

AD 680039

AD

USAAVLABS TECHNICAL REPORT 68-67

LIFTING SURFACE THEORY AND TAIL DOWNWASH CALCULATIONS FOR V/STOL AIRCRAFT IN TRANSITION AND CRUISE

By

**E. S. Levinsky
N. U. Thommen
P. M. Yager
C. N. Molland**

October 1968

**U. S. ARMY AVIATION MATERIEL LABORATORIES
FORT EUSTIS, VIRGINIA**

CONTRACT DAAJ02-67-C-0059

**AIR VEHICLE CORPORATION
SAN DIEGO, CALIFORNIA**

*This document has been approved
for public release and sale; its
distribution is unlimited.*



JAN 21 1969

115



Disclaimers

The findings in this report are not to be construed as an official Department of the Army position unless so designated by other authorized documents.

When Government drawings, specifications, or other data are used for any purpose other than in connection with a definitely related Government procurement operation, the United States Government thereby incurs no responsibility nor any obligation whatsoever; and the fact that the Government may have formulated, furnished, or in any way supplied the said drawings, specifications, or other data is not to be regarded by implication or otherwise as in any manner licensing the holder or any other person or corporation, or conveying any rights or permission, to manufacture, use, or sell any patented invention that may in any way be related thereto.

Disposition Instructions

Destroy this report when no longer needed. Do not return it to the originator.





DEPARTMENT OF THE ARMY
U. S. ARMY AVIATION MATERIEL LABORATORIES
FORT EUSTIS, VIRGINIA 23604

This report was prepared by the Air Vehicle Corporation under the terms of Contract DAAJ02-67-C-0059. It consists of the development of a theoretical method and resulting computer program for calculating the wake flow field characteristics of wing and propeller combinations during transition of V/STOL vehicles.

Reasonable agreement has been obtained in comparison of the theory and experimental data at low to moderate wing angles of attack. However, insufficient experimental data are available to test the validity of the theory at high wing angles of attack.

The report is published for the exchange of information and the stimulation of ideas.

**Project 1F125901A142
Contract DAAJ02-67-C-0059
USAAVLABS Technical Report 68-67
October 1968**

**LIFTING SURFACE THEORY AND TAIL DOWNWASH
CALCULATIONS FOR V/STOL AIRCRAFT
IN TRANSITION AND CRUISE**

Final Report

Report No. 356

by

**E. S. Levinsky, H. U. Thommen,
P. M. Yager, and C. H. Holland**

Prepared by

**Air Vehicle Corporation
San Diego, California**

for

**U. S. ARMY AVIATION MATERIEL LABORATORIES
FORT EUSTIS, VIRGINIA**

**This document has been approved
for public release and sale; its
distribution is unlimited.**

A ACT

A large-tilt-angle lifting-surface theory is developed for tilt-wing and tilt-propeller (or rotor) type V/STOL aircraft. The method is based upon an inclined actuator disc analysis in which closed-form solutions are obtained for the velocity potential inside and outside a single fully contracted circular slipstream at large distances behind the actuator surface. Both the normal velocity and the nonlinear pressure boundary conditions are satisfied exactly across the slipstream interface for a single slipstream at arbitrary inclination angles to the free stream.

The inclined actuator disc analysis is combined with a discrete-vortex Weissinger-type lifting surface theory for application to wing-propeller combinations at arbitrary wing angle of attack, propeller tilt angle, and thrust coefficient. Wing-induced modifications to the boundary conditions across the slipstream interface are made according to the approach of Ribner and Ellis. The theory is generalized for configurations with one, two, or four slipstreams, and effects of slipstream rotation are introduced in all but the single-slipstream cases.

Sample calculations showing a comparison with previous test data are presented. Agreement between theory and experiment is shown to be satisfactory for small slipstream inclination angles. However, at large tilt angles the theory (with an undeformed, but displaced, slipstream and wake) tends to predict significantly lower downwash angles in the tail region than observed from a single set of test data, possibly due to slipstream deformation and wake roll-up which reduce the downward wake displacement. Use of only one-half the calculated wake displacement gave improved agreement with downwash angle data at these conditions. However, insufficient downwash angle data are available for making a general evaluation of the theory at large slipstream angles.

Extensive digital computer results are given in chart form, showing span loading, downwash angle ϵ , stability parameter $d\epsilon/d\alpha$, and dynamic pressure inside as well as outside the propeller (rotor) slipstream at arbitrary points behind the wing. These charts are presented for V/STOL configurations with two and four slipstreams and at flight conditions ranging from hover to cruise.

FOREWORD

This publication constitutes the final technical report under Contract DAAJ02-67-C-0059 for the U. S. Army Aviation Materiel Laboratories (USAAVLABS), Fort Eustis, Virginia.

Work on this contract, entitled "Downwash Charts for Calculating Horizontal Tail Stability Derivatives for V/STOL Aircraft", was performed by Air Vehicle Corporation, San Diego, California, during the period April 1967 through June 1968.

Mr. John L. Shipley of the Aeromechanics Division (USAAVLABS) was the Army technical representative, and his contributions are gratefully acknowledged. Mr. E. S. Levinsky of Air Vehicle Corporation was the principal investigator. Dr. H. U. Thommen (Staff Scientist, Air Vehicle Corporation) was responsible in a large measure for the inclined actuator disc theory. Numerical work was carried out by Messrs. P. M. Yager and C. H. Holland on the CDC 3600 digital computer at the University of California San Diego, La Jolla, California.

TABLE OF CONTENTS

	<u>Page</u>
ABSTRACT	iii
FOREWORD	v
LIST OF ILLUSTRATIONS	ix
LIST OF TABLES	xiii
LIST OF SYMBOLS	xiv
INTRODUCTION	1
INCLINED ACTUATOR DISC THEORY	3
Boundary Conditions and General Solution	3
Evaluation of the Unknown Coefficients	5
Complex Perturbation Potential	6
Velocity Field	7
Forces and Power on an Inclined Actuator Disc	9
Comparison With Propeller Test Data	13
WING LIFTING SURFACE THEORY WITH INCLINED SLIPSTREAMS	16
Boundary Conditions	17
Slipstream Boundary Conditions	17
Wing Boundary Condition	20
Velocity Field and Downwash Angles	22
Resultant Force and Span Loading	23
SAMPLE CALCULATIONS AND COMPARISON WITH DATA	25
DESIGN CHARTS	27
CONCLUSIONS AND RECOMMENDATIONS	29
REFERENCES	80
APPENDIX I. EVALUATION OF INTEGRALS ARISING IN INCLINED ACTUATOR DISC THEORY	82
APPENDIX II. SLIPSTREAM SWIRL VELOCITY	84

	<u>Page</u>
APPENDIX III. FORTRAN COMPUTER PROGRAM.	85
General Description	85
Input Description	85
Specification of the Aircraft Configuration. .	86
Specification of the Remaining	
Parameters and Data	87
Program Control Cards	88
Sample Computer Input and Output	88
DISTRIBUTION	97

LIST OF ILLUSTRATIONS

<u>Figure</u>		<u>Page</u>
1	Flow Model and Coordinate Systems, Inclined Actuator Disc Theory	30
2	Control Surface for Determination of Forces and Power, Inclined Actuator Disc Theory	31
3	Vortex Tube Angle, Inclined Actuator Disc Theory . . .	32
4	Variation in Power Required With Propeller Tilt Angle From Inclined Actuator Disc Theory	33
5	Downwash Angle Across Slipstream Centerline, Inclined Actuator Disc Theory	34
6	Theoretical Downwash Angle on Slipstream Centerline, Inclined Actuator Disc Theory	35
7	Comparison With Slipstream Downwash Angle Test Data	36
8	Comparison With Slipstream Rotation Angle Test Data From Reference 13.	37
9	Comparison With Slipstream Rotation Angle Test Data From Reference 14	38
10	Vortex Singularities for Lifting Surface Theory With Inclined Slipstream	39
11	Comparison of Discrete Vortex Formulation Loadings and Vortex Strength With Theory of Ribner and Ellis . .	40
12	Comparison of Span Load Distribution With Test Data, Single Untilted Ducted Fan With Wing	41
13	Comparison of Downwash Angles With Test Data, Single Untilted Ducted Fan With Wing	42
14	Comparison of Span Load Distribution With Test Data, Single Untilted Propeller With Wing	43
15	Comparison of Downwash Angle With Test Data, Single Untilted Propeller With Wing	44
16	Comparison of Span Load Distribution With Test Data, Single Tilted Propeller With Wing	45

<u>Figure</u>		<u>Page</u>
17	Comparison of Span Load Distribution With Test Data: Two Tilted Propellers With Rotation, $T_c'' = 0.50$.	46
18	Comparison of Span Load Distribution With Test Data: Two Tilted Propellers With Rotation, $T_c'' = 0.60$	47
19	Comparison of Downwash Angle With Test Data: Four Tilted Propellers With Rotation, Full Vertical Wake Displacement	48
20	Comparison of Downwash Angle With Test Data: Four Tilted Propellers With Rotation, $1/2$ Vertical Wake Displacement	49
21	Two-Slipstream Configuration Design Charts: $T_c'' = 0$, $\alpha = 10^\circ$, $\delta_f = 0^\circ$	50
22	Two-Slipstream Configuration Design Charts: $T_c'' = 0.5$, $\alpha = 20^\circ$, $\alpha_p = 20^\circ$, $\delta_f = 0^\circ$, $J = 0.34$	51
23	Two-Slipstream Configuration Design Charts: $T_c'' = 0.5$, $\alpha = 20^\circ$, $\alpha_p = 30^\circ$, $\delta_f = 0^\circ$, $J = 0.34$	52
24	Two-Slipstream Configuration Design Charts: $T_c'' = 0.5$, $\alpha = 40^\circ$, $\alpha_p = 40^\circ$, $\delta_f = 0^\circ$, $J = 0.34$	53
25	Two-Slipstream Configuration Design Charts: $T_c'' = 0.5$, $\alpha = 40^\circ$, $\alpha_p = 30^\circ$, $\delta_f = 0^\circ$, $J = 0.34$	54
26	Two-Slipstream Configuration Design Charts: $T_c'' = 1.0$, $\alpha = 80^\circ$, $\alpha_p = 90^\circ$, $\delta_f = 0^\circ$, $J = 0$	55
27	Two-Slipstream Configuration Design Charts: $T_c'' = 0$, $\alpha = 10^\circ$, $\delta_f = 30^\circ$	56
28	Two-Slipstream Configuration Design Charts: $T_c'' = 0.5$, $\alpha = 20^\circ$, $\alpha_p = 20^\circ$, $\delta_f = 30^\circ$, $J = 0.34$	57
29	Two-Slipstream Configuration Design Charts: $T_c'' = 0.5$, $\alpha = 20^\circ$, $\alpha_p = 30^\circ$, $\delta_f = 30^\circ$, $J = 0.34$	58
30	Two-Slipstream Configuration Design Charts: $T_c'' = 0.5$, $\alpha = 40^\circ$, $\alpha_p = 40^\circ$, $\delta_f = 30^\circ$, $J = 0.34$	59
31	Two-Slipstream Configuration Charts: $T_c'' = 0.5$, $\alpha = 40^\circ$, $\alpha_p = 30^\circ$, $\delta_f = 30^\circ$, $J = 0.34$	60
32	Two-Slipstream Configuration Charts: $T_c'' = 0.75$, $\alpha = 40^\circ$, $\alpha_p = 40^\circ$, $\delta_f = 30^\circ$, $J = 0.26$	61

<u>Figure</u>		<u>Page</u>
33	Two-Slipstream Configuration Charts: $T_c'' = 0.75, \alpha = 40^\circ, \alpha_p = 30^\circ, \delta_f = 30^\circ, J = 0.26$. . .	62
34	Two-Slipstream Configuration Charts: $T_c'' = 0.75, \alpha = 50^\circ, \alpha_p = 50^\circ, \delta_f = 30^\circ, J = 0.26$. . .	63
35	Two-Slipstream Configuration Charts: $T_c'' = 0.75, \alpha = 50^\circ, \alpha_p = 60^\circ, \delta_f = 30^\circ, J = 0.26$. . .	64
36	Four-Slipstream Configuration Design Charts: $T_c'' = 0, \alpha = 10^\circ, \delta_f = 0^\circ$	65
37	Four-Slipstream Configuration Design Charts: $T_c'' = 0.75, \alpha = 20^\circ, \alpha_p = 20^\circ, \delta_f = 0^\circ, J = 0.37$. . .	66
38	Four-Slipstream Configuration Design Charts: $T_c'' = 0.75, \alpha = 20^\circ, \alpha_p = 30^\circ, \delta_f = 0^\circ, J = 0.37$. . .	67
39	Four-Slipstream Configuration Design Charts: $T_c'' = 0.75, \alpha = 40^\circ, \alpha_p = 40^\circ, \delta_f = 0^\circ, J = 0.37$. . .	68
40	Four-Slipstream Configuration Design Charts: $T_c'' = 0.75, \alpha = 40^\circ, \alpha_p = 30^\circ, \delta_f = 0^\circ, J = 0.37$. . .	69
41	Four-Slipstream Configuration Design Charts: $T_c'' = 1.0, \alpha = 80^\circ, \alpha_p = 90^\circ, \delta_f = 0^\circ, J = 0$	70
42	Four-Slipstream Configuration Design Charts: $T_c'' = 0, \alpha = 10^\circ, \delta_f = 55^\circ$	71
43	Four-Slipstream Configuration Design Charts: $T_c'' = 0.5, \alpha = 20^\circ, \alpha_p = 20^\circ, \delta_f = 55^\circ, J = 0.37$. . .	72
44	Four-Slipstream Configuration Design Charts: $T_c'' = 0.5, \alpha = 20^\circ, \alpha_p = 30^\circ, \delta_f = 55^\circ, J = 0.37$. . .	73
45	Four-Slipstream Configuration Design Charts: $T_c'' = 0.95, \alpha = 60^\circ, \alpha_p = 60^\circ, \delta_f = 55^\circ, J = 0.14$. . .	74
46	Four-Slipstream Configuration Design Charts: $T_c'' = 0.95, \alpha = 60^\circ, \alpha_p = 50^\circ, \delta_f = 55^\circ, J = 0.14$. . .	75
47	Four-Slipstream Configuration Design Charts: $T_c'' = 0.75, \alpha = 20^\circ, \alpha_p = 20^\circ, \delta_f = 55^\circ, J = 0.26$. . .	76
48	Four-Slipstream Configuration Design Charts: $T_c'' = 0.75, \alpha = 20^\circ, \alpha_p = 30^\circ, \delta_f = 55^\circ, J = 0.26$. . .	77

<u>Figure</u>		<u>Page</u>
49	Four-Slipstream Configuration Design Charts: $T_c'' = 0.75$, $\alpha = 40^\circ$, $\alpha_p = 40^\circ$, $\delta_f = 35^\circ$, $J = 0.2$	78
50	Four-Slipstream Configuration Design Charts: $T_c'' = 0.75$, $\alpha = 40^\circ$, $\alpha_p = 30^\circ$, $\delta_f = 55^\circ$, $J = 0.26$. . .	79

LIST OF TABLES

<u>Table</u>		<u>Page</u>
I	Recognized Symbols Following a ^\$WING^^ Control Word	89
II	Recognized Symbols Following a ^\$DATA^^ Control Word	91
III	Recognized Symbols Following ^\$SCHED^ and ^\$PLOT^^ Control Words	93

LIST OF SYMBOLS

A_p	propeller disc area
A_s	area of fully contracted propeller slipstream
b	wing span
C_{D_0}	zero lift drag coefficient
C_{H_p}''	propeller horizontal force coefficient based on propeller area and slipstream total pressure [Eq. (27)]
C_{L_p}''	propeller vertical force coefficient based on propeller area and slipstream total pressure [Eq. (28)]
C_l	section lift coefficient based on q_∞
C_{l_a}	section ideal lift coefficient
C, D	unknown coefficients in Eqs. (4) and (5)
C_n''	section normal force coefficient based on slipstream total pressure [$= n/c (q_\infty + \Delta H)$]
c	wing chord length
D	drag force
$\vec{e}_r, \vec{e}_x, \vec{e}_\theta$	unit vectors in cylindrical coordinate system
\vec{e}_z	unit vector in z direction
F	complex potential (inclined actuator disc theory)
G	integral defined by Eq. (24)
$g(\mu)$	function of μ [$= (1 + \mu^2) (1 - \mu)^{-1} G_0$]
H	total pressure
h	one-half the vortex spacing on the wing
I	integral defined by Eq. (24), also number of wing control stations
i	$\sqrt{-1}$
J	propeller advance ratio

K	number of slipstreams
L	lift force
M	number of slipstream control points
N	propeller revolutions per second
n	normal force per unit span
P, P'	power, also potential influence function (P' for multi-slipstreams)
p	static pressure
q	dynamic pressure
R	radius of fully contracted slipstream
R_c	radius of cylindrical control surface
R_p	propeller radius
r, θ	cylindrical coordinates, slipstream coordinate system
S	surface area, also downwash velocity influence coefficient
T	propeller thrust
T_c''	propeller thrust coefficient [$= T/A_p (q_\infty + \Delta H)$]
u, v, w	velocity components in slipstream coordinate system
V	velocity
V_y	induced velocity inside slipstream
V_∞	free-stream velocity
V_R	resultant velocity [Eqs. (51) and (52)]
v_θ	swirl velocity given by Eq. (34)
w_∞	component of free-stream velocity in z direction
X	component of propeller force in x direction
x, y, z	slipstream coordinate system

x', y', z'	free-stream coordinate system
y_p	spanwise position of propeller centerline
Z	component of propeller force in z direction, also complex variable $Z = re^{i\theta} = y + iz$
α	wing angle of attack
α_{eff}	effective angle of attack [Eq. (47)]
α_a	ideal angle of attack
α_p	propeller tilt angle
α_δ	flap effectiveness parameter
Γ	vortex strength
γ	ring vortex strength per unit length
Δ	difference operator
$\Delta\theta_n$	vortex spacing on slipstream(s)
δ	inclination of slipstream vortex tube with respect to the free stream
δ_f	flap angle, deg.
δ_{mn}	Kronecker delta
ϵ	downwash angle
ζ	unknown function of θ
θ	polar coordinate (r, θ) in slipstream coordinate system
μ	ratio u_o/u_s
ν_t	effective turbulent kinematic viscosity
ρ	density
φ	velocity perturbation potential
φ'	reduced velocity perturbation potential ($= \mu \varphi$)

$\varphi_{o\Gamma}, \varphi_{s\Gamma}$	perturbation potentials due to wing and slipstream horse-shoe vortex systems
ψ	stream function
Ω	effective origin of propeller viscous core ahead of $c/4$ point
∇	gradient operator

Subscripts

a	ideal
i, j	summation indices over wing
k, l	summation indices over the number of slipstreams
m, n	summation indices over the slipstream(s)
o	outside slipstream
p	propeller
R	resultant
s	inside slipstream
u	upper boundary of slipstream
Γ	induced by wing and slipstream vortex elements
γ	induced by ring vortices
∞	free stream

Superscript

$-$	normalized quantity defined by Eq. (24)
\rightarrow	vector quantity
$*$	complex conjugate

INTRODUCTION

Considerable research effort has been expended in the past pertaining to the interaction between a wing and slipstream. Most noteworthy is the pioneering contribution of Koning (reference 1), who formulated the proper boundary conditions across the interface of an uninclined slipstream. Koning matched both pressure and flow angle on each side of the boundary within the limitations of linearized theory and used the Prandtl lifting line theory to predict slipstream interference effects at cruise speeds. Koning's treatment was extended to a wider range of forward speeds by Glauert (reference 2) and by Franke and Weinig (reference 3). The latter authors also improved and generalized the theory to include effects of small propeller inclination and slipstream rotation. Nevertheless, comparison with test data indicated that the theory overpredicted the additional wing lift inside the slipstream by a substantial margin (reference 4).

Partly because of this failure of the lifting line approach, which was assumed due to the low aspect ratio of the wing segment inside the slipstream, Graham, et al. (reference 5), supplemented the lifting line theory with lifting surface (Weissinger) and slender body theories, and found improved agreement with test data. The Weissinger lifting surface theory was subsequently generalized in a series of papers by Ribner and Ellis (references 6 through 8) to apply to multiple uninclined slipstreams of arbitrary cross section. The latter authors introduced horseshoe vortex elements of unknown strength along the wing $1/4$ -chord line, and required that the wing boundary condition be satisfied at the $3/4$ -chord line in accordance with the standard Weissinger approach. By considering a reduced velocity potential inside the slipstream, they were able to satisfy both the pressure and flow angle boundary conditions across the slipstream(s) through introduction of an additional set of unknown horseshoe vortex elements around the slipstream periphery. Calculations carried out for a wing and a single uninclined slipstream showed good agreement with the test data of Brenckmann (reference 9).

It is clear that the theory of wing-propeller interaction must be extended to include effects of large slipstream inclination, if the theory is to be applicable for tilt-wing or tilt-rotor type V/STOL aircraft. Previous attempts to treat inclined slipstreams have been unsuccessful, partly because of the use of a solid cylinder approximation for the inclined slipstream, e.g., references 5 and 8. Although the solid cylinder produces a disturbed flow field outside the slipstream which satisfies the normal velocity boundary condition, the nonlinear pressure boundary condition is not satisfied. The rectification of this inadequacy and the development of a wing-slipstream interaction theory applicable to V/STOL technology are the motivations for the present study.

In the present report a new inclined actuator disc theory, which satisfies both the normal velocity and nonlinear pressure boundary conditions across the slipstream interface, is first derived. The inclined actuator

disc theory is subsequently combined with the Ribner-Ellis lifting surface method to treat tilt-rotor or propeller-wing combinations at large tilt angles and at forward speeds from hover to cruise. Effects of slipstream rotation are included by adopting a viscous core vortex model inside the slipstream for the swirl velocities. The major assumptions in the resulting generalized analysis are that the slipstream is fully contracted, is of basically circular cross section, and is of constant total head (but with nonuniform velocities and static pressures) in the region of the wing. Unseparated flow is assumed over the wing panels, both inside and outside the slipstream, and effects of wake roll-up and slipstream distortion are assumed to be negligible.

The theory is compared wherever possible with available experimental data. In addition, an extensive series of calculations is carried out to provide theoretical data on the span loading and on the downwash angles and dynamic pressures in the wake and slipstream for representative two- and four-slipstream V/STOL configurations and flight conditions. These results are presented in chart form for the rapid estimation of the stability and control characteristics and of wing structural requirements. It is recognized that additional experimental verification of the theory is required, especially for large tilt angle conditions for which detailed wake and slipstream surveys are largely unavailable.

INCLINED ACTUATOR DISC THEORY

BOUNDARY CONDITIONS AND GENERAL SOLUTION

The incompressible flow field created by an actuator disc with its axis inclined to the free-stream direction at an angle α_p is to be considered

(Figure 1). The air passing through the actuator disc is assumed to experience a uniform increase in total and static pressure of magnitude ΔH , so that the total pressure inside the slipstream has the constant value $H_s = H_o + \Delta H$, where H_o is the total pressure outside the slipstream. The resultant force on the actuator disc is assumed to act normal to the disc surface, and is of magnitude $A_p \Delta H$. In this respect the actuator disc differs from an inclined propeller or rotor which develops forces in the plane of rotation. This in-plane force is usually small compared to the normal force, and is neglected in the present formulation.

We next assume that this flow field can be approximated far behind the actuator disc by a distribution of suitable singularities around the surface of a semi-infinite circular tube (Figure 1). The axis of the tube is inclined to the free stream by the angle δ . This is the angle at which the slipstream would be inclined far behind the disc if not for distortion. The radius of the tube is taken as that of the fully contracted slipstream $r = R$, and the boundary conditions which must hold across a fluid interface are satisfied on the surface of the tube.

A slipstream coordinate system x, y, z (or equivalently x, r, θ) with the x -axis coincident with the tube axis is introduced for convenience. Denoting by \vec{V}_o, \vec{V}_s the velocities outside and inside the slipstream, respectively, the boundary condition on the velocity components normal to the slipstream boundary is

$$\frac{\vec{e}_r \cdot \vec{V}_o}{\vec{e}_x \cdot \vec{V}_o} = \frac{\vec{e}_r \cdot \vec{V}_s}{\vec{e}_x \cdot \vec{V}_s} \quad \text{for } r = R \quad (1)$$

where $\vec{e}_x, \vec{e}_r, \vec{e}_\theta$ are unit vectors in the designated directions (Figure 1). Equation (1) signifies that the flow angles normal to the cylindrical surface are the same across the interface, but allows a discontinuity in the velocity components in the plane of the surface.

The axial velocity components of \vec{V}_o and \vec{V}_s are designated by $\vec{e}_x \cdot u_o$ and $\vec{e}_x \cdot u_s$, respectively, and may be regarded as constant at large distances from the actuator disc. However, the cross-flow velocity components are nonuniform, even for large x , and lead to deformation of the originally circular slipstream.

A second boundary condition is that the static pressures $p_o(r, \theta)$ and $p_s(r, \theta)$ outside and inside the slipstream, respectively, are identical on the tube surface. It will prove convenient in the analysis to change the flow into one of constant total head by subtracting ΔH from the pressure p_s inside the slipstream. The pressure boundary condition is then

$$p_o(R, \theta) - p_s(R, \theta) = \Delta H \quad (2)$$

The above flow field may be obtained by suitably distributing singularities on the surface of the cylindrical tube. First, consider a distribution of vortices $\hat{\gamma} = \hat{e}_\theta \frac{d\Gamma(x)}{dx}$ pointed in the azimuthal direction with strength Γ independent of θ (ring vortices). Restricting ourselves to large distances behind the actuator disc, the ring vortex distribution may be regarded as infinitely long and of uniform strength. It will therefore induce only axial velocity components inside the tube, and will have no influence outside the tube. The derivative γ is chosen so that the induced velocity \hat{V}_γ inside the tube is $\hat{e}_x(u_s - u_o)$, viz.,

$$\begin{aligned} \lim_{x \rightarrow \infty} \hat{V}_\gamma &= \hat{e}_x \gamma = \hat{e}_x(u_s - u_o), & r < R \\ \lim_{x \rightarrow \infty} \hat{V}_\gamma &= 0, & r > R \end{aligned} \quad (3)$$

Next, a distribution of vortices and sources and sinks with axes parallel to x is introduced. These singularities will vary in strength as a function of θ , but can be assumed independent of x when $x \rightarrow \infty$. In this limit, and using symmetry conditions about $\theta = \pm \pi/2$, the most general form of the resulting two-dimensional velocity perturbation potential may be written as

$$\varphi = \varphi_s = - \sum_{n=1,3,5}^{\infty} \frac{R C_n (r/R)^n}{n} \sin n\theta, \quad r < R \quad (4)$$

$$\varphi = \varphi_o = \sum_{n=1,3,5}^{\infty} \frac{R D_n (r/R)^{-n}}{n} \sin n\theta, \quad r > R \quad (5)$$

Thus, the resultant velocities for $x \rightarrow \infty$ become

$$\hat{V}_s = \hat{V}_\infty + \hat{e}_x(u_s - u_o) + \nabla \varphi_s = \hat{e}_x u_s + \hat{e}_z w_\infty + \nabla \varphi_s, \quad r < R \quad (6)$$

$$\hat{V}_o = \hat{V}_\infty + \nabla \varphi_o = \hat{e}_x u_o + \hat{e}_z w_\infty + \nabla \varphi_o, \quad r > R \quad (7)$$

where the undisturbed free-stream velocity \hat{V}_∞ has been resolved into components

$$\hat{V}_\infty = \hat{e}_x u_o + \hat{e}_z w_\infty$$

with $u_o = V_\infty \cos \delta$ and $w_\infty = V_\infty \sin \delta$

EVALUATION OF THE UNKNOWN COEFFICIENTS

The coefficients C_n, D_n , which must be known to obtain the velocity field, are determined from the boundary conditions on the slipstream interface.

Making use of Eqs. (6) and (7), the normal velocity condition [Eq. (1)] becomes

$$\partial \phi_o / \partial r - \mu \partial \phi_s / \partial r = -(1 - \mu) w_\infty \sin \theta, \quad r = R \quad (8)$$

where $\mu = u_o / u_s$.

Introducing Eqs. (4) and (5), and satisfying Eq. (8) for each term in $\sin n\theta$, gives the following conditions on the coefficients:

$$\begin{aligned} D_1 - \mu C_1 &= (1 - \mu) w_\infty \\ D_n &= \mu C_n, \quad n \geq 3 \end{aligned} \quad (9)$$

Utilizing the steady form of the incompressible Bernoulli equation, the pressure condition [Eq. (2)] may be similarly expressed as

$$2 \frac{\Delta H}{\rho} = u_s^2 - u_o^2 + \left[\hat{e}_z w_\infty + \nabla \phi_s \right]^2 - \left[\hat{e}_z w_\infty + \nabla \phi_o \right]^2, \quad r = R \quad (10)$$

where the density ρ is taken as the same inside and outside the slipstream. Since $\nabla \phi_s$ and $\nabla \phi_o$ are both functions of θ , whereas the remaining quantities in Eq. (10) are independent of θ , it is required that

$$\frac{2 \Delta H}{\rho} = u_s^2 - u_o^2, \quad r = R$$

or, equivalently,

$$\frac{\Delta H}{q_\infty} = \frac{1 - \mu^2}{\mu^2} \cos^2 \delta, \quad r = R \quad (11)$$

in order that Eq. (10) be satisfied. Using complex notation, the pressure condition becomes

$$|i w_{\infty} + \nabla \varphi_s| = |i w_{\infty} + \nabla \varphi_o|, \quad r = R$$

which may be written, without loss of generality, as

$$e^{i\zeta(\theta)} (w_{\infty} - i \nabla \varphi_s) = w_{\infty} - i \nabla \varphi_o, \quad r = R \quad (12)$$

where ζ is an unknown function of θ to be determined, and $\nabla \varphi = \partial \varphi / \partial y + i (\partial \varphi / \partial z)$. Substituting Eqs. (4), (5), and (9) into Eq. (12) for $r = R$, and observing that all coefficients C_n , D_n are real, it is readily determined that ζ must be either 0 or π . Taking first $\zeta = 0^*$, and equating coefficients of like powers of $e^{i\theta}$ on both sides of Eq. (12), gives

$$\begin{aligned} C_1 &= 0 \\ C_3 &= -(1-\mu) w_{\infty} \\ C_{n+2} &= -\mu C_n, \quad n \geq 3 \end{aligned} \quad (13)$$

Complex Perturbation Potential

In terms of the complex potentials $F_s (= \varphi_s + i\psi_s)$ and $F_o (= \varphi_o + i\psi_o)$ inside and outside the slipstream, respectively, Eqs. (4) and (5) yield

$$\begin{aligned} dF_s/dZ &= i \sum_{n=1,3,\dots} C_n (Z/R)^{n-1} \\ dF_o/dZ &= -i \sum_{n=1,3,\dots} \frac{D_n}{(Z/R)^{n+1}} \end{aligned} \quad (14)$$

where $dF/dZ = (\varphi_r \cos \theta - \frac{1}{r} \varphi_{\theta} \sin \theta) - i (\varphi_r \sin \theta + \frac{1}{r} \varphi_{\theta} \cos \theta)$

and $Z = r e^{i\theta}$.

By inserting Eqs. (9) and (13) for the coefficients C_n , D_n in Eq. (14), it is found that the series can be readily summed. The resulting closed-

* The rejection of solutions with $\zeta = \pi$ is justified in the next section.

form expressions may be integrated with respect to Z , giving

$$F_s = -i \frac{(1-\mu)}{\mu} w_\infty Z + \frac{(1-\mu)}{2\mu^{3/2}} w_\infty R \ln \left[\frac{Z/R - i/\mu^{1/2}}{Z/R + i/\mu^{1/2}} \right] \quad (15)$$

$$F_o = - \frac{(1-\mu)}{2\mu^{1/2}} w_\infty R \ln \left[\frac{Z/R - i/\mu^{1/2}}{Z/R + i/\mu^{1/2}} \right] \quad (16)$$

In the limit $\mu \rightarrow 1$, which corresponds to an actuator disc of vanishing strength, $\Delta H \rightarrow 0$ and F_s and F_o vanish, indicating that the flow field is undisturbed in this limit. Re-evaluation of the coefficients for $\xi = \pi$ yields expressions similar in form to Eqs. (15) and (16), except that the factor $(1-\mu)$ is replaced by $(1+\mu)$. These solutions must be discarded, because they fail to satisfy the physical flow in the limit $\mu \rightarrow 1$.

In the limit $\mu \rightarrow 0$, corresponding either to an inclined actuator disc of infinite strength ($\Delta H \rightarrow \infty$) or at zero forward velocity, expansion of the logarithmic term in Eq. (16) shows that F_o becomes the complex potential produced by a doublet at the origin. Upon superposition of the component w_∞ of the free stream velocity parallel to the z -axis, the resultant outside flow velocity becomes the same as if the slipstream boundary were a solid surface. The solid cylinder approximation for an inclined slipstream, which was discussed in the Introduction, is found to hold only in this limit.

At intermediate values of μ , the complex perturbation potential F_o is recognized as that due to a source of strength $\pi(1-\mu)w_\infty R/\mu^{1/2}$ located at $Z = -iR\mu^{1/2}$ and to a sink of equal strength located at $Z = iR\mu^{1/2}$. Similarly, F_s is that of a source and sink at $Z = \pm iR/\mu^{1/2}$, together with a parallel flow of velocity $(1-\mu)w_\infty/\mu$ in the positive Z direction.

Velocity Field

Having obtained the complex potential in the Trefftz plane $x = \infty$, the overall velocity field is readily evaluated from Eqs. (6) and (7). The velocity potentials ϕ_s and ϕ_o are found by extracting the real parts of F_s and F_o , respectively. Thus, in rectangular coordinates,

$$\phi_s = \frac{(1-\mu)}{\mu} w_\infty z - \frac{(1-\mu)}{4\mu^{3/2}} w_\infty R \ln \left[\frac{y^2 + z^2 + R^2/\mu + 2Rz/\mu^{1/2}}{y^2 + z^2 + R^2/\mu - 2Rz/\mu^{1/2}} \right] \quad (17)$$

$$\varphi_o = \frac{(1-\mu)}{4\mu^{1/2}} w_\infty R \ln \left[\frac{y^2 + z^2 + R^2\mu + 2Rz\mu^{1/2}}{y^2 + z^2 + R^2\mu - 2Rz\mu^{1/2}} \right] \quad (18)$$

Taking the gradient of the above expressions and substituting into Eqs. (6) and (7), the overall velocity components u, v, w in the x, y, z directions at any arbitrary point in the flow field are found to be

$$\left. \begin{aligned} u_o &= V_\infty \cos \delta \\ v_o &= - \left\{ \frac{2(1-\mu)yz}{\left[y^2 + (z - R\mu^{1/2})^2 \right] \left[y^2 + (z + R\mu^{1/2})^2 \right]} \right\} R^2 V_\infty \sin \delta \\ w_o &= \left\{ 1 + \frac{(1-\mu)R^2(y^2 - z^2 + \mu R^2)}{\left[y^2 + (z - R\mu^{1/2})^2 \right] \left[y^2 + (z + R\mu^{1/2})^2 \right]} \right\} V_\infty \sin \delta \end{aligned} \right\} \quad (19)$$

for $y^2 + z^2 > R^2$, and

$$\left. \begin{aligned} u_s &= V_\infty \cos \delta / \mu \\ v_s &= \left\{ \frac{z(1-\mu)yz}{\left[\mu y^2 + (\mu^{1/2}z - R)^2 \right] \left[\mu y^2 + (\mu^{1/2}z + R)^2 \right]} \right\} R^2 V_\infty \sin \delta \\ w_s &= \left\{ 1 - \frac{(1-\mu)R^2(\mu y^2 - \mu z^2 + R^2)}{\left[\mu y^2 + (\mu^{1/2}z - R)^2 \right] \left[\mu y^2 + (\mu^{1/2}z + R)^2 \right]} \right\} V_\infty \frac{\sin \delta}{\mu} \end{aligned} \right\} \quad (20)$$

for $y^2 + z^2 < R^2$.

Equations (19) and (20) give the velocities in the flow field at $x = \infty$ in terms of the parameters μ and δ . Before applying these expressions to evaluating the downwash angle distribution inside as well as outside the slipstream, it will prove convenient to express μ and δ in terms of parameters of more physical significance. This will be accomplished in the next section by relating μ and δ to the tilt angle α_p and thrust coefficient T'_c . It will also be convenient to relate the vortex tube radius R to the physical radius of the disc R_p .

Forces and Power on an Inclined Actuator Disc

In order to evaluate the forces acting on the disc, a cylindrical control tube of radius R_c is placed around the disc and slipstream as shown in Figure 2. The value of R_c is taken sufficiently large so that the pressure is ambient around the cylindrical surface S_3 . The velocity is assumed to be equal to \vec{V}_∞ on the forward face S_1 at $x = -\infty$, and to be given by Eqs. (19) and (20) on the rear face S_2 at $x = \infty$. The continuity equation is written in integral form as

$$\int_{S_1} \vec{V}(-\infty) \cdot d\vec{S} + \int_{S_{2s}} + \int_{S_{2o}} \vec{V}(\infty) \cdot d\vec{S} + \int_{S_3} \vec{V}(R_c) \cdot d\vec{S} = 0$$

where $d\vec{S}$ has the direction of the inward normal to the surface, and the subscripts s and o designate the portions of S_2 inside and outside the slipstream, respectively. Using Eqs. (6) and (7), the net mass flux into the cylindrical surface becomes, for a unit density,

$$\int_{S_3} \vec{V}(R_c) \cdot d\vec{S} = \pi R^2 (u_s - u_o)$$

and carries a net momentum flux

$$\int_{S_3} \vec{V} (\vec{V} \cdot d\vec{S}) = \pi R^2 (u_s - u_o) \vec{V}_\infty \quad (21)$$

The momentum equation is expressed in the form

$$\hat{T} = -\rho \int_{S_1+S_2+S_3} \vec{V} (\vec{V} \cdot d\vec{S}) - \int_{S_1+S_2+S_3} p d\vec{S} \quad (22)$$

where \hat{T} is the thrust force normal to the actuator disc. Taking the component of \hat{T} in the x direction and making use of Eqs. (6), (7), (11), and (21), together with the incompressible form of Bernoulli's equation, after some rearrangement we obtain

$$\begin{aligned}
X = \pi R^2 \rho u_s (u_s - u_o) - \frac{1 - \mu^2}{2\mu^2} \rho w_\infty^2 \pi R^2 \\
- \rho w_\infty^2 \left[I_o + \frac{I_s}{\mu^2} + \frac{1}{2} (G_o + \frac{G_s}{\mu^2}) \right] \pi R^2
\end{aligned}
\tag{23}$$

Here we have defined

$$\begin{aligned}
I_o &= \frac{1}{\pi R^2} \int_{S_{2o}} \frac{\partial \bar{\varphi}_o}{\partial z} dS \\
I_s &= \frac{1}{\pi R^2} \int_{S_{2s}} \frac{\partial \bar{\varphi}_s}{\partial z} dS \\
G_o &= \frac{1}{\pi R^2} \int_{S_{2o}} (\nabla \bar{\varphi}_o)^2 dS \\
G_s &= \frac{1}{\pi R^2} \int_{S_{2s}} (\nabla \bar{\varphi}_s)^2 dS
\end{aligned}
\tag{24}$$

where $\bar{\varphi}$ is a modified velocity potential such that

$$\begin{aligned}
\partial \bar{\varphi}_o / \partial z &= (1/w_\infty) \partial \varphi_o / \partial z \\
\partial \bar{\varphi}_o / \partial y &= (1/w_\infty) \partial \varphi_o / \partial y \\
\partial \bar{\varphi}_s / \partial z &= (\mu/w_\infty) (\partial \varphi_s / \partial z) - (1 - \mu) \\
\partial \bar{\varphi}_s / \partial y &= (\mu/w_\infty) \partial \varphi_s / \partial y
\end{aligned}$$

The integrals given by Eq. (24), as evaluated in Appendix I, are

$$I_o = I_s = -(1-\mu)$$

$$G_o = G_s = \frac{(1-\mu)^2}{2\mu} \ln \left(\frac{1+\mu}{1-\mu} \right)$$

Substituting these results into Eq. (23) gives

$$X = \pi R^2 \rho \left[u_s (u_s - u_o) + \left(\frac{1-\mu}{2\mu} \right) w_\infty^2 \left\{ (1+\mu^2) \left[1 - \frac{1-\mu}{4\mu} \ln \left(\frac{1+\mu}{1-\mu} \right) \right] - \frac{1+\mu}{2} \right\} \right] \quad (25)$$

Carrying out a similar evaluation for the component of \hat{T} in the z direction (the pressure forces do not contribute to this component) gives

$$Z = \pi R^2 \rho (1-\mu) u_o w_\infty \quad (26)$$

It is convenient to express the forces on the actuator disc in terms of horizontal and vertical force coefficients C_{H_p}'' and C_{L_p}'' , based on the propeller area A_p and the dynamic pressure in the slipstream at ambient static pressure. Thus we define

$$C_{H_p}'' = \frac{X \cos \delta - Z \sin \delta}{A_p (q_\infty + \Delta H)}$$

$$C_{L_p}'' = \frac{X \sin \delta + Z \cos \delta}{A_p (q_\infty + \Delta H)}$$

Substituting for Z and X through Eqs. (25) and (26), and using Eq. (11) for ΔH , after some simplification we obtain

$$C_{H_p}'' = \left(\frac{A_s}{A_p} \right) \frac{\left\{ 2(1-\mu) - (1-\mu)[1+\mu+g(\mu)] \sin^2 \delta \right\} \cos \delta}{\left[(1-\mu^2) \cos^2 \delta + \mu^2 \right]} \quad (27)$$

$$C_{L_p}'' = \left(\frac{A_s}{A_p} \right) \frac{\left\{ 2(1-\mu)(1+\mu^2) - (1-\mu)[1+\mu+g(\mu)] \sin^2 \delta \right\} \sin \delta}{\left[(1-\mu^2) \cos^2 \delta + \mu^2 \right]} \quad (28)$$

where $g(\mu) = \left(\frac{1+\mu^2}{1-\mu}\right) G_0$ and $A_s = \pi R^2$ is the area of the fully contracted slipstream (vortex tube).

Since \hat{T} is assumed to act normal to the plane of the disc, the tilt angle α_p is given by

$$\alpha_p = \tan^{-1} \left(C_{L_p}'' / C_{H_p}'' \right) \quad (29)$$

Introducing the thrust coefficient T_c'' , defined as

$$T_c'' = \frac{T/A_p}{q_\infty + \Delta H} = \left[\left(C_{H_p}'' \right)^2 + \left(C_{L_p}'' \right)^2 \right]^{1/2},$$

the ratio of the propeller area to slipstream area A_p/A_s becomes

$$A_p/A_s = \left[\left(C_{L_p}'' A_p/A_s \right)^2 + \left(C_{H_p}'' A_s/A_p \right)^2 \right]^{1/2} / T_c'' \quad (30)$$

where the quantities $C_{L_p}'' A_p/A_s$ and $C_{H_p}'' A_s/A_p$ are given by Eqs. (27) and (28).

Equations (11) and (27) through (30) may be used to express the flow field velocities in terms of the given physical parameters T_c'' , α_p , and A_p instead of μ , δ , and A_s . Once T_c'' , α_p , and A_p are known, μ , δ , and A_s may be obtained either by iterating on the value of δ , or graphically from Figure 3.

The power P added to the slipstream and to the outside flow by the actuator disc is readily obtained by evaluating the net flux of energy out of the cylindrical control surface in Figure 2. Thus, writing

$$P = -\frac{\rho}{2} \int_{S_1+S_2+S_3} (\hat{V} \cdot \hat{V}) (\hat{V} \cdot d\hat{S}) - \int_{S_1+S_2+S_3} p \hat{V} \cdot d\hat{S}$$

and performing a similar analysis to that done previously for the components of \hat{T} , we obtain

$$P = u_s A_s \Delta H \quad (31)$$

The effect of propeller tilt angle on power, for a fixed forward velocity and thrust coefficient, is obtained by writing Eq. (31) as

$$\frac{P(\alpha_p)}{P(0)} = \left[\frac{\cos^2 \delta + \frac{T_c''}{1 - T_c''}}{1 + \frac{T_c''}{1 - T_c''}} \right]^{1/2} \left[\frac{\frac{A_s}{A_p}(\alpha_p)}{\frac{A_s}{A_p}(0)} \right] \quad (32)$$

where δ and A_s/A_p are obtained in terms of α_p from Eq. (11) and Eqs. (27) through (30). This expression has been evaluated (Figure 4), and is compared with wind tunnel measurements of power versus tilt angle in the following section.

COMPARISON WITH PROPELLER TEST DATA

Because of the many assumptions inherent in the inclined actuator disc theory, it is of importance that the theory be evaluated by comparison with test data before being applied to the wing-slipstream interference problem. Comparisons of the power and average downwash angle across the slipstream may be made without consideration of slipstream rotation or swirl. However, the swirl effects must be added to the theory before detailed downwash survey data may be compared.

A comparison of predicted and measured effects of propeller tilt angle on power is shown in Figure 4. Both the theory, Eq. (32), and the test data, reference 10, show that the power required to produce a given value of T_c'' decreases with increasing tilt angle, with the power becoming independent of tilt angle as $T_c'' \rightarrow 1.0$. The data scatter and differences between theory and test data in Figure 4 could be due to errors in estimating the ideal efficiency of the inclined propellers.

The downwash angle ϵ far behind the propeller may be found from the expression

$$\epsilon(y, z) = -\tan^{-1} \left[\frac{w \cos \delta - u \sin \delta}{w \sin \delta + u \cos \delta} \right] \quad (33)$$

and is readily determined from the theory using Eqs. (19) and (20). As illustrated in Figure 5, Eq. (33) predicts a nonuniform downwash distribution inside the slipstream and a varying upwash outside the slipstream, except for the limiting cases $T_c'' = 0$ and 1.0. The calculated downwash

angle at the center of the slipstream has been plotted, for convenience, in Figure 6.

The nonuniform value of ϵ makes comparison with test data, obtained by means of a tailplane spanning the slipstream, somewhat difficult to interpret. Nevertheless, as illustrated in Figure 7, such "average" test data (reference 11) show a variation in the ratio of ϵ/α_p with T_c'' similar to that predicted by theory, at least for the small values of α_p for which the tests were conducted.

A simple vortex model of the slipstream has been used to calculate the swirl velocities caused by the propeller rotation (Appendix II). The analysis is similar to that by Franke and Weinig (reference 3) in that a central vortex is introduced along the slipstream axis and a helical vortex is placed around the slipstream interface. However, in order to keep the swirl velocities finite near the axis, the central vortex is "softened" by introducing viscous core effects according to Lamb (reference 12). The resulting expression (from Appendix II) for the circumferential swirl velocity $v_\theta(r)$ inside the slipstream is

$$\frac{v_\theta}{V_\infty} = \pm \frac{J}{2\pi} \left(\frac{R_p}{r} \right) \left(\frac{\Delta H}{q_\infty} \right) \left\{ 1 - \exp \left[- \left(\frac{r}{R} \right)^2 \left(\frac{R}{x + \Omega} \right) \left(\frac{R u_s}{4 v_t} \right) \right] \right\} \quad (34)$$

where $J = V_\infty / 2NR_p$ is the advance ratio, v_t is the effective turbulent viscosity, Ω is the effective starting distance ahead of the origin for the viscous core, and the sign is positive for a counterclockwise sense of rotation when viewed from the rear. No swirl velocities are predicted outside the fully contracted slipstream.

Equation (34) is compared with measurements by Stüper (reference 4) in Figure 8. The test data were obtained at several stations in the wake of a 0.49-ft.-diameter pusher propeller aligned with the free stream and at a thrust coefficient $T_c'' \approx 0.38$. With the origin $x = 0$ located at the blade trailing edge, the best fit to the data was accomplished by choosing $v_t = 0.093 \text{ ft}^2/\text{sec}$ and $\Omega = 0.08 \text{ ft}$ (approximately twice the maximum blade chord). The propeller advance ratio was 0.472, whereas the free-stream velocity was approximately 100 fps. The circulation Γ was $14.2 \text{ ft}^2/\text{sec}$ as computed from Eq. (51) of Appendix II.

It is not clear how v_t will scale for different values of these parameters, although, as discussed by Hall (reference 13), v_t scaling with either Γ or $(\Gamma)^{1/2}$ has been considered. Because it would be premature to use such scaling laws indiscriminately, and because of the lack of additional test data on the slipstream vortex, it was decided to use $v_t = 0.10 \text{ ft}^2/\text{sec}$ for all subsequent calculations and design charts employing swirl.

A comparison of Eq. (34) with test data from reference 14 is shown in Figure 9. The test data were obtained at a single station located 1.43 ft. behind the propeller (3.25 ft. diameter). The propeller was mounted on a flat-faced cylindrical nacelle which extended rearward to the measuring station. This may have been the cause of the thick viscous core which is apparent from the data. In order to achieve correspondence between the theory and data, it was necessary to place the effective turbulent origin 28.6 ft. ahead of the measuring station (20 times the actual distance) when using a nominal value of $v_t = 0.10 \text{ ft}^2/\text{sec}$. Although the correlation shown in Figure 9 is reasonable, data scatter (due possibly to wind tunnel wall interference at propeller incidence) and the scarcity of data points make the comparison somewhat questionable.

Additional experimental verification of the inclined actuator disc theory is clearly needed, both with and without effects of slipstream rotation. This is especially true for conditions of large tilt angle and thrust coefficient representative of V/STOL transition, for which little experimental data are available. In the next section the inclined actuator disc theory is used in the development of a wing lifting surface theory with inclined slipstreams.

WING LIFTING SURFACE THEORY WITH INCLINED SLIPSTREAMS

A method will be developed for calculating the span loading and wake flow field, inside and outside the slipstream, for a wing with inclined slipstreams representative of tilt-wing or tilt-propeller (rotor) V/STOL aircraft. The procedure will be applied to aircraft with one, two, or four slipstreams. For reasons of computational simplicity, the plane of the wing will be assumed to pass through the center of the slipstream(s) and to bisect the slipstream into upper and lower halves. Also, for reasons of simplicity, the formulation will be restricted to configurations with symmetrical span loadings about the aircraft centerline. This eliminates consideration of slipstream swirl for single slipstream aircraft, and requires that the propellers be rotating in opposite directions on each wing panel for the two- and four-slipstream configurations.

Basically, the method to be developed can be considered a combination of the inclined actuator disc theory developed in the previous sections and the Ribner and Ellis potential theory for a wing in an uninclined slipstream (references 6 through 8). The approach used, as shown in Figure 10, replaces the wing by a system of discrete small-span horseshoe vortices with the bound vortex elements placed along the $1/4$ -chord line (assumed unswept). The wing vortex system will produce velocity perturbations which in general violate both the pressure and normal velocity boundary conditions across the slipstream interfaces. To correct for the pressure boundary condition, a system of horseshoe vortex elements is also placed around each cylindrical vortex tube representing the boundaries of the slipstream. Violation of the normal velocity boundary condition across the slipstream is automatically suppressed by using a reduced velocity potential $\phi'_s = \mu \phi_s$ inside the slipstream, as done by Ribner and Ellis.

The tangential flow boundary condition is satisfied on the wing at the $3/4$ -chord points according to the well-known Weissinger lifting surface theory, e.g., Gray and Schenk (reference 15). However, the resultant velocity includes effects of slipstream inclination [Eqs. (19) and (20)], swirl [Eq. (34)], and perturbations from the slipstream horseshoe vortex systems, in addition to perturbations from the wing horseshoe vortex system as in reference 15. The pressure boundary condition is satisfied across the slipstream in a linear approximation, as originally suggested by Koning (reference 1). Satisfaction of the wing and slipstream boundary conditions leads to a system of linear simultaneous equations whose unknowns are the strengths of the wing and slipstream vortex elements. Subsequent solution of this system leads to the span loading and velocity field.

A further simplification has been to take all trailing vortex elements as straight and inclined downward to the free stream at the same angle δ as the axis of the vortex tube. It is recognized that a somewhat improved model might be to take the direction of the trailing vortices as coincident with the local flow angle at the particular spanwise station. Because of

the additional computational complexities, it was decided to forego this remodeling until justified by comparison with experimental data.

In the following sections, expressions are derived for the wing and slipstream boundary conditions in terms of the unknown vortex strengths. Results of the computational procedure are then compared with test data.

BOUNDARY CONDITIONS

The boundary conditions to be satisfied are a constant pressure and a constant normal velocity angle across the slipstream, and tangential flow to the effective airfoil mean line at the 3/4-chord position of the wing.

Slipstream Boundary Conditions

The pressure boundary condition, from the incompressible form of the Bernoulli equation, is now

$$\frac{2 \Delta H}{\rho} = \left[(u_s + u_{s\Gamma})^2 + (v_s + v_{s\Gamma})^2 + (w_s + w_{s\Gamma})^2 \right] - \left[(u_o + u_{o\Gamma})^2 + (v_o + v_{o\Gamma})^2 + (w_o + w_{o\Gamma})^2 \right]$$

where the single subscripted velocity components are for zero loading on the wing [Eqs. (19) and (20)], whereas quantities with a second subscript Γ refer to perturbations due to the vortex systems. By Eq. (10), and also neglecting second-order perturbations in accordance with the usual linearity assumptions, the above expression becomes

$$u_s u_{s\Gamma} + v_s v_{s\Gamma} + w_s w_{s\Gamma} = u_o u_{o\Gamma} + v_o v_{o\Gamma} + w_o w_{o\Gamma}$$

This condition will be satisfied on the slipstream in the region of the wing, for which the first terms on the left- and right-hand sides may be assumed dominant. In terms of the perturbation velocity potentials $\phi_{s\Gamma}$ and $\phi_{o\Gamma}$ inside and outside the slipstream, this becomes

$$u_s (d\phi_{s\Gamma}/dx) \simeq u_o (d\phi_{o\Gamma}/dx) \quad (35)$$

which is the usual linearized pressure boundary condition originally introduced by Koning.* Equation (35) should be satisfied for all x in the vicinity of the wing, and at all azimuthal positions θ around the slipstream.

* The full nonlinear pressure condition has been satisfied in the inclined actuator disc theory.

However, following Koning and others, Eq. (35) is integrated from $x = -\infty$ to $x = \infty$ giving

$$u_s \varphi_{s\Gamma}(\infty, R, \theta) = u_o \varphi_{o\Gamma}(\infty, R, \theta) \quad (36)$$

where $\varphi_{s\Gamma}(-\infty) = \varphi_{o\Gamma}(-\infty) = 0$. This allows the pressure boundary condition to be satisfied in the Trefftz plane. We note, however, that Eq. (36) satisfies the linearized boundary condition [Eq. (35)] in an average sense only, and is therefore less exact.

The boundary condition on the normal velocities [Eq. (1)] may be readily generalized to include the velocity perturbations due to the vortex systems. Assuming that the axial perturbation velocities are small compared to u_s and u_o , and utilizing Eq. (1), we obtain

$$\frac{\partial \varphi_{o\Gamma} / \partial r}{u_o} = \frac{\partial \varphi_{s\Gamma} / \partial r}{u_s} \quad (37)$$

which can be satisfied on the slipstream, $r = R$, for all x and θ by the placement of a suitable distribution of sources and sinks of strength proportional to the normal velocity jump. Following Ribner and Ellis, a reduced potential

$$\varphi'_{s\Gamma} = (u_o / u_s) \varphi_{s\Gamma} \quad (38)$$

is used inside the slipstream, so that the normal velocity jump is suppressed. In terms of $\varphi'_{s\Gamma}$, the pressure boundary condition [Eq. (36)] now becomes

$$\varphi'_{s\Gamma}(\infty, R, \theta) = (u_o / u_s)^2 \varphi_{o\Gamma}(\infty, R, \theta)$$

In terms of the potential jump $\Delta \varphi_{\Gamma} = \varphi_{o\Gamma} - \varphi'_{s\Gamma} = \Gamma(\theta)$, where $\Gamma(\theta)$ is the strength of the horseshoe vortex element on the slipstream at azimuthal angle θ , the pressure condition finally becomes

$$\Gamma(\theta) = (1 - \mu^2) \varphi_{o\Gamma}(\infty, R, \theta) \quad (39)$$

where it is recalled that $\mu = u_o / u_s$.

In the present treatment, Eq. (39) will be satisfied at each of M slipstream control points of azimuthal angle θ_m as shown in Figure 10.

For reasons of simplicity, the formulation will be given for single- and two-slipstream configurations only. Generalization to configurations with four slipstreams is straightforward, and has been incorporated into the

machine computational procedure.

Because of the symmetry conditions discussed previously, Eq. (39) may be satisfied only on the starboard wing panel, and θ_m may be limited to the range $0 < \theta_m < \pi$ ($0 < \theta_m < \pi/2$ for a single-slipstream configuration). Thus, we are led to a series of M equations of the form

$$\Gamma(\theta_m) = \frac{1-\mu^2}{2\pi} \left[P_{mj} \Gamma_j + P_{m(-j)} \Gamma_j + P_{mn} \Gamma_n - P'_{mn} \Gamma_n - P'_{m(-n)} \Gamma_n \right]$$

$$m = 1, 2, \dots, M \quad (40)$$

where the repeated subscript signifies a summation. The elements P_{mj} represent the contribution to the potential at θ_m , just outside the slipstream, arising from the trailing vortices of the j 'th wing horseshoe vortex element of unit strength and centered about $y = y_j$. P_{mj} is given in complex notation by

$$P_{mj} = \arg(Z_j + h_j - Z_m) - \arg(Z_j - h_j - Z_m) \quad (41)$$

Here $2h_j$ is the vortex spacing on the wing, $Z_j = y_j$, and $Z_m = y_p + R \exp(i\theta_m)$, where y_p is the coordinate of the slipstream axis. The elements $P_{m(-j)}$ represent the contribution to the potential at θ_m due to the image vortex system on the opposite wing panel, and are obtained from Eq. (41) through the relation

$$P_{m(-j)}(Z_j, h_j) = -P_{mj}(-Z_j, -h_j) \quad (42)$$

The elements P_{mn} represent the contribution to the potential at θ_m from a pair of trailing vortices of unit strength located on the upper half of the same slipstream at azimuthal angles $\theta_n \pm \Delta\theta_n/2$, and also from their images on the lower half of the slipstream. The vortex pair at $\theta_n = \theta_m$ is included. Because of the symmetry arising when the wing passes through the center of the slipstream, viz., $\Gamma(\theta_n) = -\Gamma(-\theta_n)$, it may be demonstrated that P_{mn} reduces to

$$P_{mn} = \delta_{mn} \quad (43)$$

where δ_{mn} is the Kronecker delta symbol (see Ribner, reference 6).

The elements P'_{mn} occur only for multi-slipstream configurations, and

represent contributions to the potential from the image vortex system on the upper half of the beam on the opposite wing panel. P'_{mn} may be written as

$$P'_{mn} = \arg \left[R \exp i (\pi - \theta_n + \Delta \theta_n / 2) - R \exp (i \theta_m) - 2y_p \right] \\ - \arg \left[R \exp i (\pi - \theta_n - \Delta \theta_n / 2) - R \exp (i \theta_m) - 2y_p \right] \quad (44)$$

Similarly, the $P'_{m(-n)}$ represent contributions from the lower half of the slipstream on the opposite wing panel, and may be obtained from Eq. (44) through the relation

$$P'_{m(-n)} (\theta_n, \Delta \theta_n) = - P'_{mn} (-\theta_n, -\Delta \theta_n) \quad (45)$$

Wing Boundary Condition

The condition that the resultant flow velocity is tangent to the effective wing surface at the i 'th control point along the 3/4-chord line becomes, in the slipstream coordinate system,

$$\tan \left[(\alpha_{eff})_i - \delta \right] = - (w_R / u)_i, \quad i = 1, 2, \dots, I \quad (46)$$

Here δ is the inclination of the vortex tube representing the slipstream, $(w_R)_i$ is the resultant Z component of velocity, and $(\alpha_{eff})_i$ is the effective angle of attack of the wing section measured with respect to the remote free stream direction \vec{V}_∞ . In accordance with thin airfoil theory, we define α_{eff} as the angle of attack of an equivalent flat plate airfoil which yields the same lift coefficient as a cambered and flapped section. Thus, we take

$$\alpha_{eff} = \alpha - \alpha_a + (\alpha_\delta) \delta_f + C_{l_a} / 2\pi \quad (47)$$

where α is the geometric angle of attack and may vary along the span due to geometric and aeroelastic twist, α_a is the ideal angle of attack of the section (the angle at which the pressure at the leading edge of the cambered mean line is finite), α_δ is the section flap effectiveness parameter at zero lift coefficient, δ_f is the flap deflection angle, and C_{l_a} is the ideal lift coefficient, i.e., the lift coefficient at $\alpha = \alpha_a$. The parameters α_a and C_{l_a} are tabulated in reference 16 for various airfoil

mean lines. The flap effectiveness α_δ is also given in reference 16 as a function of the flap/wing chord ratio.

For control points located outside the slipstreams, we take at the i 'th station

$$(u)_i = u_o$$

$$(w_R)_i = (w_\Gamma)_i + \sum_{k=1, 2, \dots}^K \left[(w_o - w_\infty)_k \right]_i + w_\infty \quad (48)$$

where $(w_\Gamma)_i$ is the z component of the velocity induced by all wing and slipstream horseshoe vortex systems at the control point, and w_{ok} is the z velocity component due to the k 'th inclined slipstream as obtained from Eq. (19). Thus, the multiple slipstream effects on the basic velocity field are approximated by superposition. A complete theory for multiple inclined actuator discs would involve additional interference velocities, inside as well as outside the slipstream, and has as yet not been accomplished.

As mentioned in the previous section, a reduced perturbation potential $\phi_\Gamma^i = \mu \phi_\Gamma$ is used inside a slipstream. In order that the form of Eq. (46) remain invariant across a slipstream boundary, it is required that all other velocity components, i. e., in addition to w_Γ , be reduced by a like factor. Therefore, for control points inside one of the slipstreams, say $k = l$, we take

$$(u)_i = \mu u_s = u_o \quad (49)$$

$$(w_R)_i = \left\{ w_\Gamma + \mu w_{sl} + \left[\frac{y - y_{pl}}{|y - y_{pl}|} \right] (v_\theta)_l + \mu \sum_{k \neq l}^K (w_o - w_\infty)_k \right\}_i$$

where w_{sl} is given by Eq. (20) and v_θ by Eq. (34).

All quantities in Eqs. (46) through (49) can be regarded as known at a particular control station except for $(w_\Gamma)_i$. Expressing $(w_\Gamma)_i$ in terms of the $\Gamma(y_j)$ and $\Gamma(\theta_n)$ gives

$$(w_\Gamma)_i = S_{ij} \Gamma(y_j) + S_{in} \Gamma(\theta_n) \quad (50)$$

where S_{ij} and S_{in} are influence coefficients which give the z velocity

component induced at the i 'th control point by wing and slipstream horseshoe vortex elements of unit strength and by their images. Expressions for S_{ij} and S_{in} may be obtained directly from the Biot-Savart law, e.g., reference 17.

VELOCITY FIELD AND DOWNWASH ANGLES

Once the strengths of the vortex elements have been obtained, the resultant velocity $\hat{V}_R(x, y, z)$ in the flow field may be obtained in a straightforward manner. Outside a slipstream, \hat{V}_R is found from

$$\hat{V}_R = \hat{V}_{R0} = \hat{V}_\Gamma(x, y, z) + \sum_{k=1}^K \left[\hat{V}_0(y, z) - \hat{V}_\infty \right]_k + \hat{V}_\infty \quad (51)$$

where $\hat{V}_\Gamma(x, y, z)$ is the resultant velocity induced at the point (x, y, z) in the slipstream coordinate system by all vortex elements on the wing and slipstreams and is obtained from the Biot-Savart law. The velocity contributions from the inclined slipstream are obtained by superposition, as indicated by the summation over k .

Inside a slipstream the induced velocity \hat{V}_Γ and the vortex elements Γ_j must be augmented by the factor $(1/\mu)$ to correspond to the physical perturbation velocity and vortex strength. We therefore obtain for \hat{V}_R inside the l 'th slipstream

$$\begin{aligned} \hat{V}_R = (\hat{V}_R)_{sl} = \frac{1}{\mu} \hat{V}_\Gamma(x, y, z) + \sum_{k \neq l}^K \left[\hat{V}_0(y, z) - \hat{V}_\infty \right]_k \\ + \left[\hat{V}_s(y, z) \right]_l + \left[\hat{v}_\theta(y, z) \right]_l \end{aligned} \quad (52)$$

Of importance in the estimation of the static stability and control of $V/STOL$ as well as of conventional aircraft are the dynamic pressure ratio q/q_∞ , the downwash angle ϵ , and the stability parameter $d\epsilon/d\alpha$. These quantities may readily be found from \hat{V}_R . For convenience in presentation, we shall express these parameters in free stream coordinates (x', y', z') rather than in the slipstream coordinates (x, y, z) used in the theoretical development. The two coordinate systems are related by a simple rotation as shown in Figure 1.

The dynamic pressure ratio is given by

$$q(x', y', z')/q_\infty = \hat{V}_R \cdot \hat{V}_R / V_\infty^2 \quad (53)$$

The resultant downwash angle $\epsilon(x', y', z')$ is defined as the angle which the projection of \hat{V}_R in the plane $y' = \text{constant}$ makes with \hat{V}_∞ , and is given by an expression similar to Eq. (33).

The parameter $d\epsilon/d\alpha$ must be evaluated in a body fixed coordinate system, because the tail is assumed to rotate rigidly with the wing as the angle of attack is changed. Thus, $d\epsilon/d\alpha(x', y', z')$ is evaluated numerically from the expression

$$d\epsilon/d\alpha = \left[\epsilon(\alpha, x', y', z') - \epsilon(\alpha + \Delta\alpha, x' + \Delta x', y', z' + \Delta z') \right] / \Delta\alpha \quad (54)$$

where $\Delta x' = z' \Delta\alpha$ and $\Delta z' = -x' \Delta\alpha$.

RESULTANT FORCE AND SPAN LOADING

Outside the slipstreams, the force per unit span \hat{n} may be found from the expression

$$\hat{n} = \hat{n}_o(y_i) = \rho \hat{\Gamma}(y_i) \times \hat{V}_{Ro}(0, y_i, 0) \quad (55)$$

where $x = z = 0$ corresponds to the 1/4-chord line. Inside a slipstream, because of the augmentation of the circulation and induced velocities, we take

$$\hat{n} = \hat{n}_s(y_i) = \rho (\hat{\Gamma}(y_i)/\mu) \times \hat{V}_{Rs}(0, y_i, 0) \quad (56)$$

It should be noted that \hat{n} is the resultant of the local lift and induced drag per unit span, because induced velocities have been included in \hat{V}_R . The direction of \hat{n} will vary across the span, and the overall lift force \hat{L} and drag \hat{D} may be obtained by integrating the components of \hat{n} perpendicular to and parallel to \hat{V}_∞ across the span.

The span loading $n(y)$ must be continuous, even across a slipstream interface, because of pressure continuity. The circulation $\Gamma(y_i)$ is therefore discontinuous across the slipstream interface (a similar discontinuity occurs for $\Gamma(\theta_m)$ across the wing, reference 7). In the present discrete vortex formulation, $\Gamma(y_i)$ and $\Gamma(\theta_m)$ are not necessarily continuous, and jumps in their values will automatically occur across the slipstream

interface as required by the boundary conditions. This is in contrast with the formulation by Ribner and Ellis wherein the jumps in Γ are explicitly prescribed and can unduly complicate the analysis for multiple slip-streams.

SAMPLE CALCULATIONS AND COMPARISON WITH DATA

Several sample calculations have been carried out to compare the present discrete vortex formulation with the calculations by Ribner and Ellis and with experimental data.

A comparison of the calculated span load distribution with that from reference 8 is given in Figure 11 for a wing with a single untilted slipstream. According to Ribner and Ellis, discontinuities in the wing vortex strength are required across the slipstream interface $r = R$ such that

$$\Gamma(R+0) - \Gamma(R-0) = (1 - \mu^2) \Gamma(R+0)$$

whereas a similar jump in slipstream vortex strength is required across the wing. As shown in Figure 11, jumps of approximately this magnitude were obtained with the discrete vortex formulation.

A comparison of the calculated span loadings and downwash angle with test data by Stüper (reference 4) is found in Figures 12 through 16. Shown in Figures 12 and 13 are the span loading and downwash angle distribution, respectively, for a wing in the slipstream of an untilted ducted fan with straightener vanes to remove swirl effects. Good agreement is found except at $\alpha = 12^\circ$, for which the wing has probably stalled.

A similar comparison, however, for a wing with a single untilted propeller, is given in Figures 14 and 15. Because the present theory is limited to symmetrical span load distributions, slipstream swirl can only be included for two- and four-propeller configurations. The experimental span loading and downwash data were therefore averaged (right and left wing panels) before being plotted in Figures 14 and 15 for comparison with theory. Once again, reasonable agreement is found, except for the highest α , where stall occurs, and except for some differences attributed to scatter.

A similar span loading comparison, for a single propeller inclined upward 6° with respect to the wing zero lift angle, is shown in Figure 16. Again, average experimental data were used.

Although many more test data are available in reference 4 for comparison with theory, all data are for relatively small propellers at small inclination angles. Tests of comparable detail but for propeller sizes and tilt angles more representative of V/STOL configurations and operational conditions are required to substantiate the theory.

This requirement has been partially met by the half-model tests of reference 14, wherein span loading data were obtained by testing a segmented wing and propeller simulating a two-engine V/STOL aircraft at large tilt angles. A comparison between the present theory, including effects of slipstream swirl, and representative data from reference 14 is given in Figures 17 and 18. Satisfactory agreement is shown at angles of attack

and propeller inclination angles at or below 20° , for which wing stall effects and wind tunnel wall interference effects are probably small. The test data at larger incidence angles and for thrust coefficients $T_C'' \geq 0.90$ have not been included in the comparison, because stall and wall interference effects have been observed in the data.

Although no general downwash angle survey is available for large tilt angles, i.e., on a scale comparable to that of reference 4 at small tilt angles, it is still possible to obtain average values of the downwash angle at the tail location from tail-on and tail-off wind tunnel test data. Such data (reference 18) are compared with the theory in Figure 19. The test model was a 1/11-scale version of the four-engine tilt-wing configuration shown in Figures 36 through 50. The experimental downwash angle was taken as the tail incidence angle with respect to the remote free-stream direction at which both tail-on and tail-off pitching moment coefficients were equal, and represents an average value across the tail span. The theoretical downwash angle was calculated at the location of the horizontal tail $c/4$ -line in the plane $y/(b/2) = 0.325$ (70% of the tail semispan). Corrections were made in the theory for the vertical displacement of the wing wake and of the slipstream interface by shifting these boundaries an amount equal to the calculated displacement of the wing wake (see Design Charts).

As shown in Figure 19, satisfactory agreement was found for $\epsilon \leq 10^\circ$. For test conditions (α , T_C'' , δ_f) which resulted in downwash angles in excess of 10° , the experimental values for ϵ were significantly greater than calculated from theory. One possible explanation for this disagreement is that the slipstream and wing wake are deformed in such a manner that their downward displacement below the vertical tail is appreciably reduced. Thus, it is known that a completely rolled-up wake is displaced downward by only $2/\pi^2$ of the displacement of a plane vortex wake from an elliptically loaded wing (reference 19). Although wake roll-up generally occurs behind the tail position at moderate lift coefficients and large aspect ratios, slipstream effects might well accelerate the roll-up process, because of the low effective aspect ratios of the wing segments inside the slipstream (see Introduction). Similar results were noted by Heyson and Katzoff (reference 20), who observed a very rapid roll-up of the rotor slipstream. They found that the rolled-up vortices had been displaced downward only about one-half as far as the calculated momentum wake.

In lieu of a complete wake theory, which includes slipstream deformation and wake roll-up, it was decided to correct for these effects by using only one-half of the calculated undeformed wake displacement (or, equivalently, to shift the tail downward by this amount). Substantially improved agreement with the data from reference 18 was thereby obtained, as shown in Figure 20.

Because of the lack of sufficient test data at large tilt angles, it was decided to forego any modification of the theory for slipstream deformation and roll-up effects until further evaluation and comparison with test data could be carried out.

DESIGN CHARTS

Knowledge of the structural, aerodynamic, longitudinal stability, and control characteristics of V/STOL aircraft requires information on the span load distribution and on the wake velocity field. In order to supply the aircraft design engineer with data for making a rational estimate of these characteristics, design charts have been prepared for the span loading $C_n''(y)$, downwash angle ϵ , stability parameter $d\epsilon/d\alpha$, and dynamic pressure ratio q/q_∞ as obtained from the present lifting surface theory (Figures 21 through 50).

The design charts were prepared for twin-propeller and four-propeller tilt-wing configurations with wing and flap planforms taken similar to the Canadair CL-84 and the Ling-Temco-Vought XC-142a aircraft, respectively. The flight conditions and aerodynamic parameters (e.g., α , α_p , T_c'' , δ_f , J , etc.) were chosen as representative of V/STOL aircraft operations in the hover, transitional, and cruise regimes. Thus, the figures may be considered an extension of the cruise design charts by Silverstein and Katzoff (reference 21) to conditions wherein inclined slipstream effects are of significance.

The data for the charts were obtained from the computer program described in Appendix III. Running time was approximately 30 seconds per case. The data for ϵ , $d\epsilon/d\alpha$, and q/q_∞ are presented in the form of contour plots in the vertical planes $y/(b/2) = 0.40$ and 0.325 , which were assumed representative of the average spanwise horizontal tail stations for two- and four-propeller aircraft, respectively. Considerable data smoothing was required, because the discrete vortex formulation gives spurious results at points near the singularities. Although all computations are carried out in the slipstream coordinate system (x, y, z) , the contour plots are presented for convenience in the free stream coordinate system (x', y', z') as discussed previously.

It is noted that no wake roll-up or slipstream distortion effects are included. In this respect, the charts are similar to those in reference 21. However, because of the large angles of attack, effects of the vertical displacement of the wake have been approximated by shifting the contour plots by an amount $\Delta z(x, y)$ where

$$\Delta z = \int_0^x w_R(x, y, 0) dx .$$

This results in both the slipstream boundaries and wing vortex wake being displaced downward by an amount equal to the displacement of the wing vortex wake. As pointed out in the previous section, slipstream deformation and wake roll-up will reduce the vertical displacement below that

shown in the design charts. In lieu of a calculation procedure which considers slipstream deformation and roll-up, the present charts might be corrected for these effects by displacing the tail position by an amount equal to the change in the displacement of the slipstream or wing wake. The physical displacement has been estimated to be approximately one-half the calculated displacement Δz shown on the charts for large tilt angles.

The design charts include the effects of slipstream rotation with viscous core effects reducing the swirl velocities to zero along the streamline passing through the propeller axis. All computations were made with the value $\nu_t = 0.10 \text{ ft}^2/\text{sec}$, as obtained from wind tunnel data, with no scaling for aircraft size. The effective turbulent origin Ω was taken as 200 ft. and 400 ft. for the two- and four-slipstream configurations, respectively.

Jumps in the quantities ϵ , $d\epsilon/d\alpha$, and q/q_∞ occur across the slipstream interface, as previously noted in the section dealing with the inclined actuator disc theory (e.g., Figure 5). Values of $d\epsilon/d\alpha$ were obtained from Eq. (54) using an incremental $\Delta\alpha = 0.5^\circ$. The value of $d\epsilon/d\alpha$ is actually undefined at the slipstream interface, and the values shown are limiting values obtained by extrapolation from inside and outside the slipstream. Viscous effects will probably play a role in smoothing out these jumps. Viscous effects are also known to modify the downwash angle and dynamic pressure contours near the vortex wake of the wing, because of dynamic pressure losses caused by skin friction on the wing. Corrections for the latter effect are given in reference 21, and require the introduction of the wing profile drag coefficient C_{D_o} as an additional parameter.

CONCLUSIONS AND RECOMMENDATIONS

A theory has been developed for an inclined actuator disc which satisfies the normal velocity and nonlinear pressure boundary conditions. This theory has been used as the basis for the development of a wing lifting surface theory with inclined slipstreams for application to V/STOL aircraft in the transitional regime. The lifting surface theory has been programmed on the CDC 3600 digital computer. Sample calculations have been carried out to compare with available test data and also to present design charts of span loading, downwash angle, $d\epsilon/d\alpha$, and dynamic pressure in the wake for typical V/STOL aircraft.

Comparison with test data has shown that the theory predicts the span loading and downwash angle reasonably well for small angles of attack and small propeller tilt angle. However, at large tilt angles the theory (with an undeformed, but displaced, slipstream and wake) tends to predict significantly lower downwash angles in the tail region than observed from a single set of test data, possibly due to slipstream deformation and wake roll-up which tend to reduce the downward wake displacement. Use of only one-half of the calculated wake displacement gave improved agreement with measured downwash angles at these conditions. However, the lack of sufficiently detailed test data for conditions representative of V/STOL transition makes evaluation of the theory and assessment of its limitations difficult.

In order to evaluate the theory, a test program is required for a wing-propeller configuration at large angles of attack and large propeller tilt angles with slotted flaps and slats to prevent separation. Measurements should include span load distribution, separate overall wing and propeller force and moment coefficients, and a survey of downwash angle and dynamic pressure inside and outside the slipstream. Improvement of the theory for effects of slipstream deformation, wake roll-up, etc., could be carried out following experimental justification.

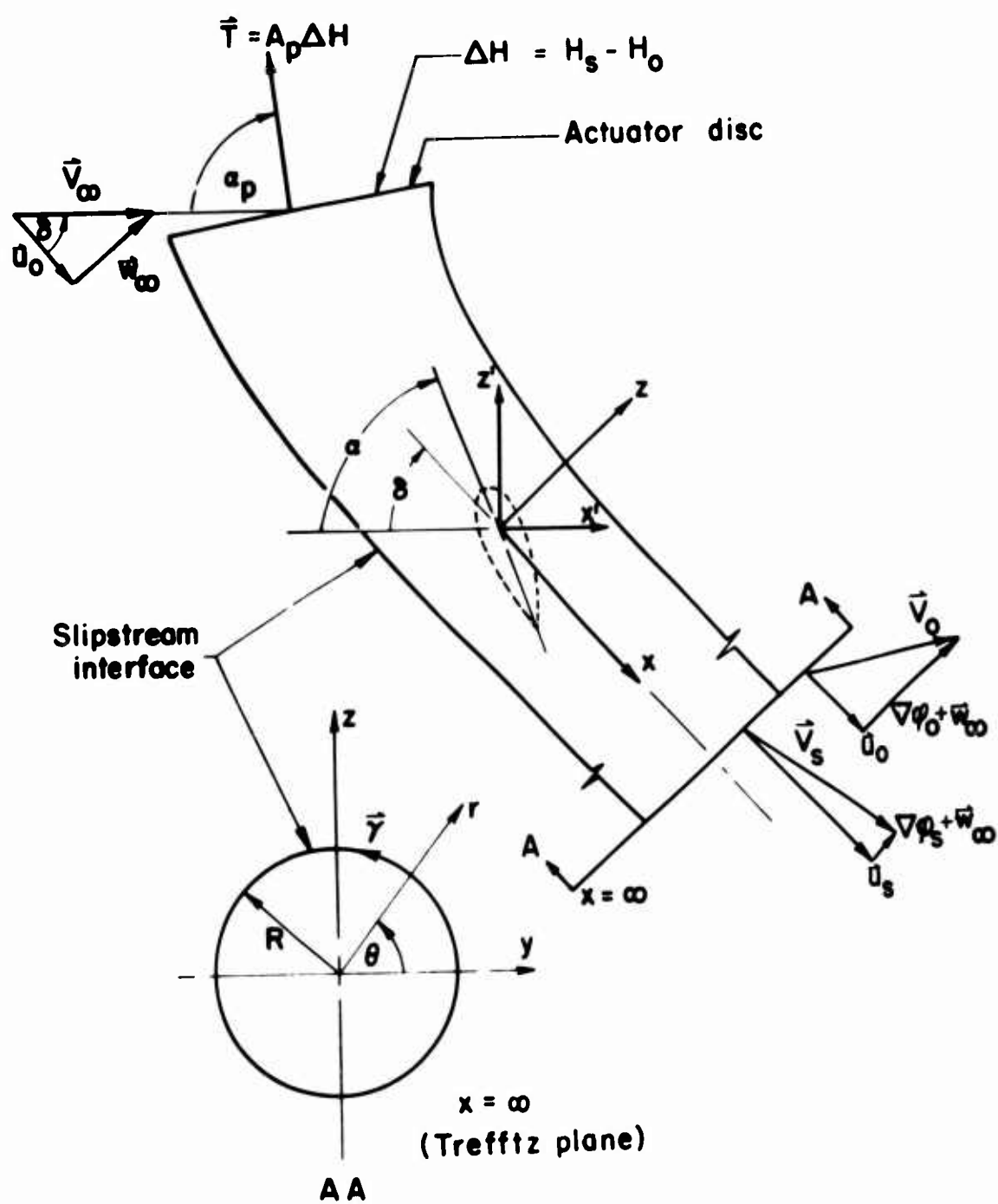


Figure 1. Flow Model and Coordinate Systems, Inclined Actuator Disc Theory

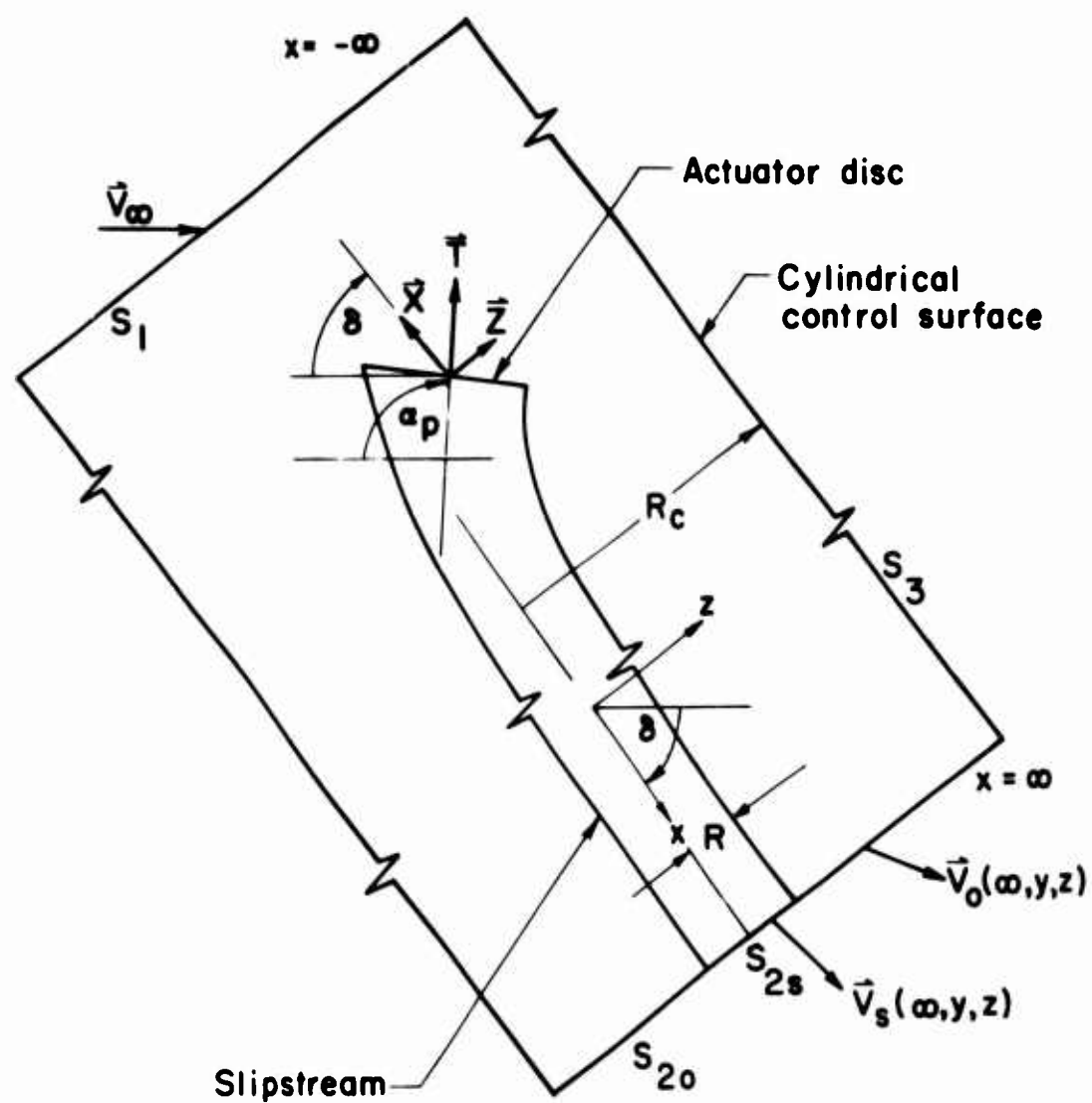
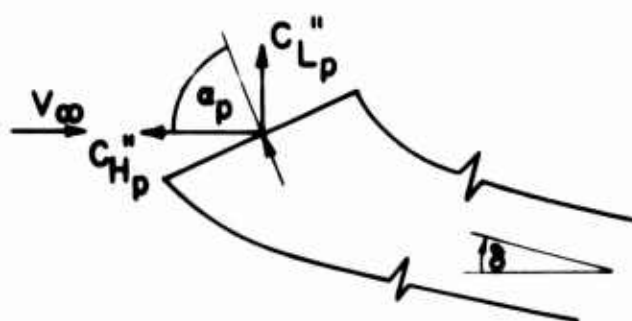


Figure 2. Control Surface for Determination of Forces and Power, Inclined Actuator Disc Theory.



$$T_c'' = \frac{\Delta H}{q_\infty + \Delta H}$$

$$C_{Lp}'' = \frac{\text{Vertical force}}{A_p(q_\infty + \Delta H)}$$

$$C_{Hp}'' = \frac{\text{Horizontal force}}{A_p(q_\infty + \Delta H)}$$

δ is the slipstream
vortex tube angle

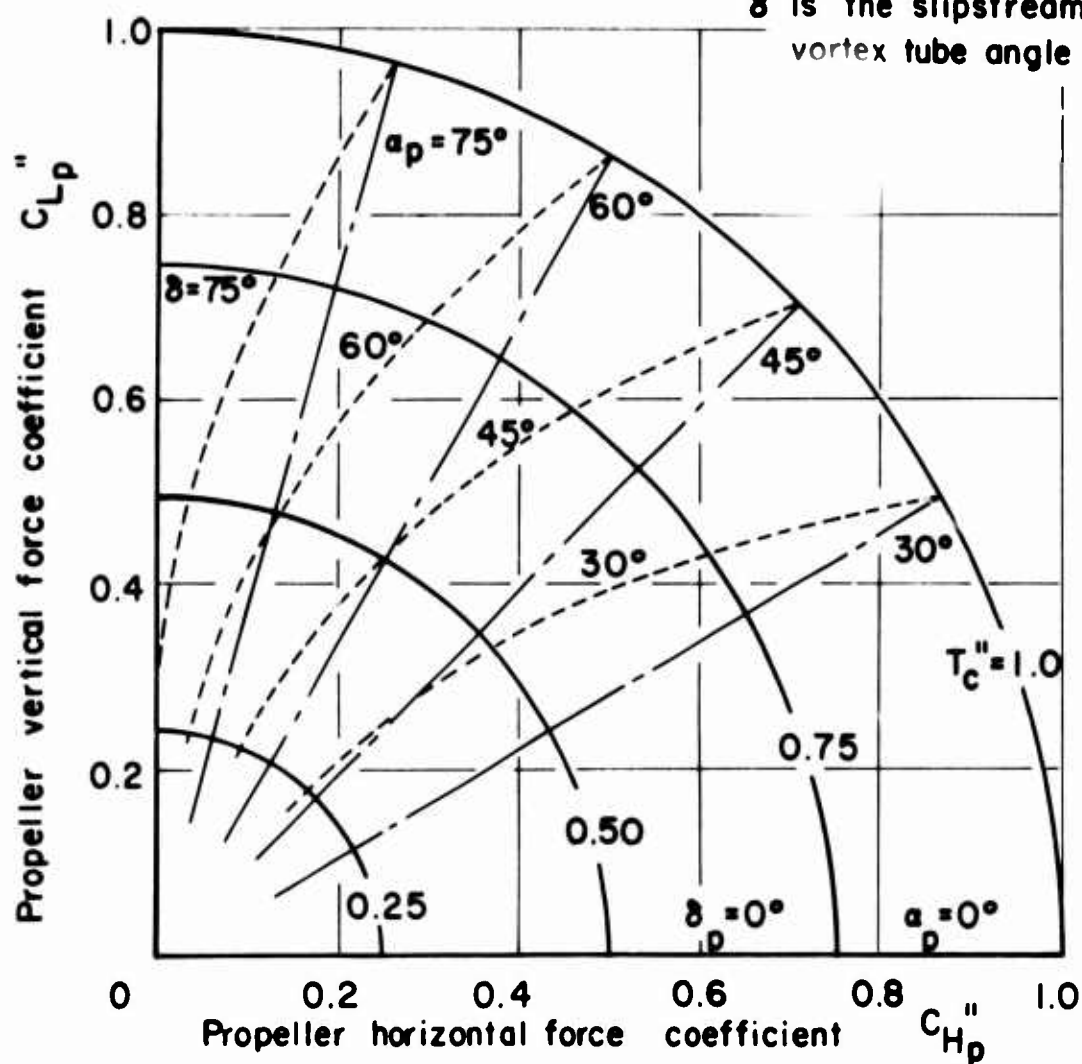


Figure 3. Vortex Tube Angle, Inclined Actuator Disc Theory.

P is power added to slipstream

Test points from reference II assume $\Delta H = T/A_p$
and are corrected for ideal efficiency

$$\circ T_c'' = 0.50$$

$$\triangle T_c'' = 0.71$$

$$\square T_c'' = 0.91$$

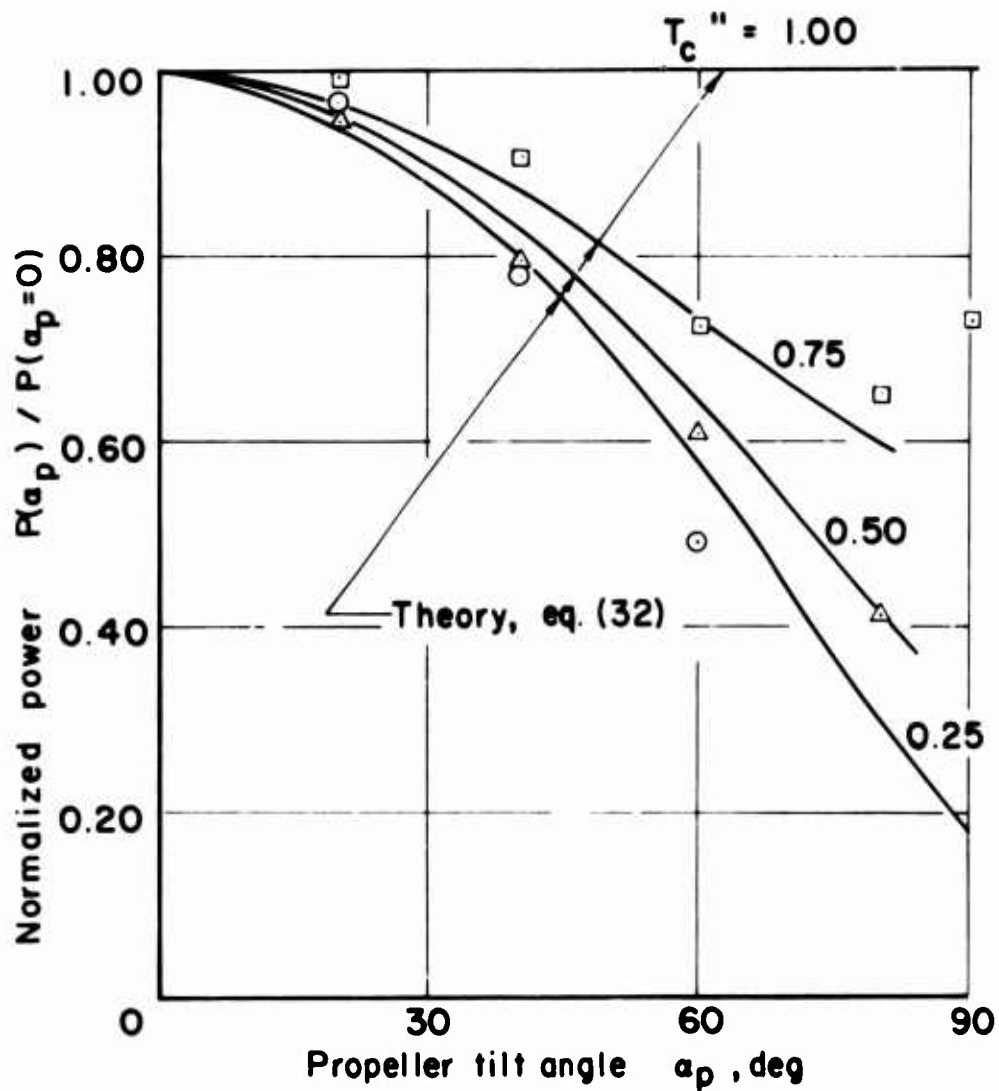


Figure 4. Variation in Power Required With Propeller Tilt Angle From Inclined Actuator Disc Theory.

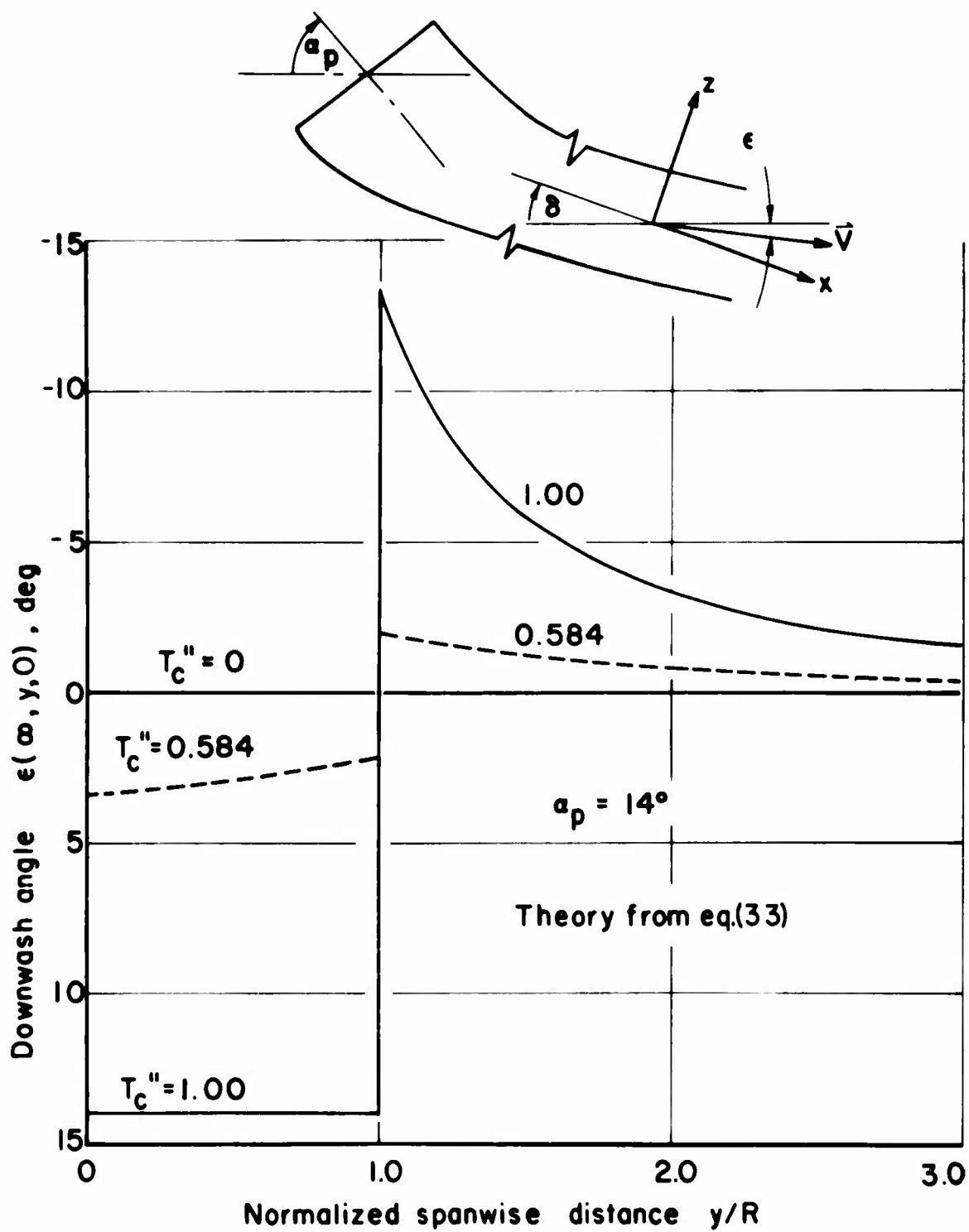


Figure 5. Downwash Angle Across Slipstream Centerline, Inclined Actuator Disc Theory.

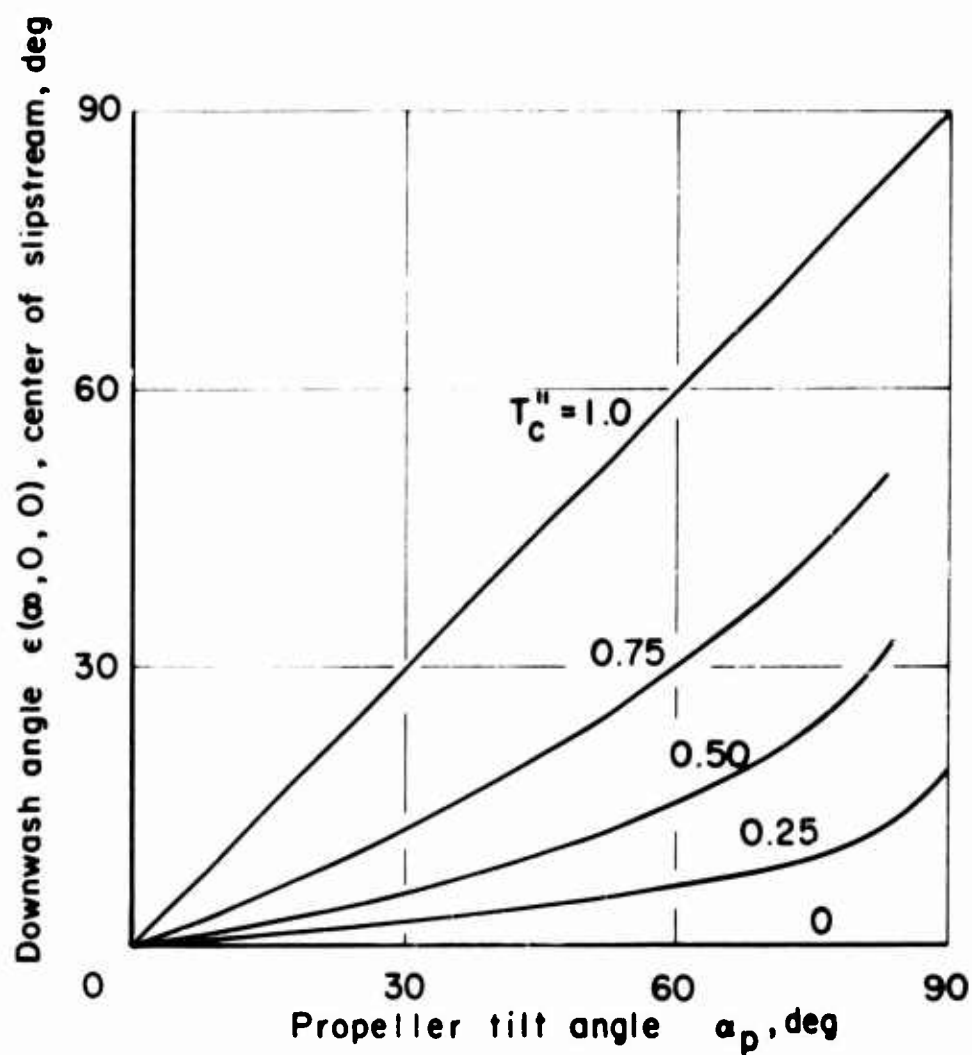
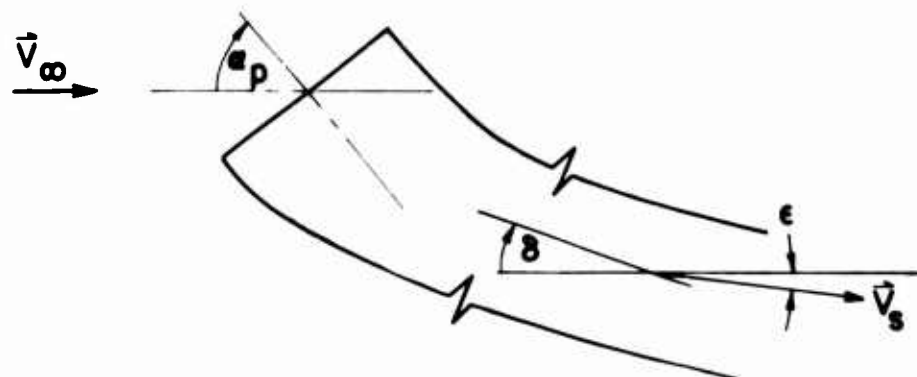


Figure 6. Theoretical Downwash Angle on Slipstream Centerline, Inclined Actuator Disc Theory.

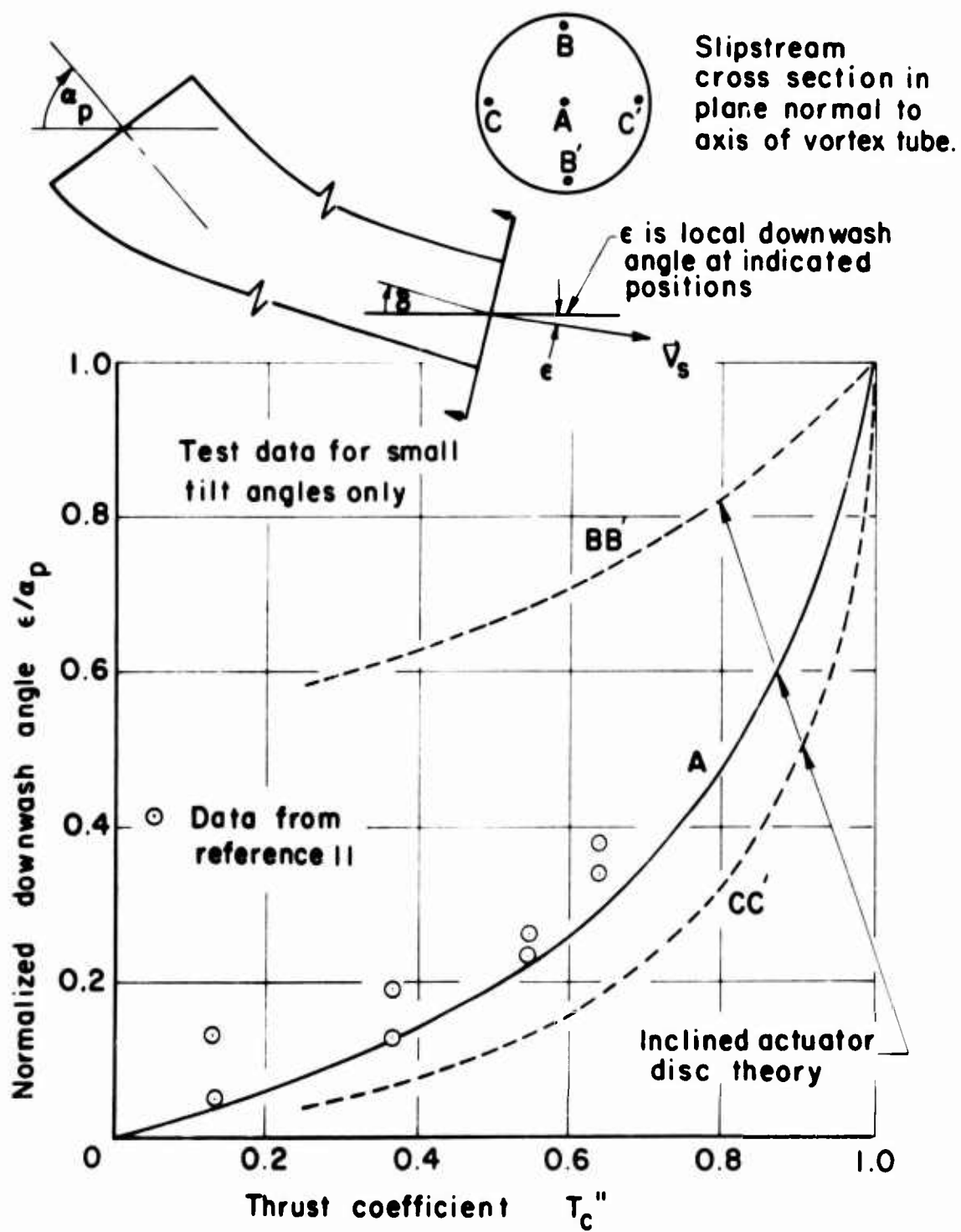


Figure 7. Comparison With Slipstream Downwash Angle Test Data.

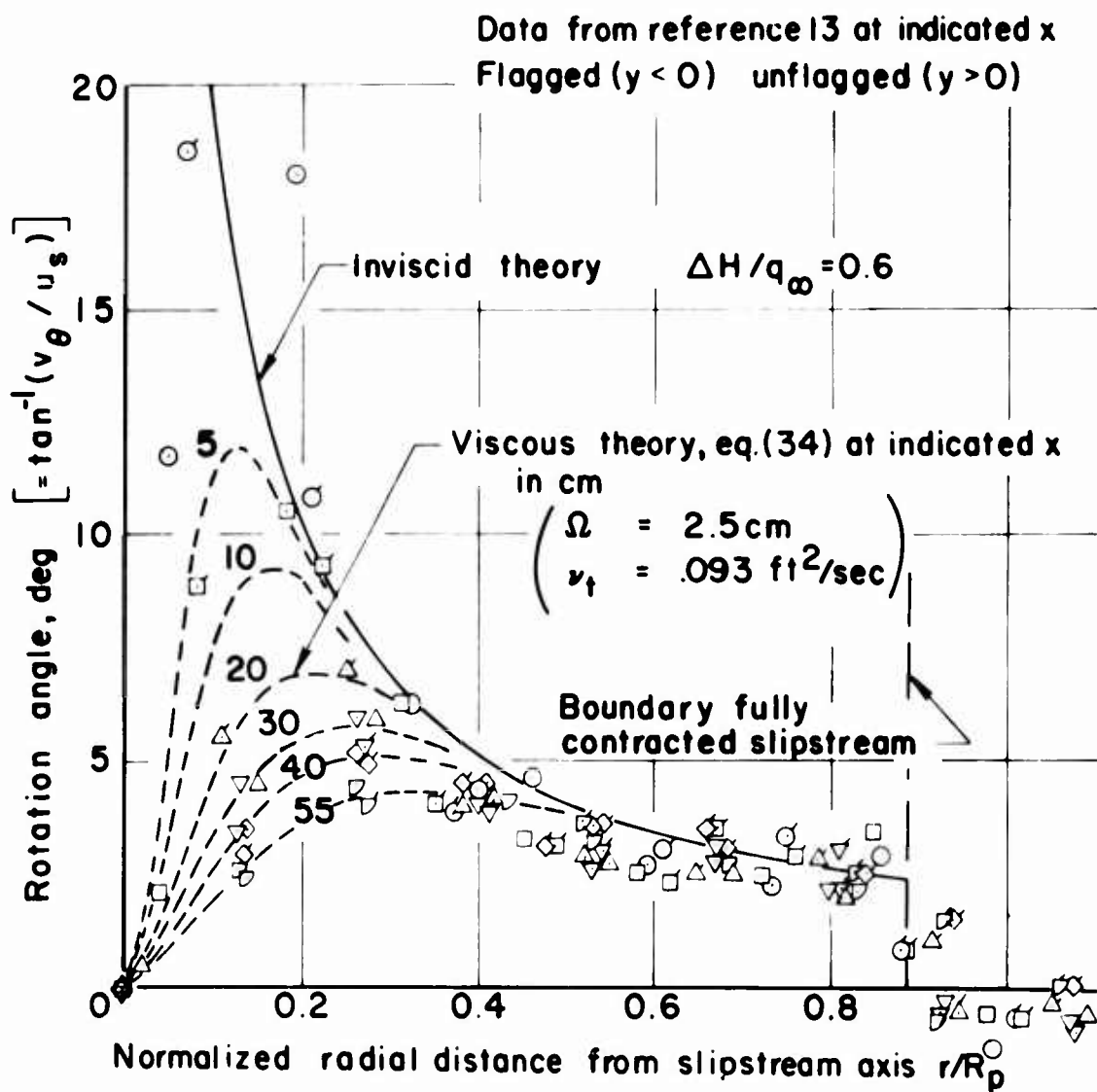
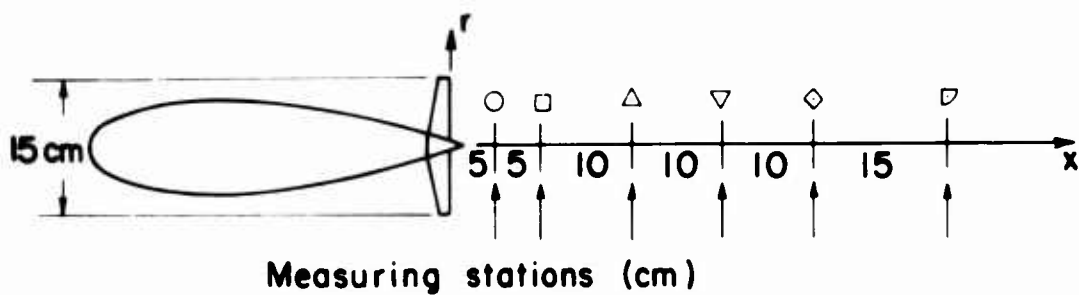


Figure 8. Comparison With Slipstream Rotation Angle Test Data From Reference 13.

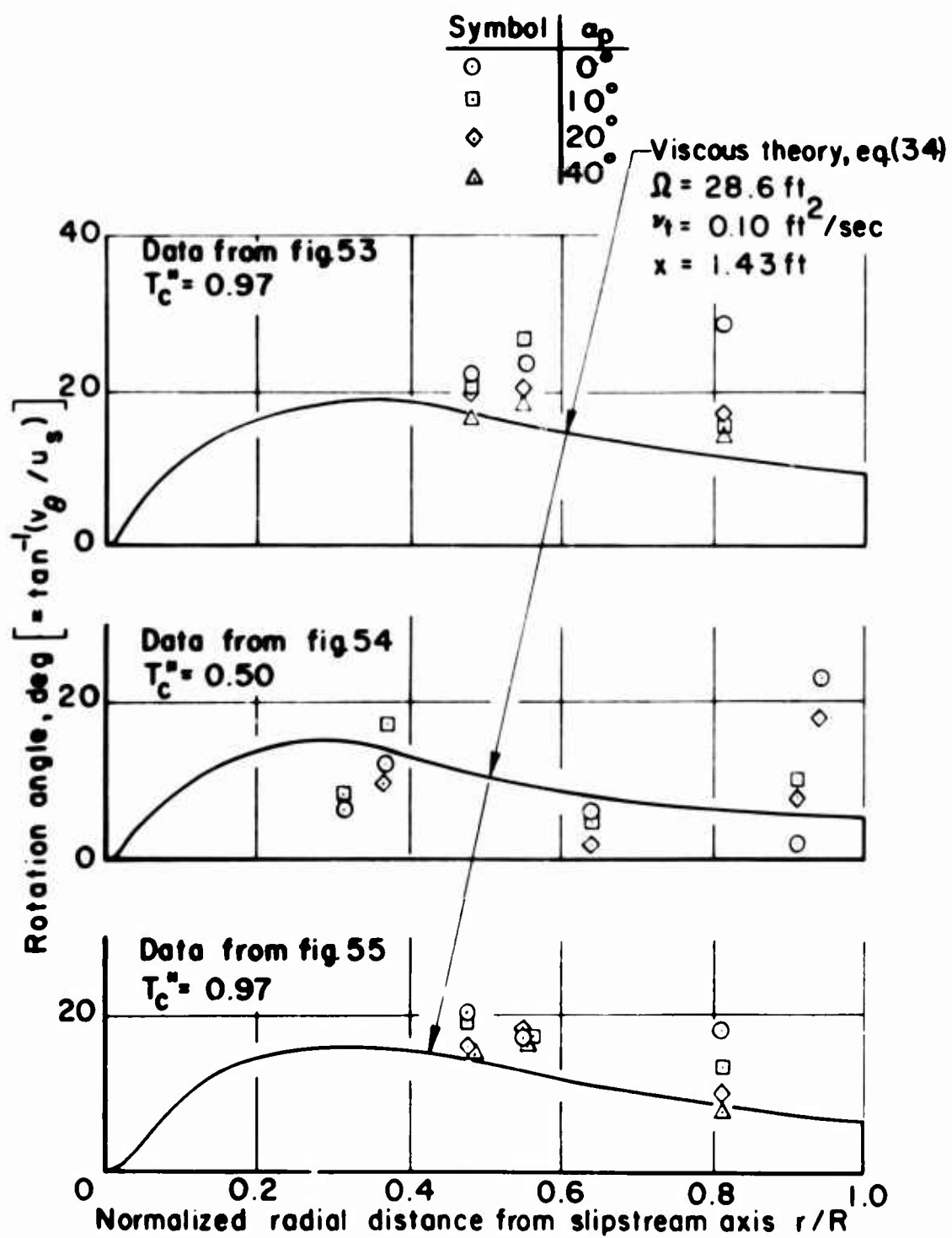


Figure 9. Comparison With Slipstream Rotation Angle Test Data From Reference 14.

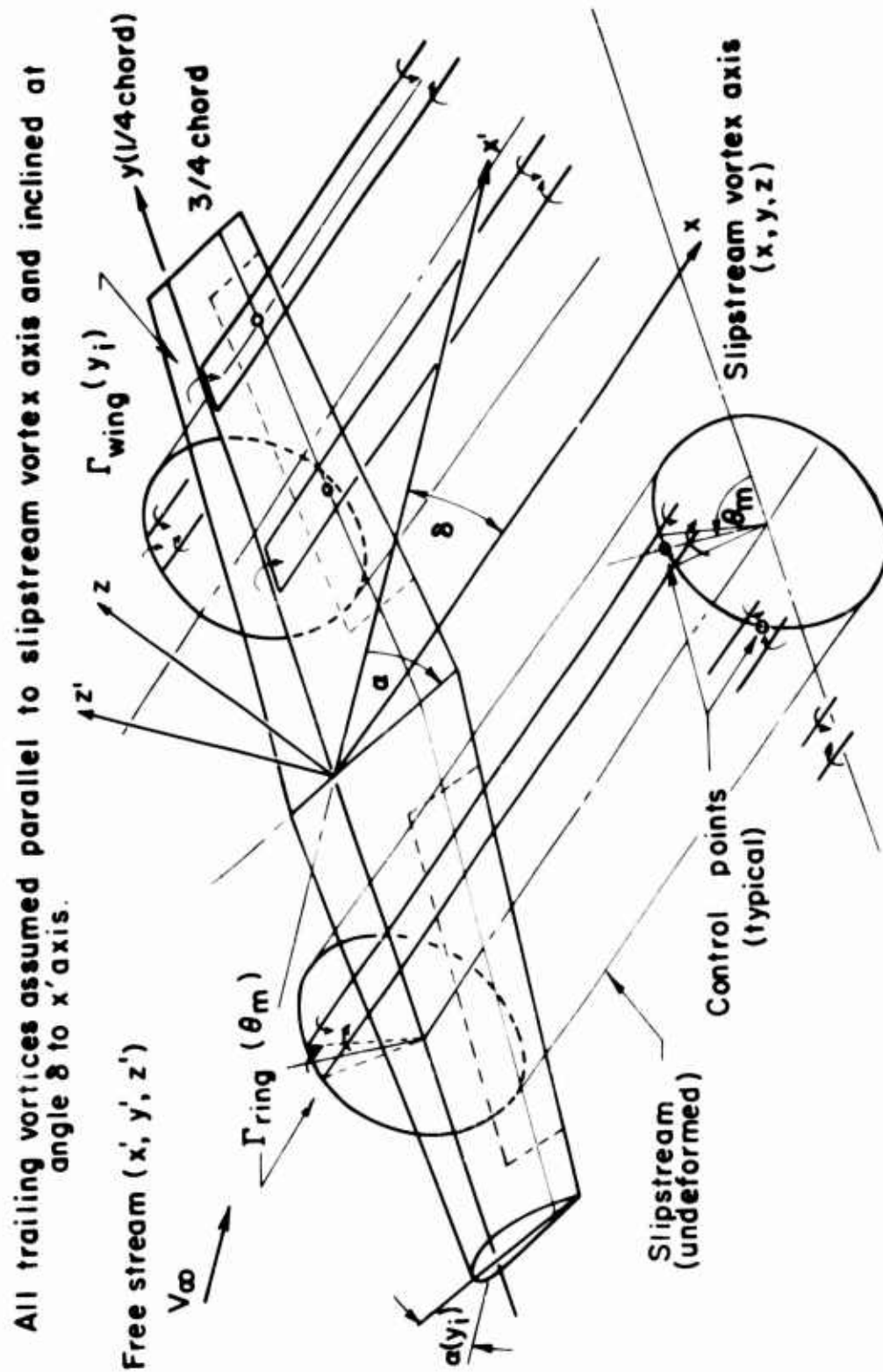


Figure 10. Vortex Singularities for Lifting Surface Theory With Inclined Slipstream.

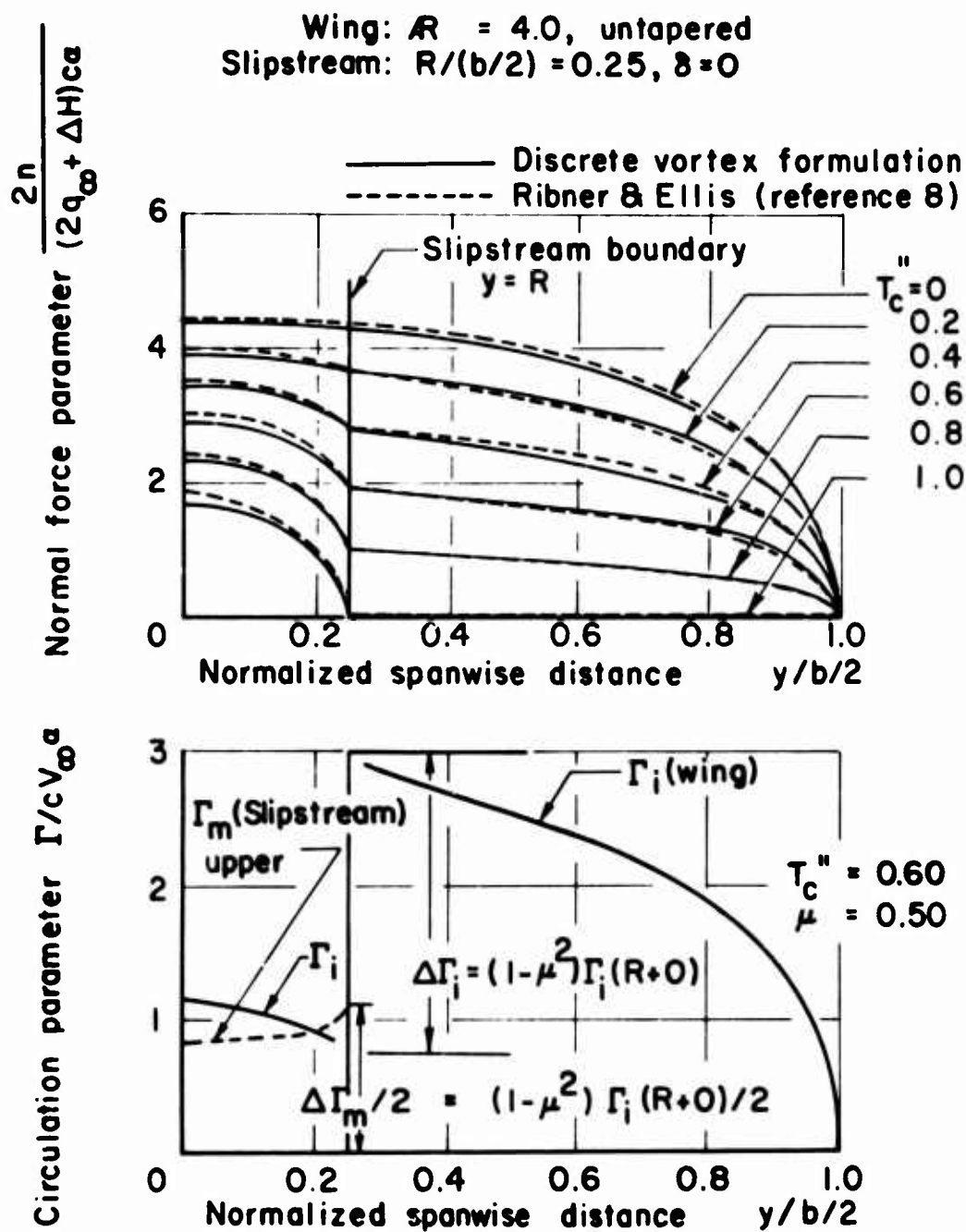


Figure 11. Comparison of Discrete Vortex Formulation Loadings and Vortex Strength With Theory of Ribner and Ellis.

Untilted ducted fan, $T_c'' = 0.46$
 $R = 6\text{cm}$, $c = 20\text{cm}$

—— Theory, $T_c'' = 0$
 ---- Theory, $T_c'' = 0.46$
 Data from reference 4
 ○ No fan, $\Delta T_c'' = 0.46$

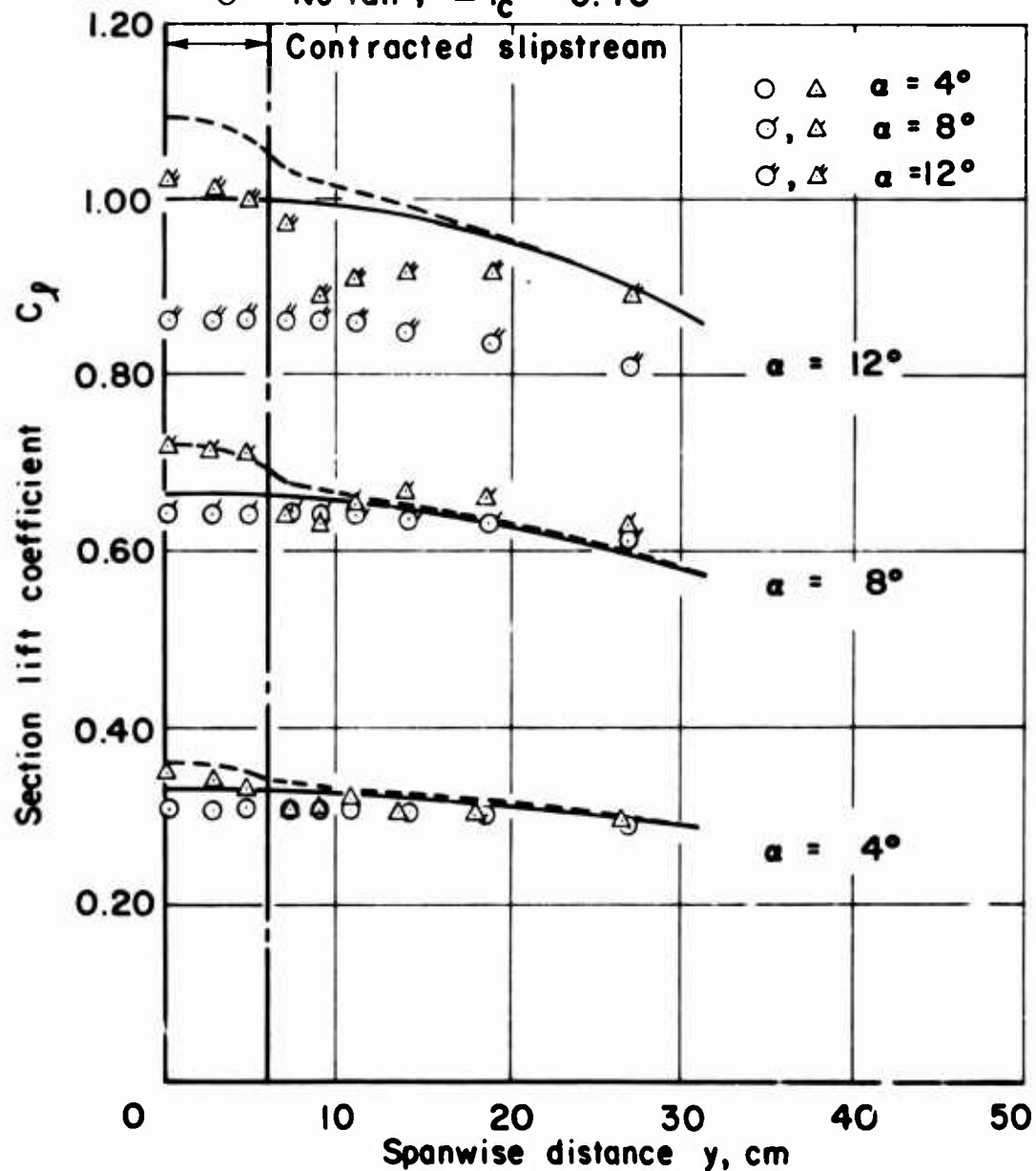


Figure 12. Comparison of Span Load Distribution With Test Data, Single Untilted Ducted Fan With Wing.

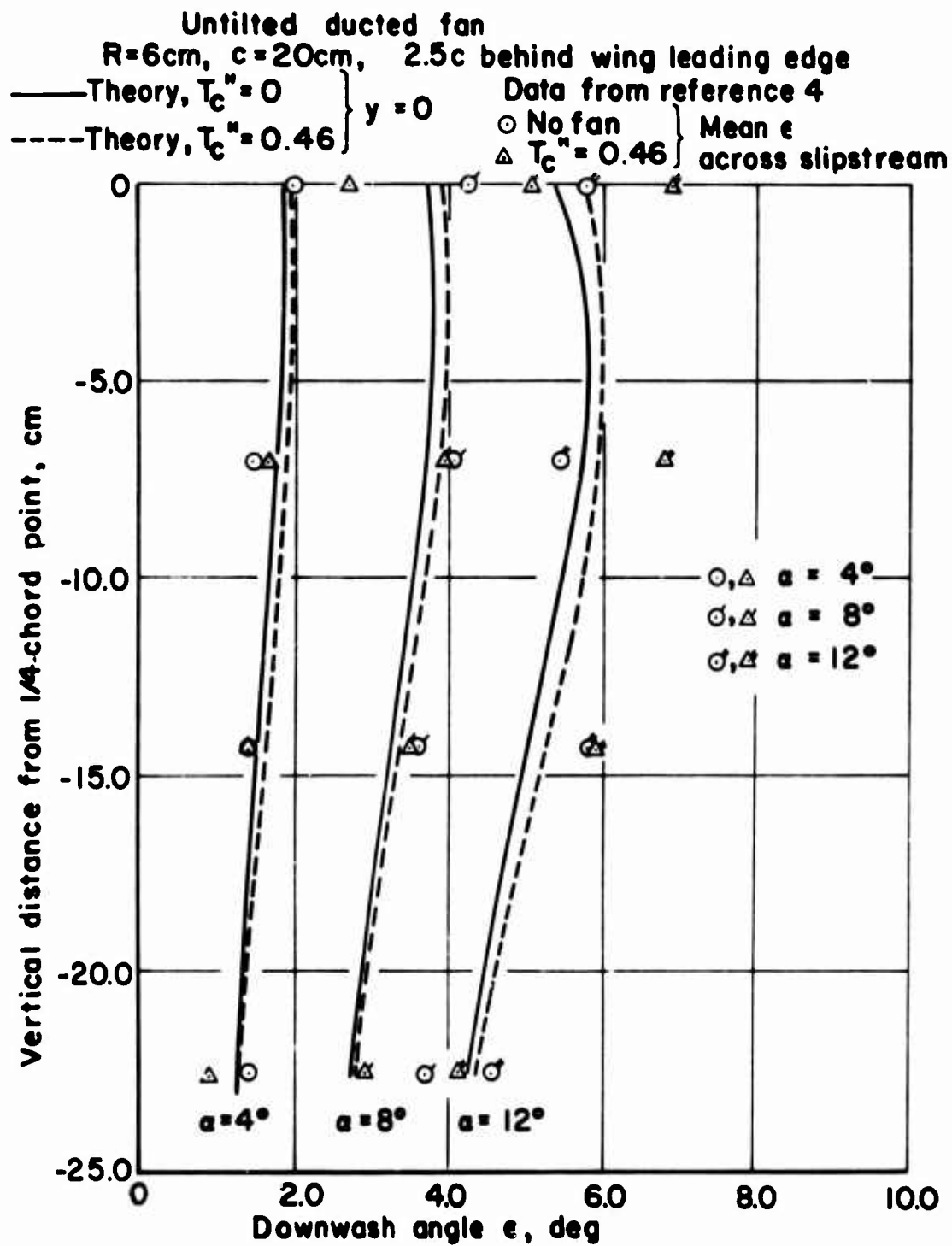


Figure 13. Comparison of Downwash Angles With Test Data, Single Untilted Ducted Fan With Wing.

Untilted propeller, $T_c'' = 0.375$
 $k_p = 7.5 \text{ cm}$, $R = 7 \text{ cm}$, $c = 20 \text{ cm}$

— Theory
 ○ Data from reference 4

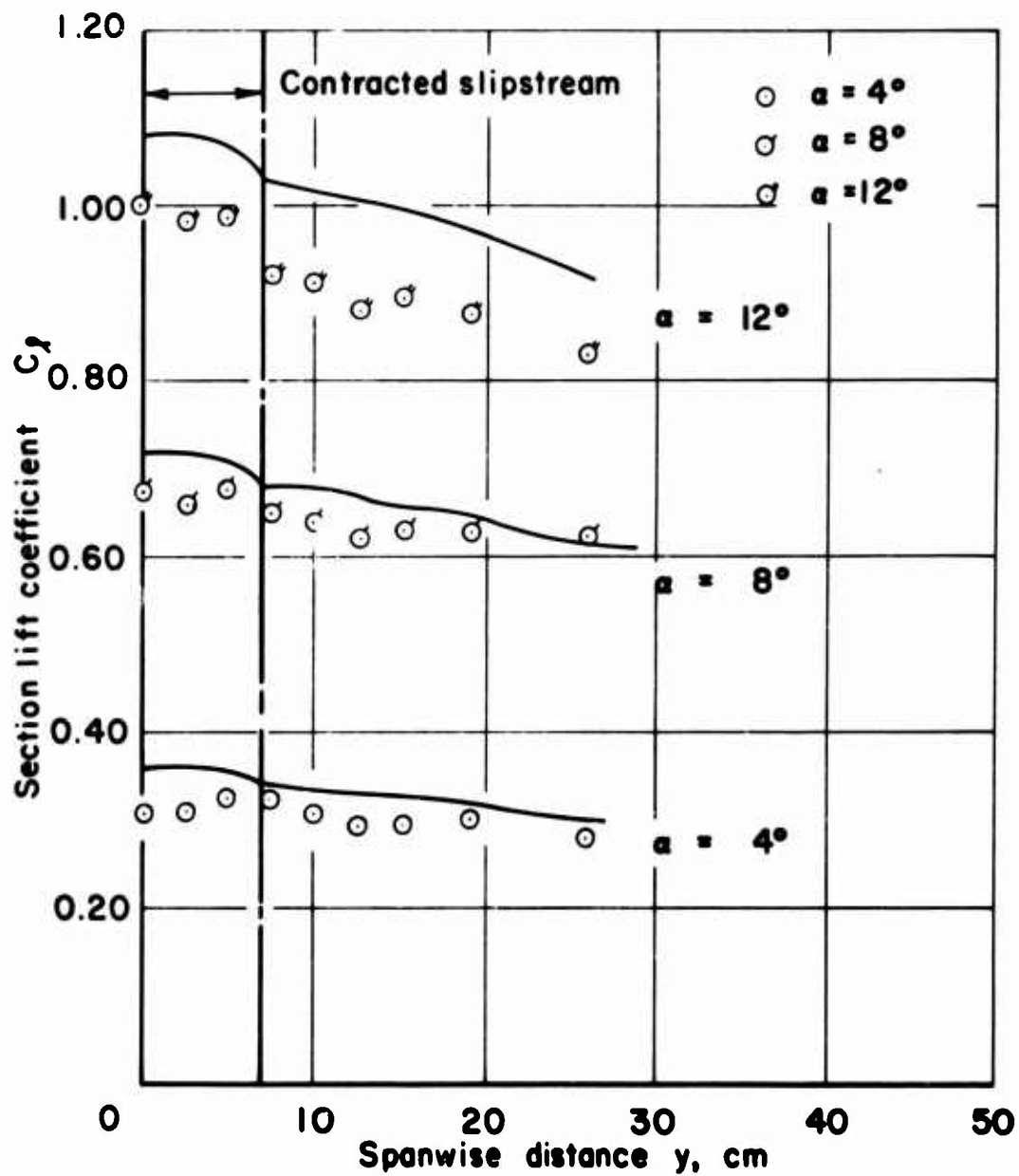


Figure 14. Comparison of Span Load Distribution With Test Data, Single Untilted Propeller With Wing.

Untilted propeller, $T_c'' = 0.375$
 $R_p = 7.5\text{cm}$, $c = 20\text{cm}$, $2.5c$ behind wing leading edge
 Theory, — $y = 0\text{cm}$, - - - $y = 5\text{cm}$, — — — $y = 15\text{cm}$

Data from reference 4

○ $y = 0\text{cm}$, □ $y = 5\text{cm}$, △ $y = 15\text{cm}$

○, □, △ $\alpha = 4^\circ$

○, □, △ $\alpha = 8^\circ$

○, □, △ $\alpha = 12^\circ$

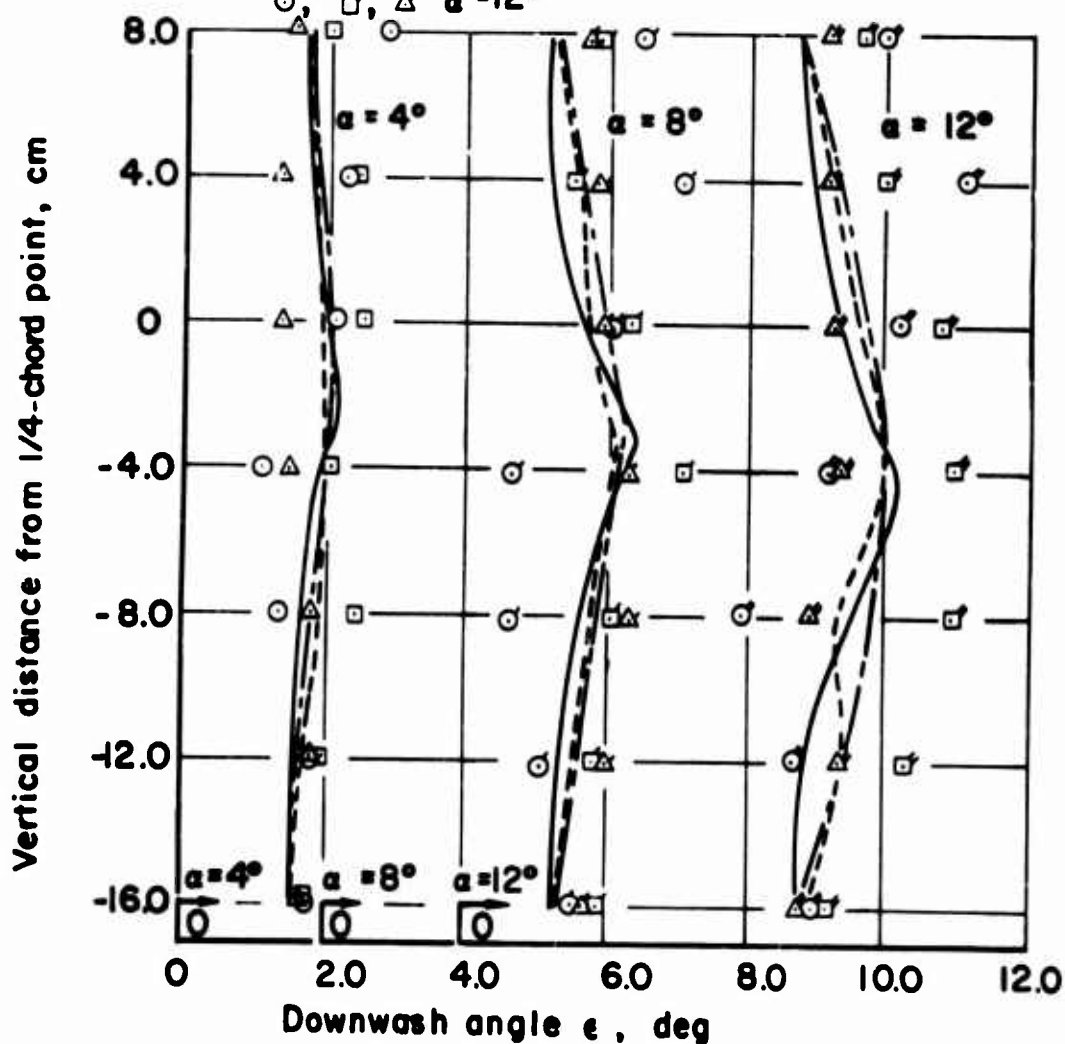


Figure 15. Comparison of Downwash Angle With Test Data, Single Untilted Propeller With Wing.

Tilted propeller, $T_c'' = 0.58$

$R_p = 10.34 \text{ cm}$, $R = 9.4 \text{ cm}$, $c = 20 \text{ cm}$

— Theory, ($\alpha_{\text{eff}} = \alpha + 6.5^\circ$)

○ Data from reference 4

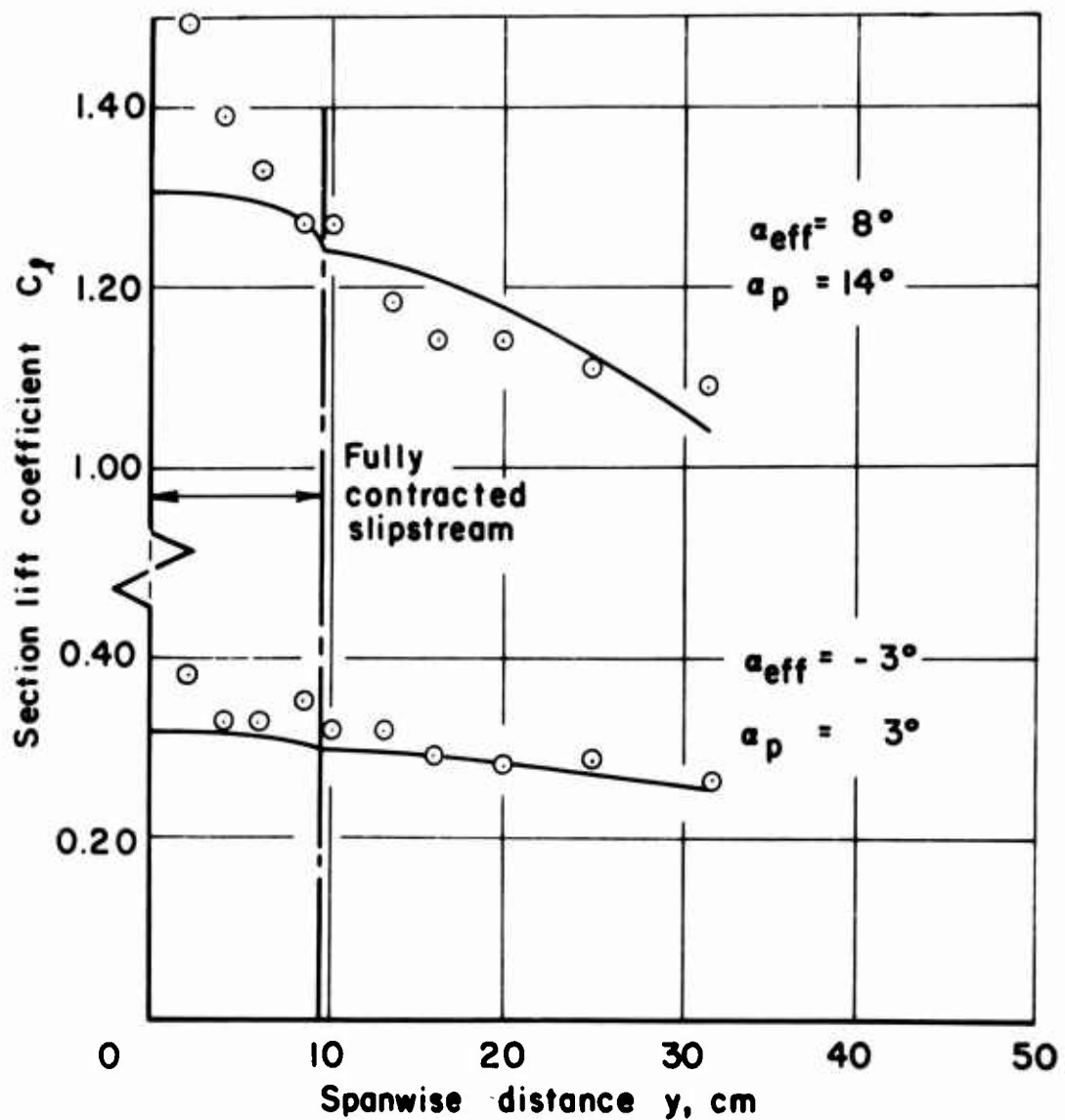


Figure 16. Comparison of Span Load Distribution With Test Data, Single Tilted Propeller With Wing.

Tilted propeller with rotation

$R_p = 1.63\text{ft}$, $c = 1.5\text{ft}$, $b = 9.54\text{ft}$, $J = 0.28$

Data from ref 4, figs.42 & 43

○ $\alpha = \alpha_p = 0^\circ$

□ $\alpha = \alpha_p = 10^\circ$

△ $\alpha = \alpha_p = 20^\circ$

Data for $\alpha_p > 20^\circ$ not shown because of stall effects

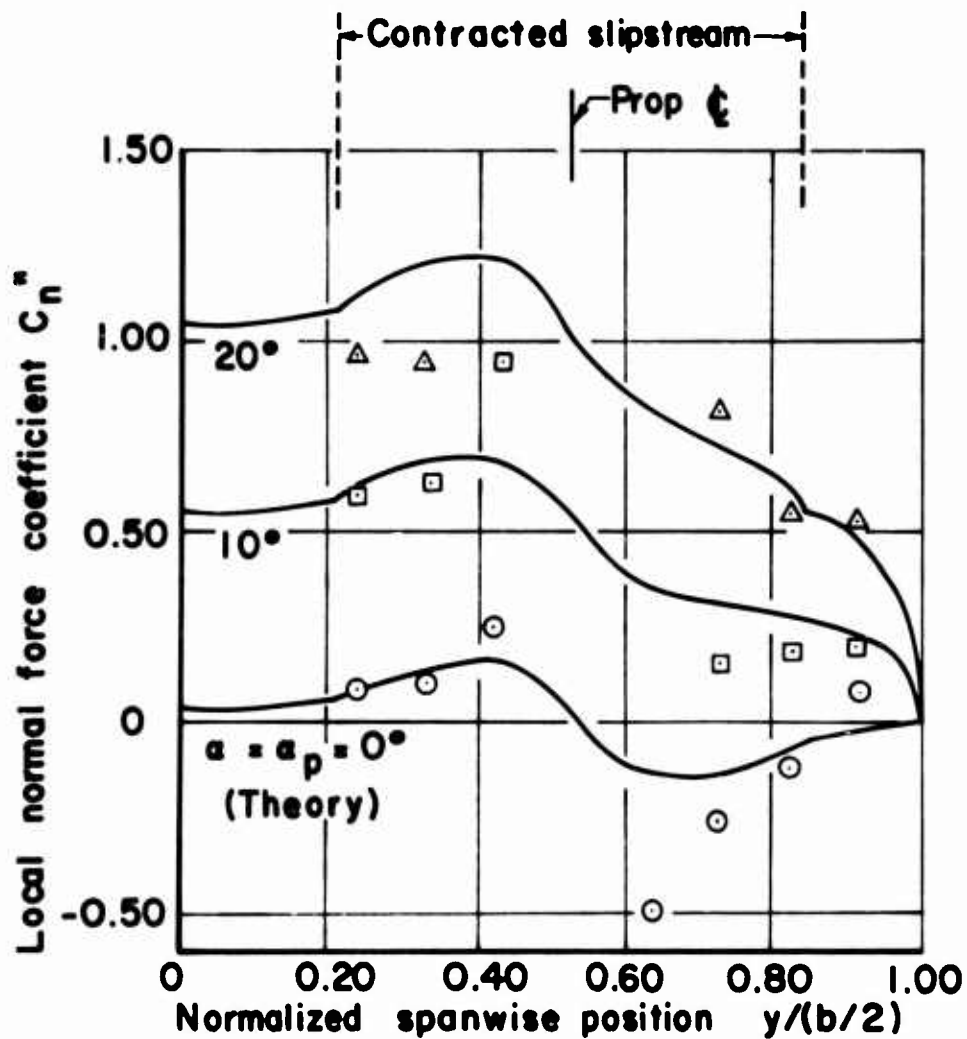


Figure 17. Comparison of Span Load Distribution With Test Data:
Two Tilted Propellers With Rotation, $T'_c = 0.50$.

Tilted propeller with rotation,
 $R_p = 1.63 \text{ ft}$, $c = 1.50 \text{ ft}$, $b = 9.54 \text{ ft}$, $J = 0.377$

Data from reference 13, figs. 24 & 25

○	$\alpha =$	$\alpha_p = 0^\circ$
□	"	" $= 10^\circ$
◇	"	" $= 15^\circ$
△	"	

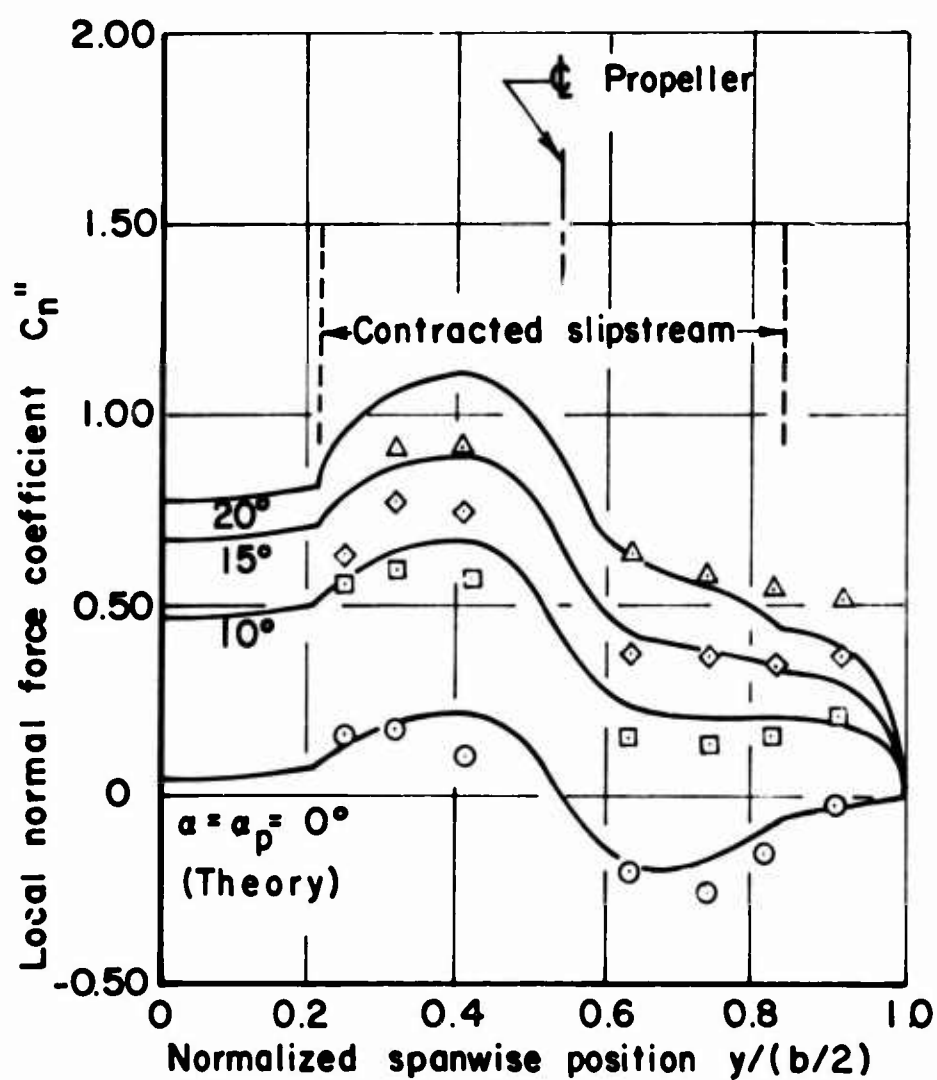


Figure 18. Comparison of Span Load Distribution With Test Data:
 Two Tilted Propellers With Rotation, $\Gamma_c'' = 0.60$.

Data from reference 18, figs. 19 & 20.

Measured downwash angle is tail incidence with respect to free stream direction for zero tail moment coefficient.

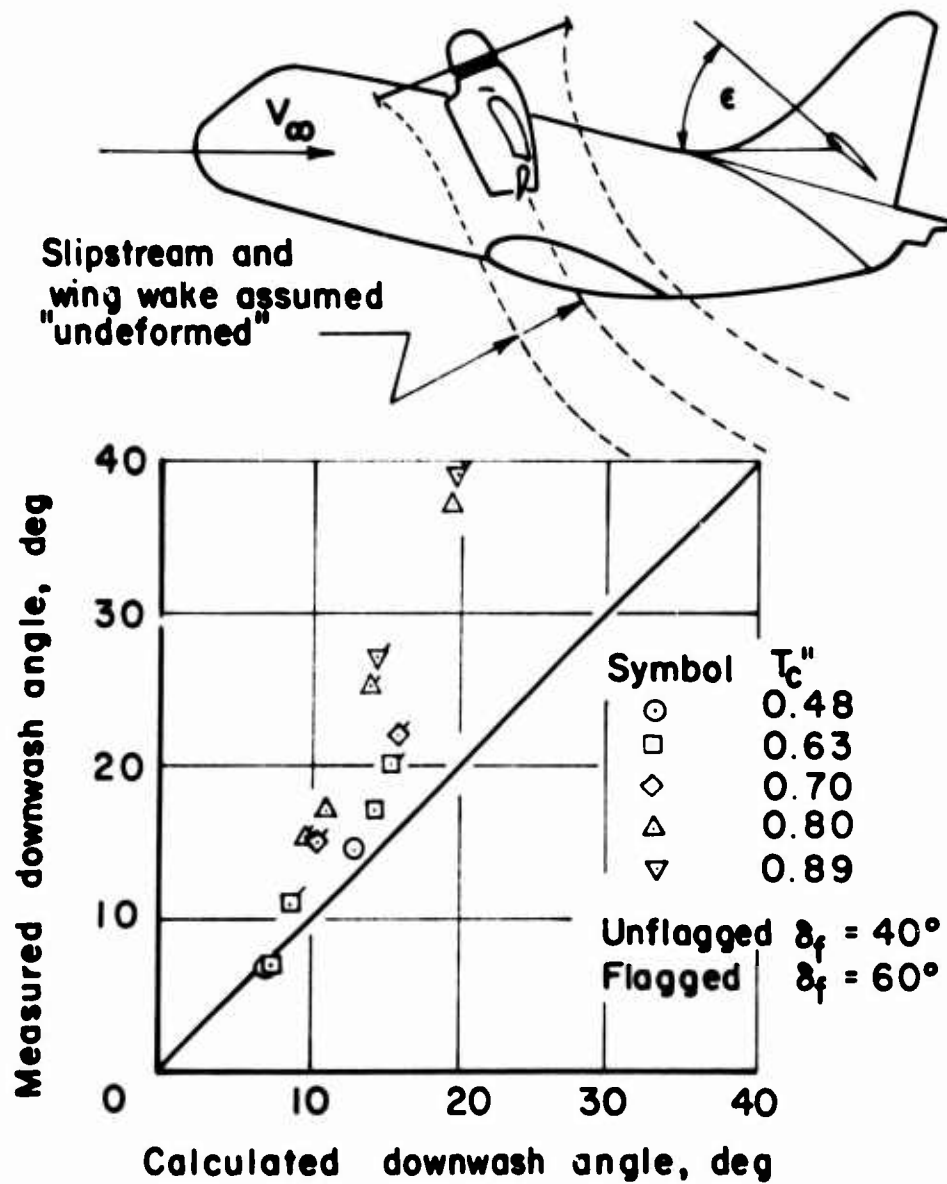


Figure 19. Comparison of Downwash Angle With Test Data: Four Tilted Propellers With Rotation, Full Vertical Wake Displacement.

Experimental downwash data are the same as in fig.19.
 Calculated downwash data obtained with 1/2
 calculated wake displacement.

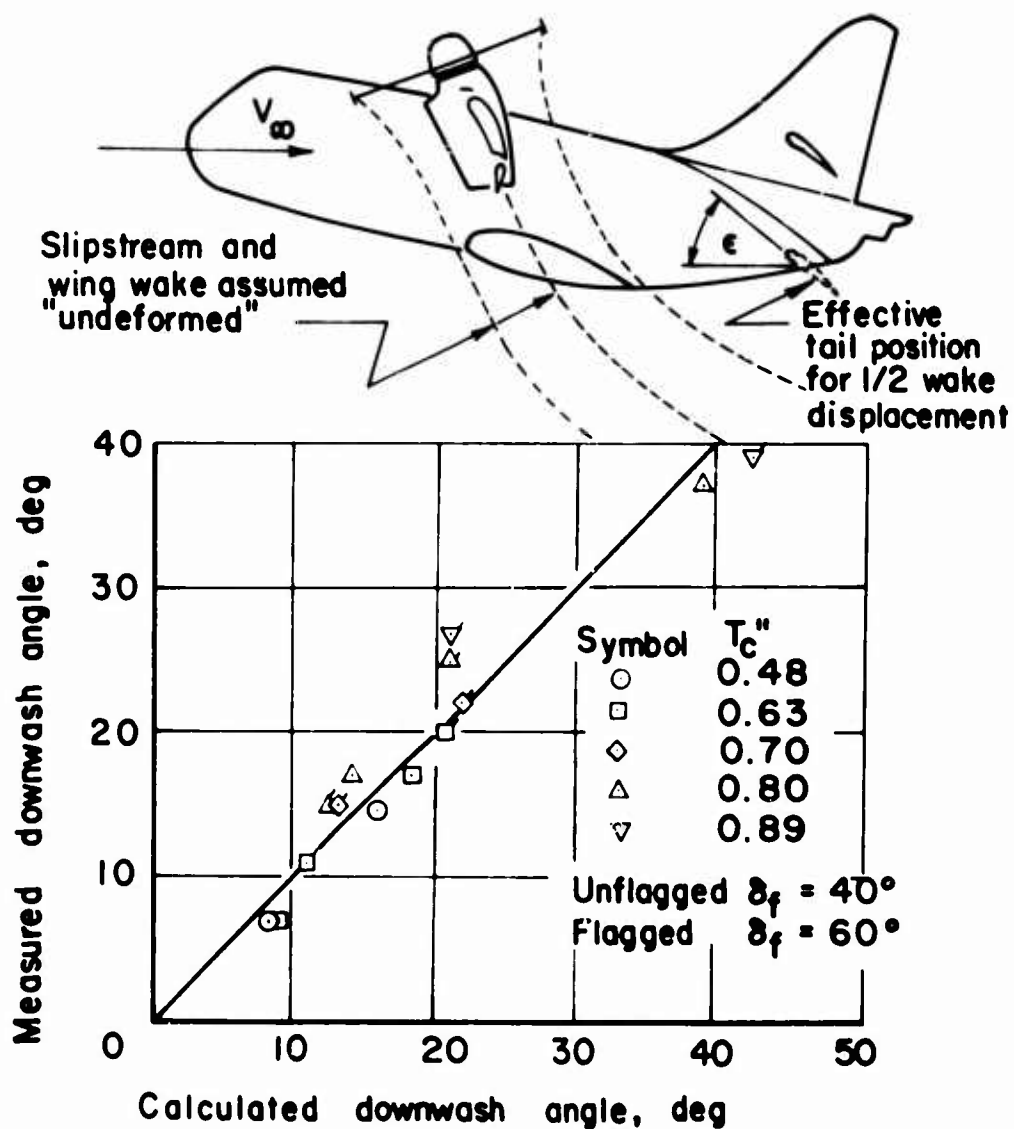


Figure 20. Comparison of Downwash Angle With Test Data:
 Four Tilted Propellers With Rotation, 1/2
 Vertical Wake Displacement.

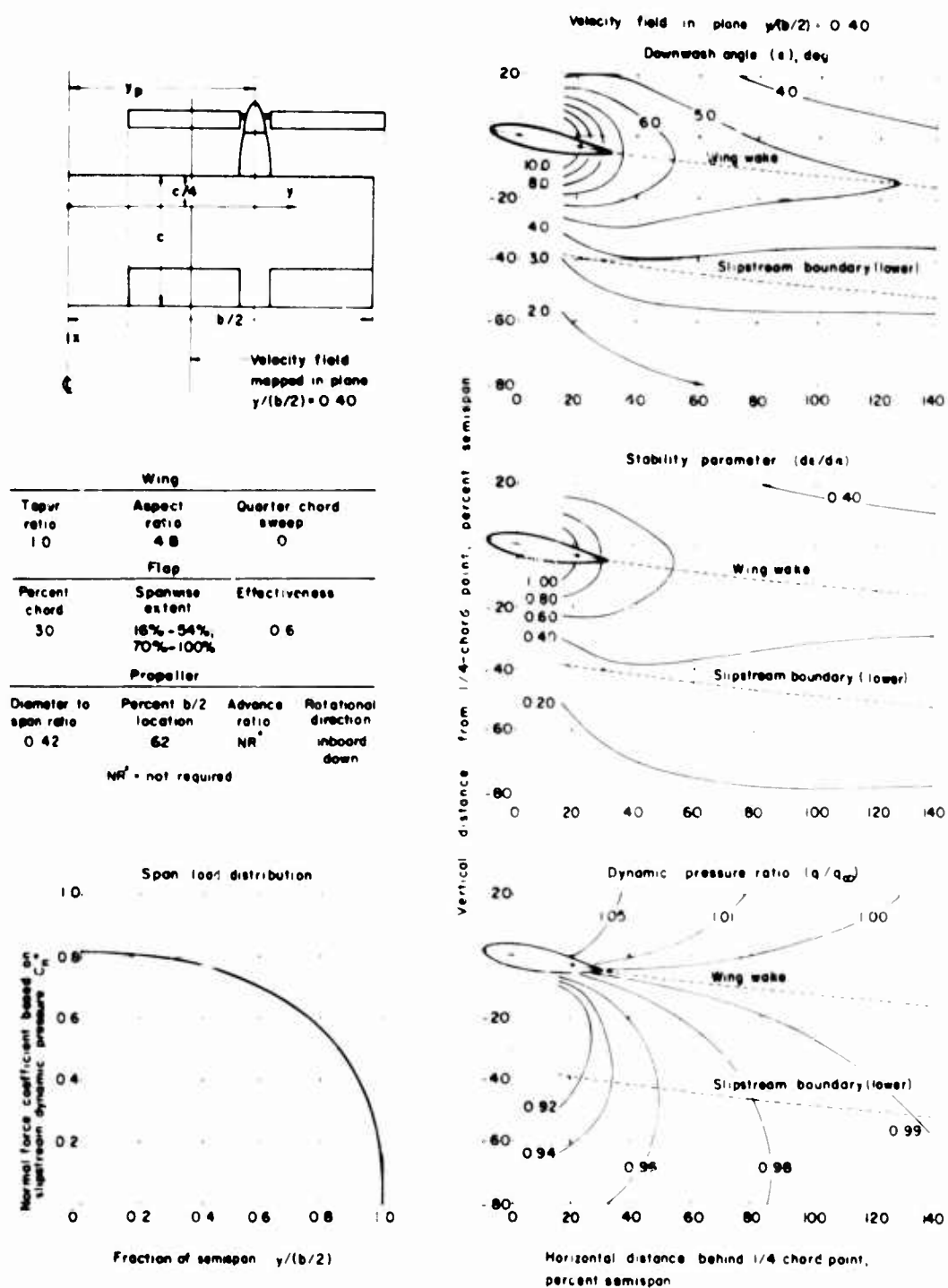


Figure 21. Two-Slipstream Configuration Design Charts:
 $T_c'' = 0$, $\alpha = 10^\circ$, $\delta_f = 0^\circ$.

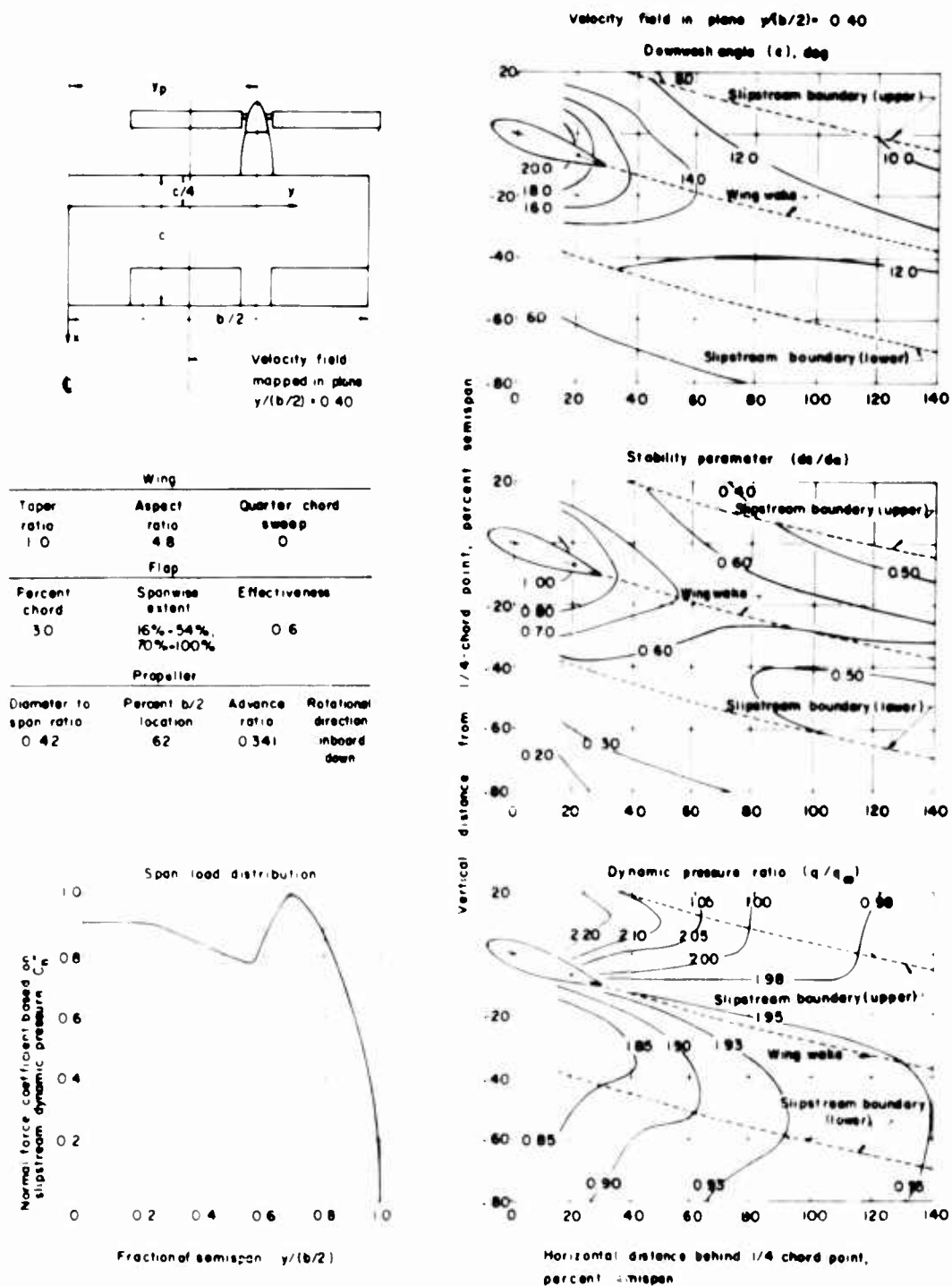


Figure 22. Two-Slipstream Configuration Design Charts:
 $T_c'' = 0.5$, $\alpha = 20^\circ$, $\alpha_p = 20^\circ$, $\delta_f = 0^\circ$, $J = 0.34$.

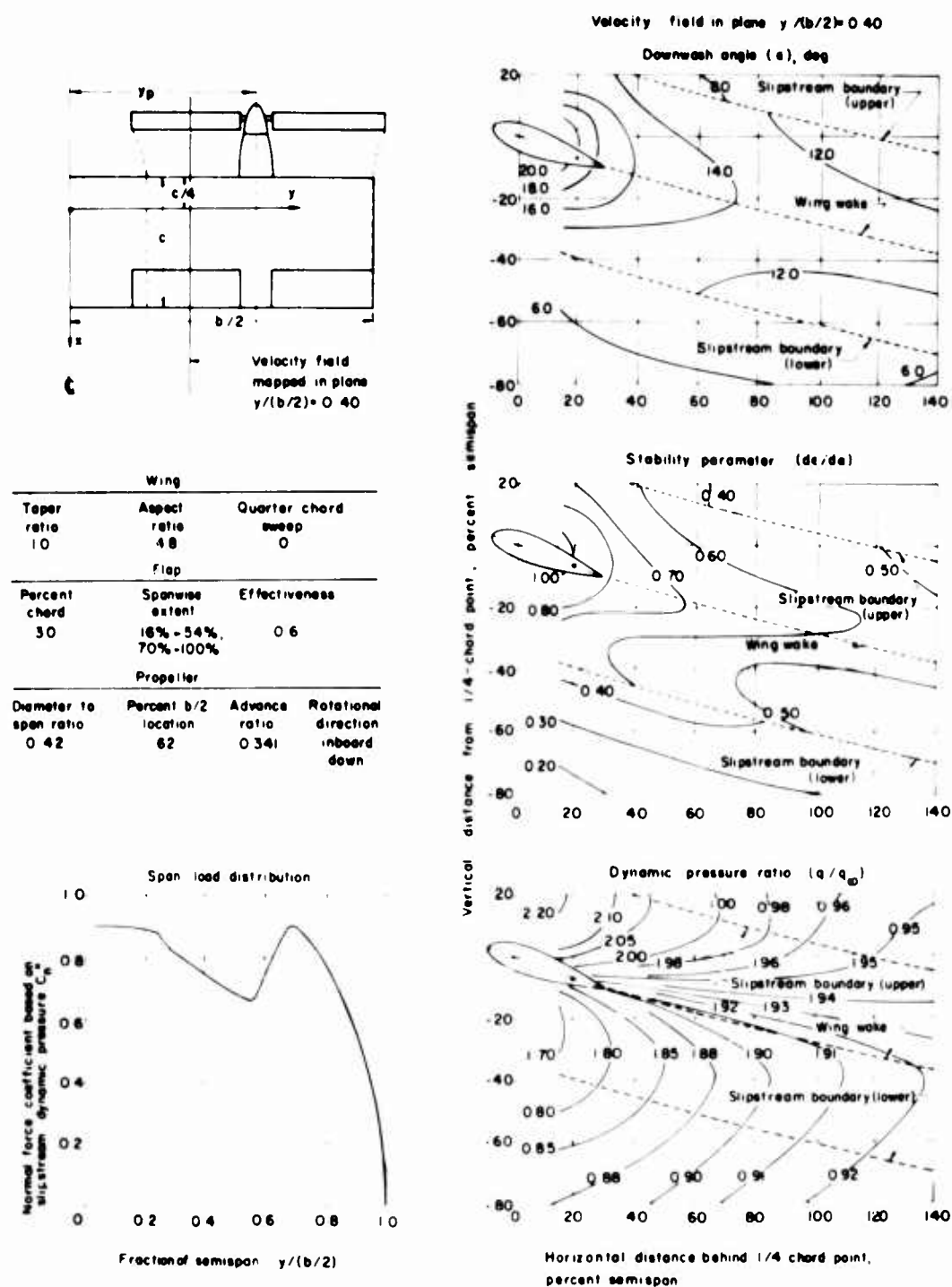


Figure 23. Two-Slipstream Configuration Design Charts:
 $T'_c = 0.5$, $\alpha = 20^\circ$, $\alpha_p = 30^\circ$, $\delta_f = 0^\circ$, $J = 0.34$.

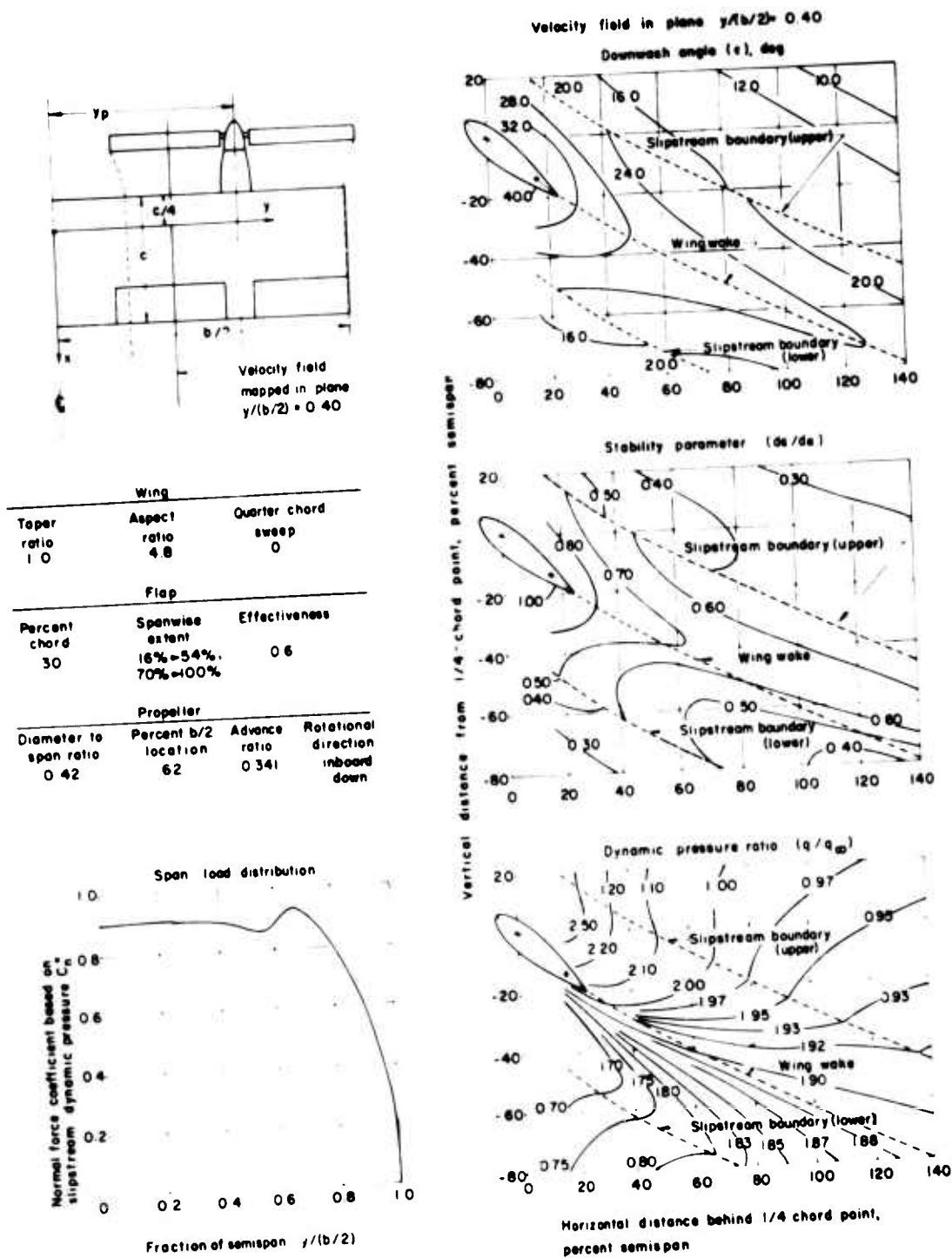


Figure 24. Two-Slipstream Configuration Design Charts:
 $T_c'' = 0.5$, $\alpha = 40^\circ$, $\alpha_p = 40^\circ$, $\delta_f = 0^\circ$, $J = 0.34$.

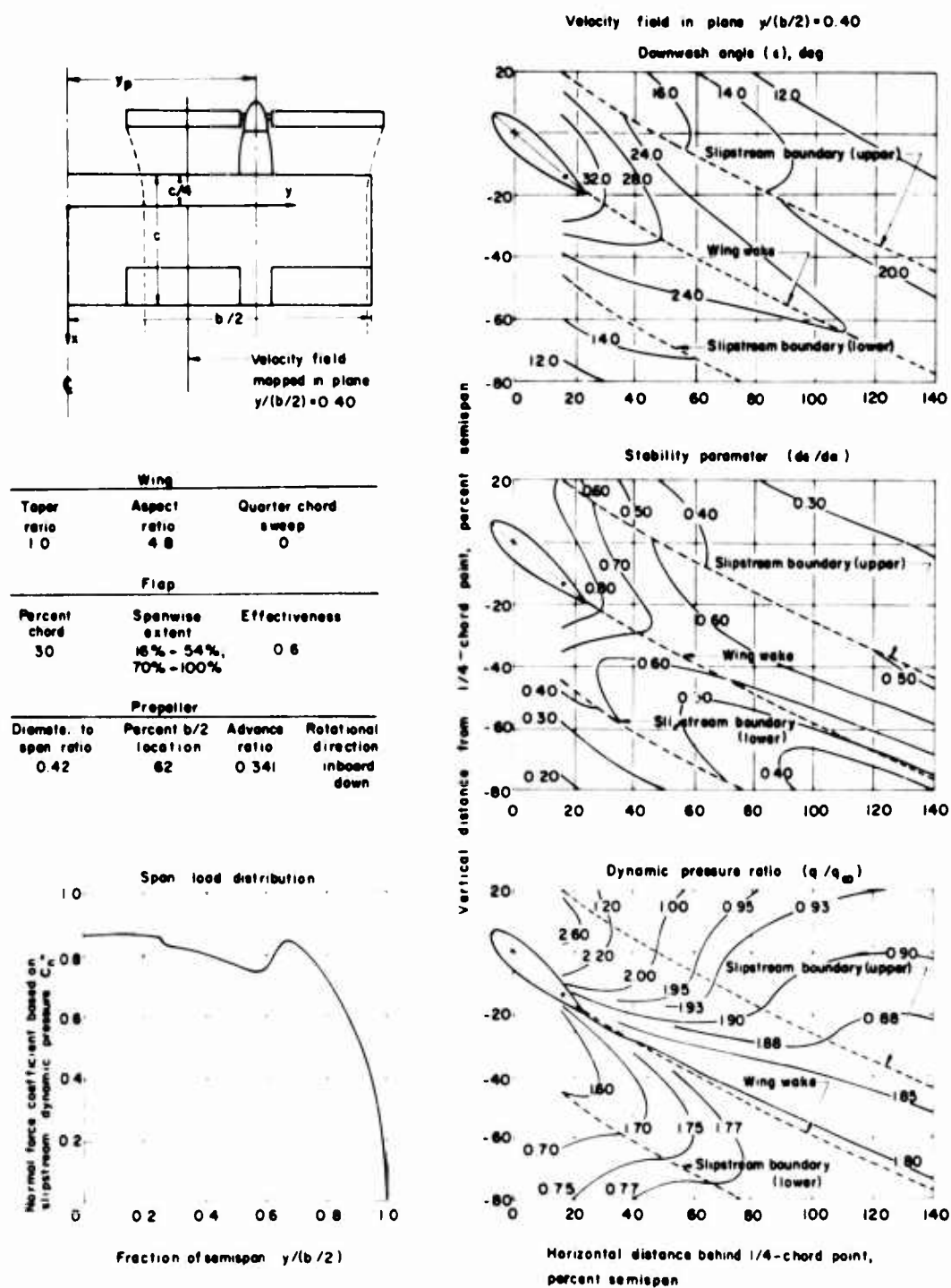


Figure 25. Two-Slipstream Configuration Design Charts:
 $T_c'' = 0.5$, $\alpha = 40^\circ$, $\alpha_p = 30^\circ$, $\delta_f = 0^\circ$, $J = 0.34$.

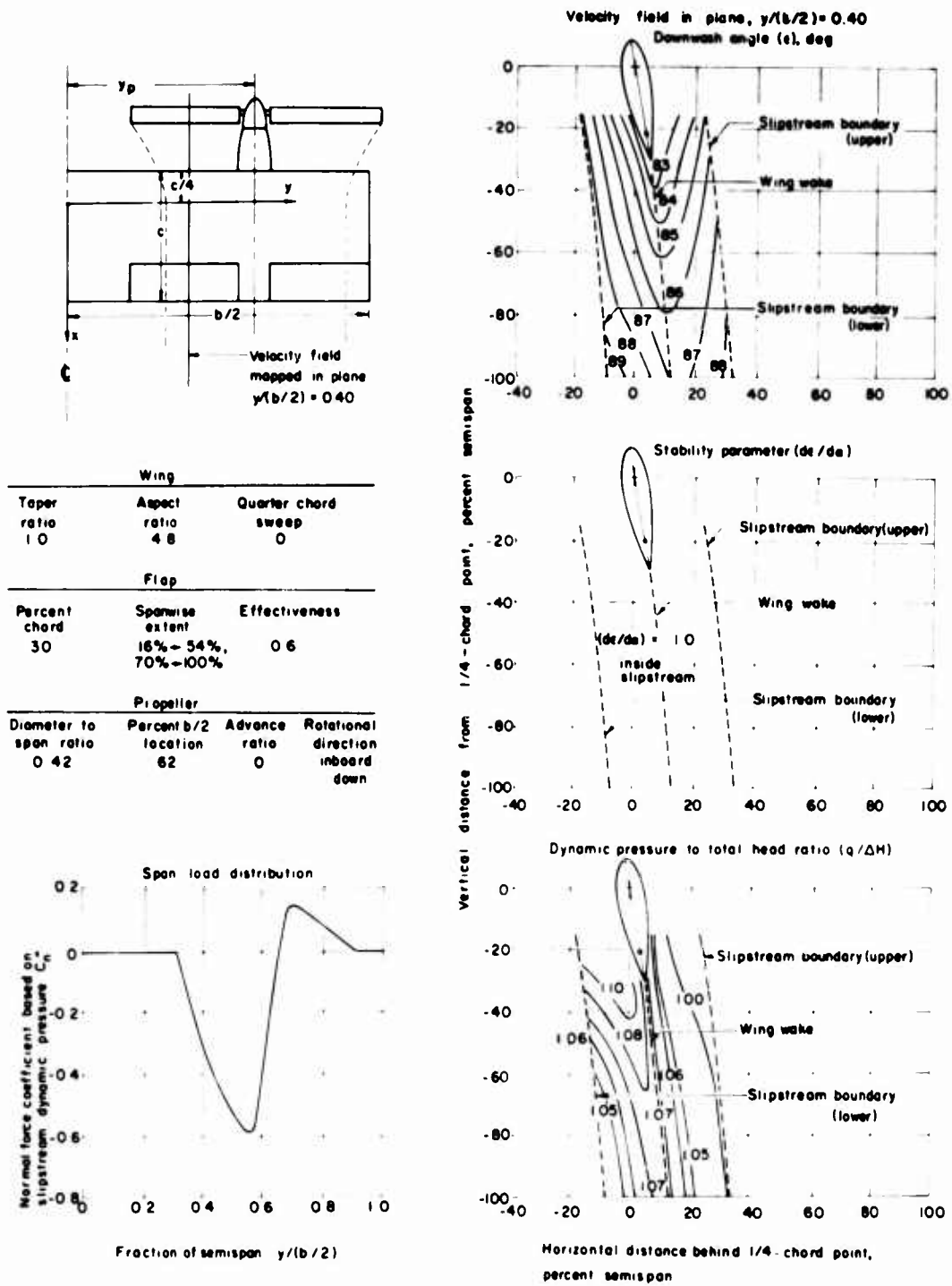


Figure 26. Two-Slipstream Configuration Design Charts:
 $T_c'' = 1.0$, $\alpha = 80^\circ$, $\alpha_p = 90^\circ$, $\delta_f = 0^\circ$, $J = 0$.

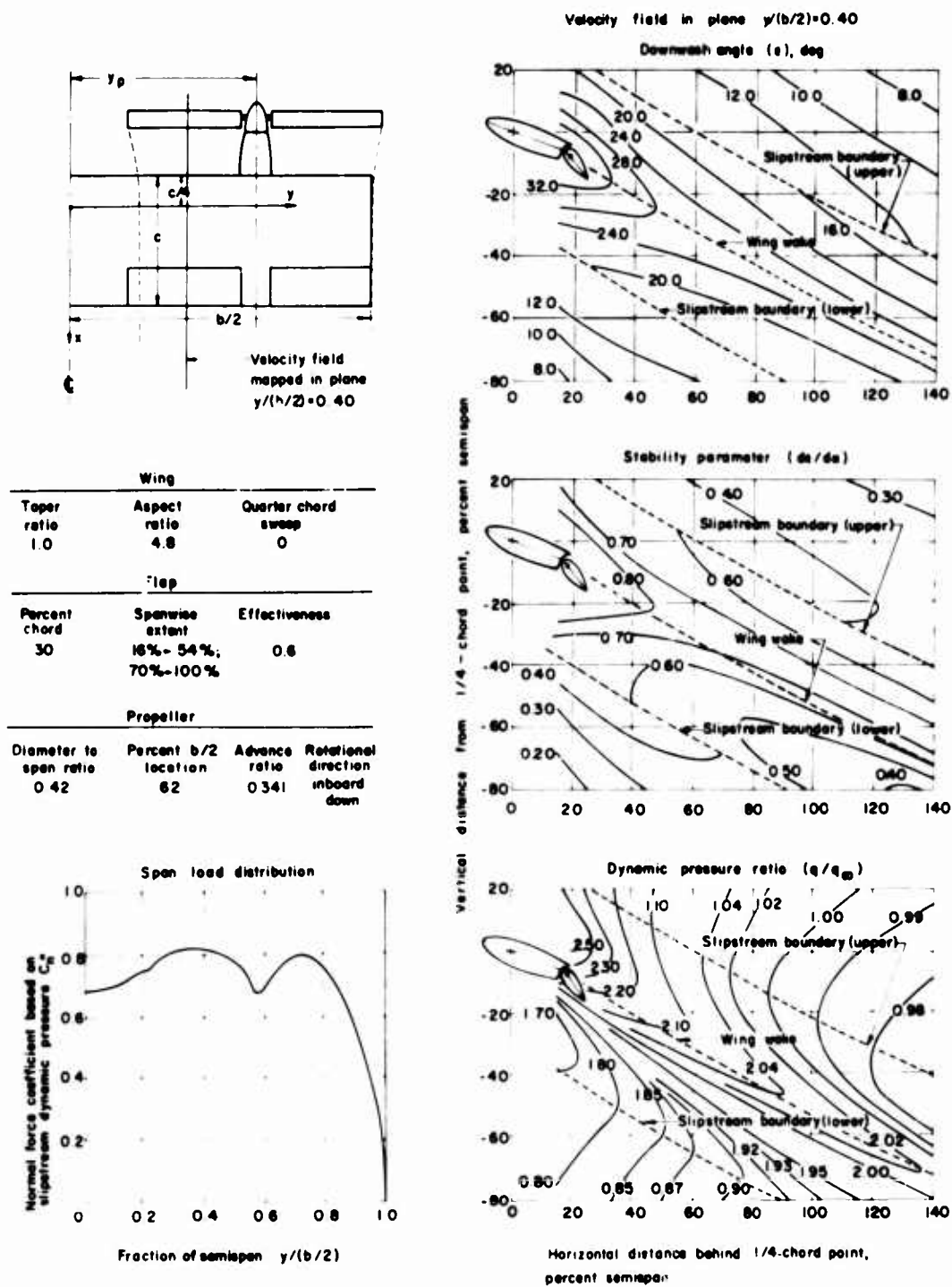


Figure 28. Two-Slipstream Configuration Design Charts:
 $T_c'' = 0.5$, $\alpha = 20^\circ$, $\alpha_p = 20^\circ$, $\delta_f = 30^\circ$, $J = 0.34$.

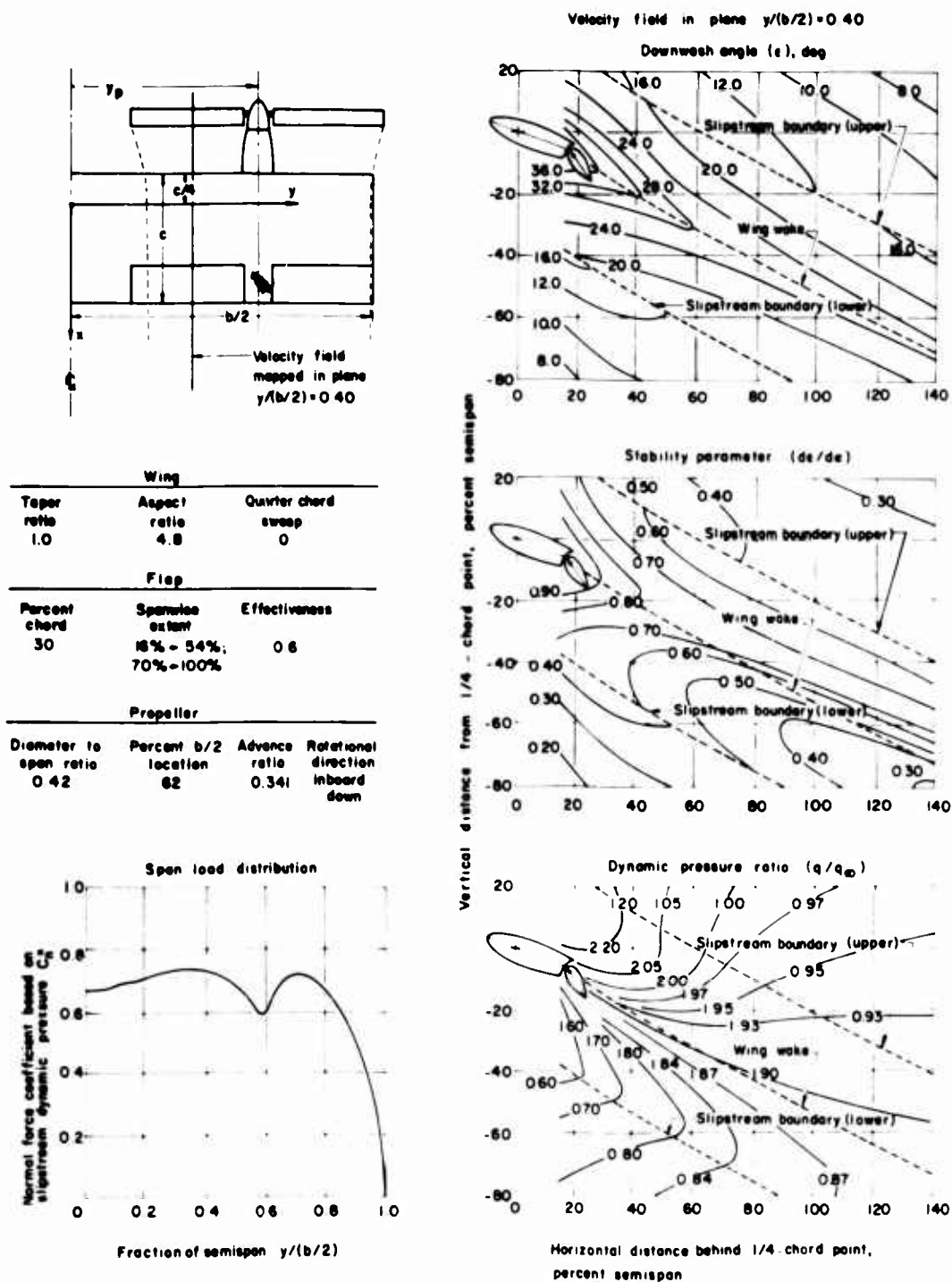


Figure 29. Two-Slipstream Configuration Design Charts:
 $T_c'' = 0.5$, $\alpha = 20^\circ$, $\alpha_p = 30^\circ$, $\delta_f = 30^\circ$, $J = 0.34$.

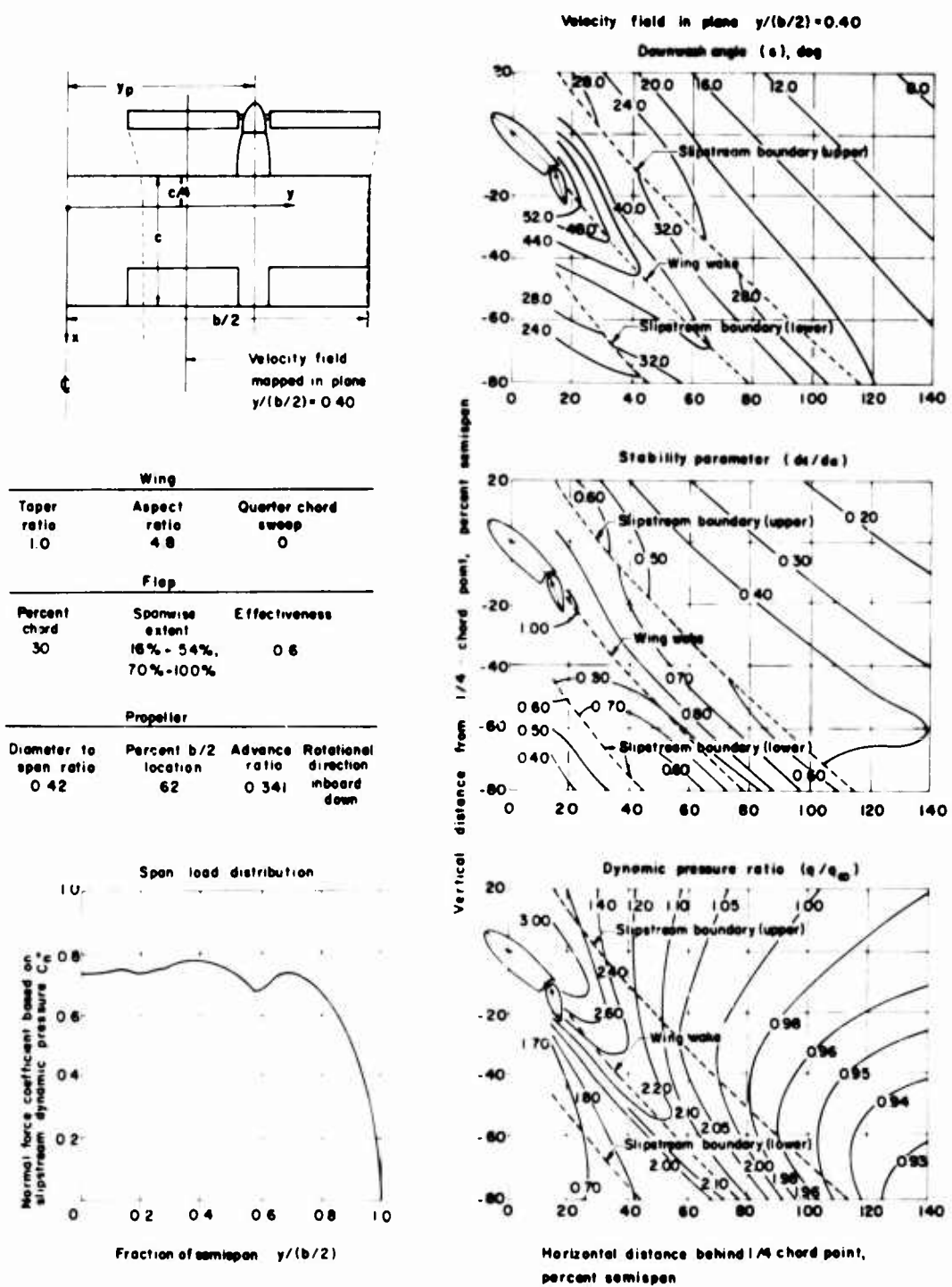


Figure 30. Two-Slipstream Configuration Design Charts:
 $T_c'' = 0.5$, $\alpha = 40^\circ$, $\alpha_p = 40^\circ$, $\delta_f = 30^\circ$, $J = 0.34$.

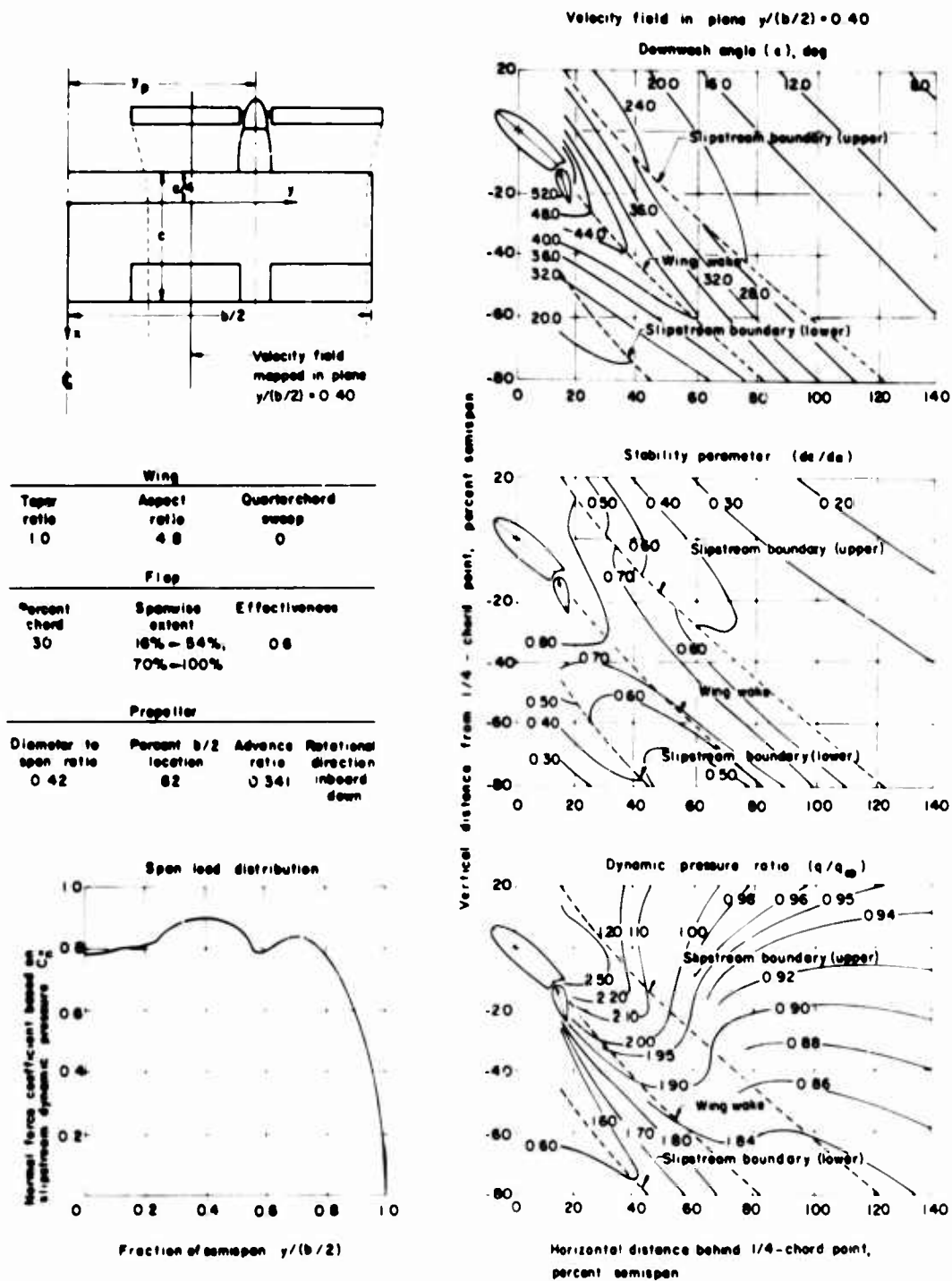


Figure 31. Two-Slipstream Configuration Charts;
 $T_c'' = 0.5$, $\alpha = 40^\circ$, $\alpha_p = 30^\circ$, $\delta_f = 30^\circ$, $J = 0.34$.

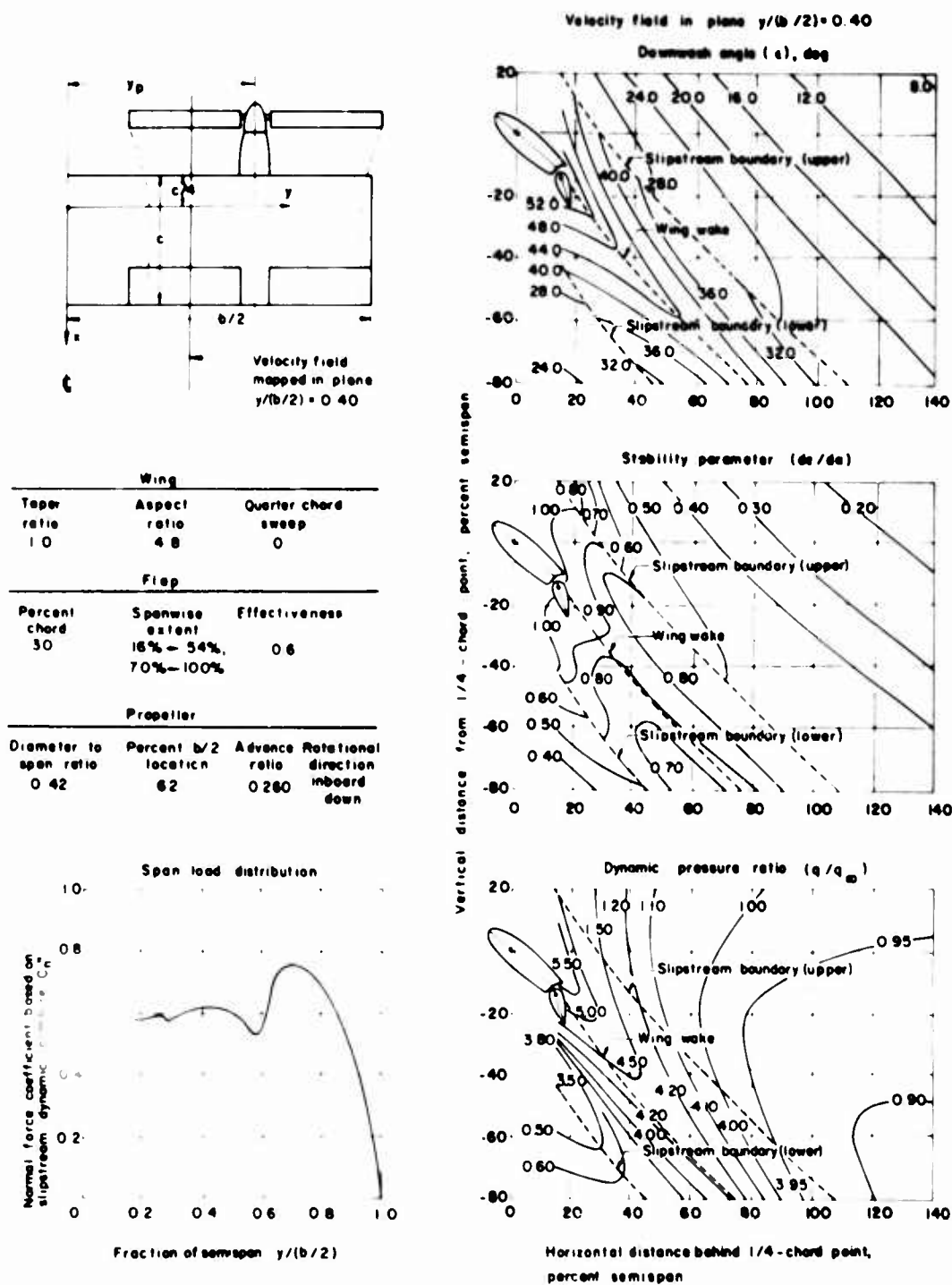


Figure 32. Two-Slipstream Configuration Charts:
 $T'_c = 0.75$, $\alpha = 40^\circ$, $\alpha_p = 40^\circ$, $\delta_f = 30^\circ$, $J = 0.26$.

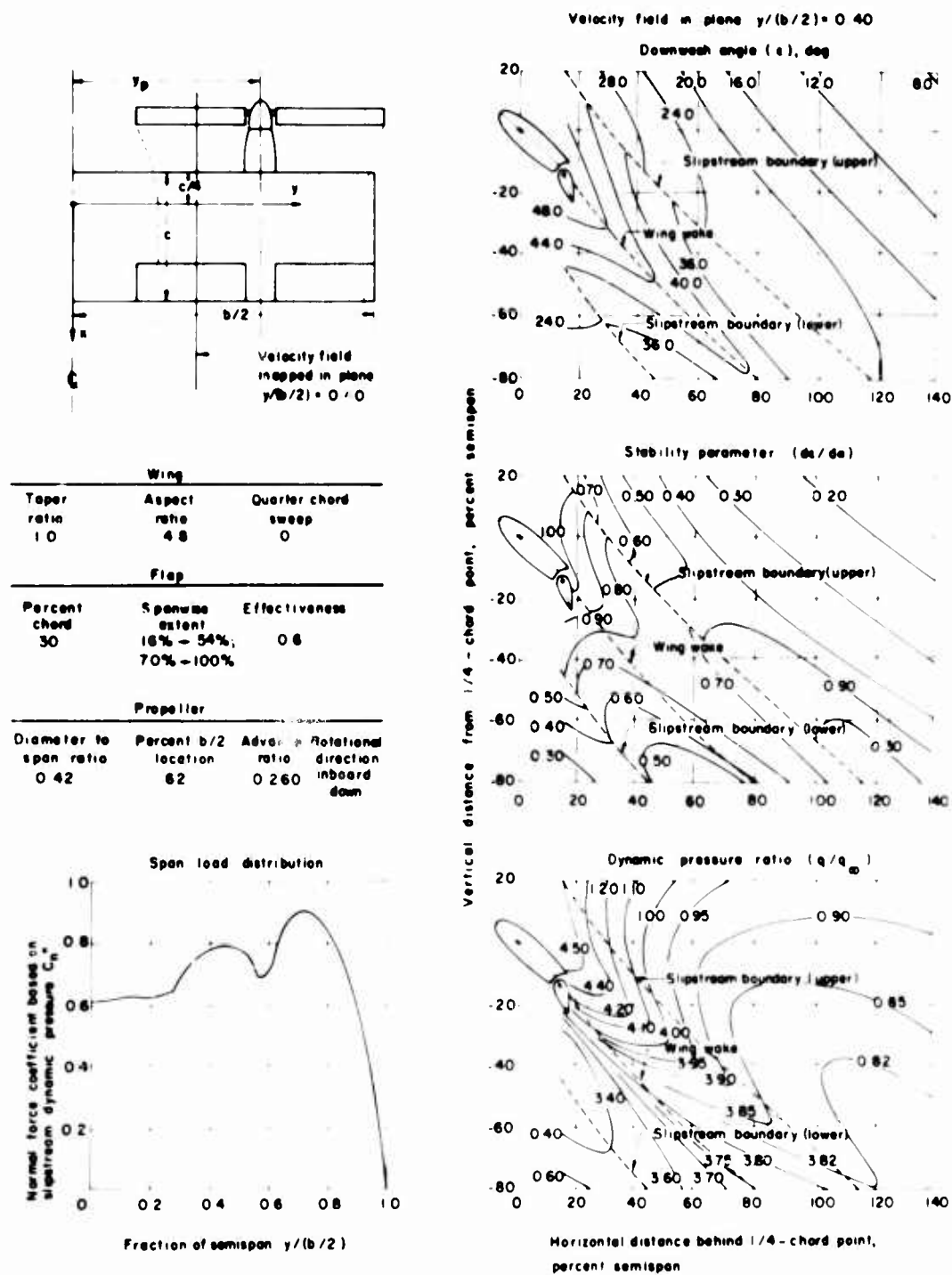


Figure 33. Two-Slipstream Configuration Charts:
 $T'_c = 0.75$, $\alpha = 40^\circ$, $\alpha_p = 30^\circ$, $\delta_f = 30^\circ$, $J = 0.26$.

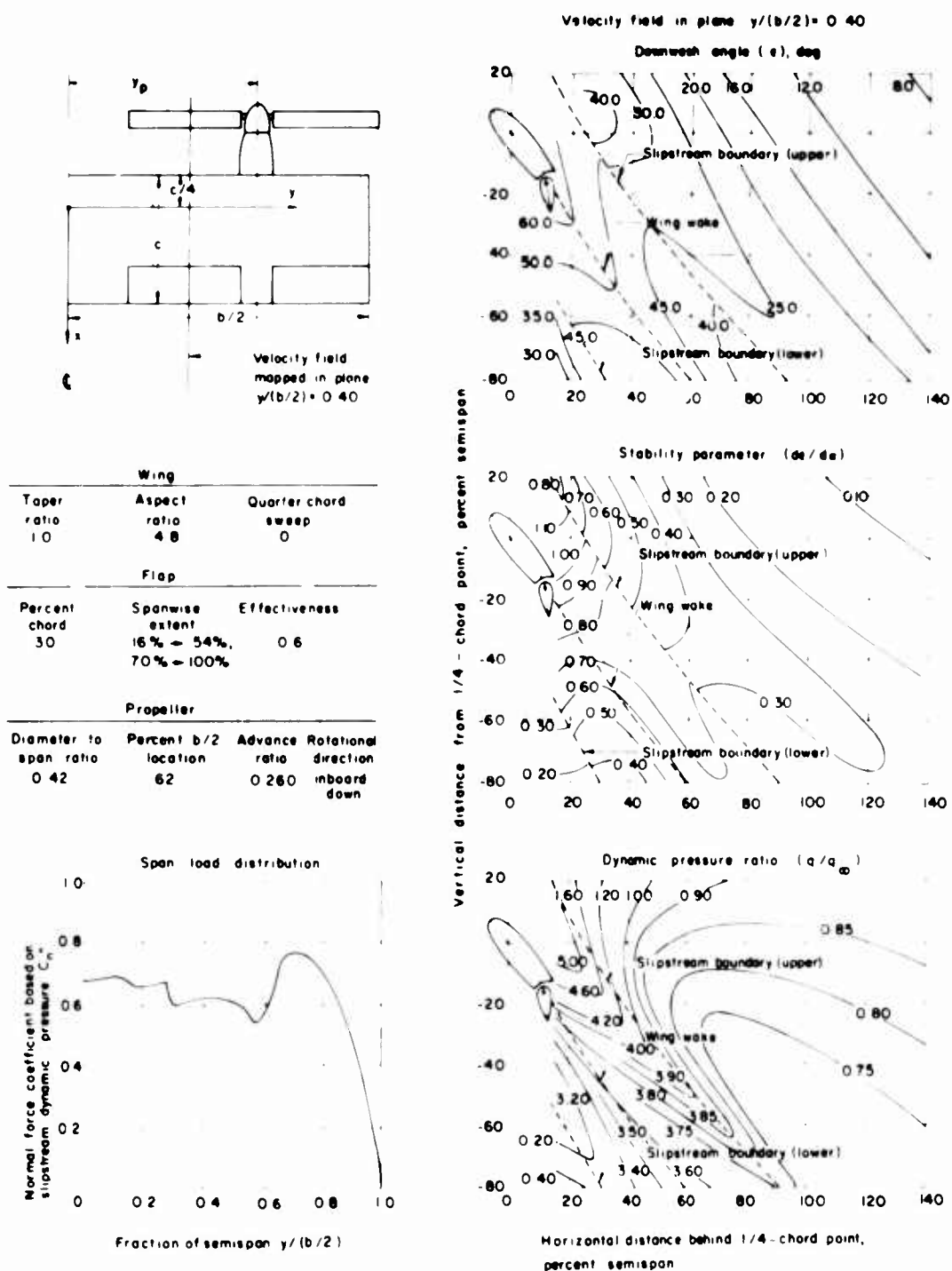


Figure 34. Two-Slipstream Configuration Charts:

$$T_c'' = 0.75, \alpha = 50^\circ, \alpha_p = 50^\circ, \delta_f = 30^\circ, J = 0.26.$$

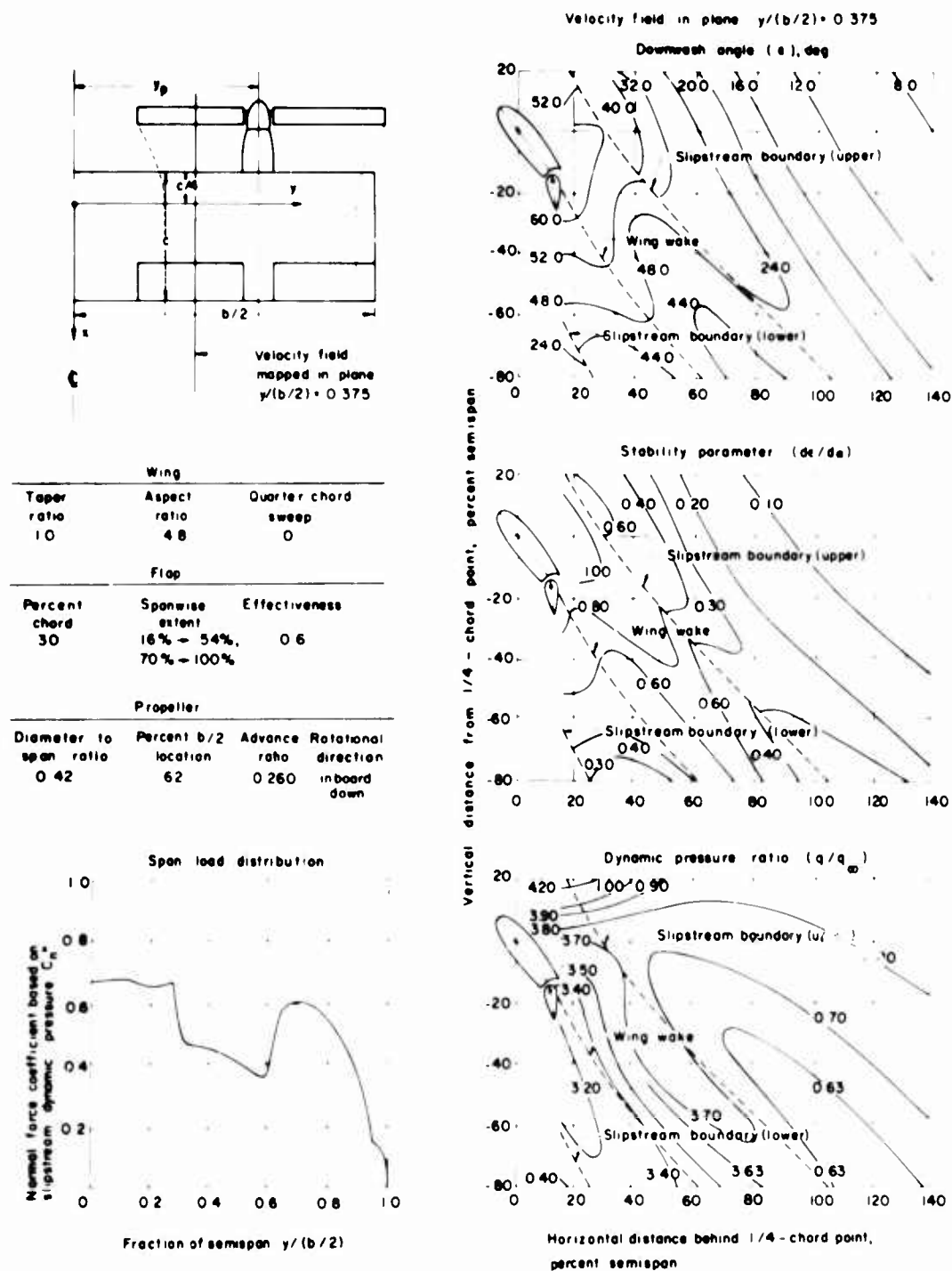


Figure 35. Two-Slipstream Configuration Charts:
 $T_c'' = 0.75$, $\alpha = 50^\circ$, $\alpha_p = 60^\circ$, $\delta_f = 30^\circ$, $J = 0.26$.

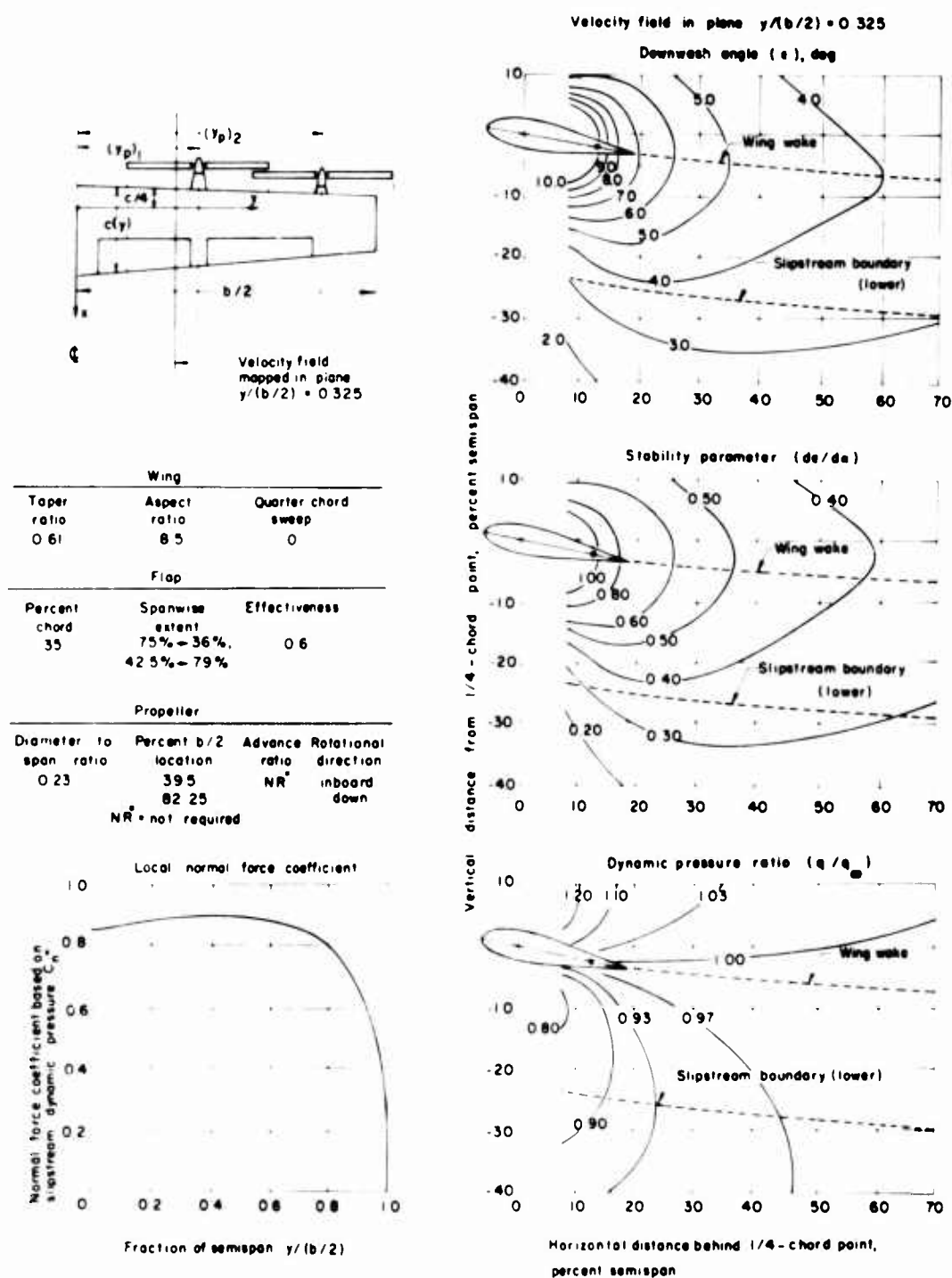


Figure 36. Four-Slipstream Configuration Design Charts:
 $T_c'' = 0$, $\alpha = 10^\circ$, $\delta_f = 0^\circ$.

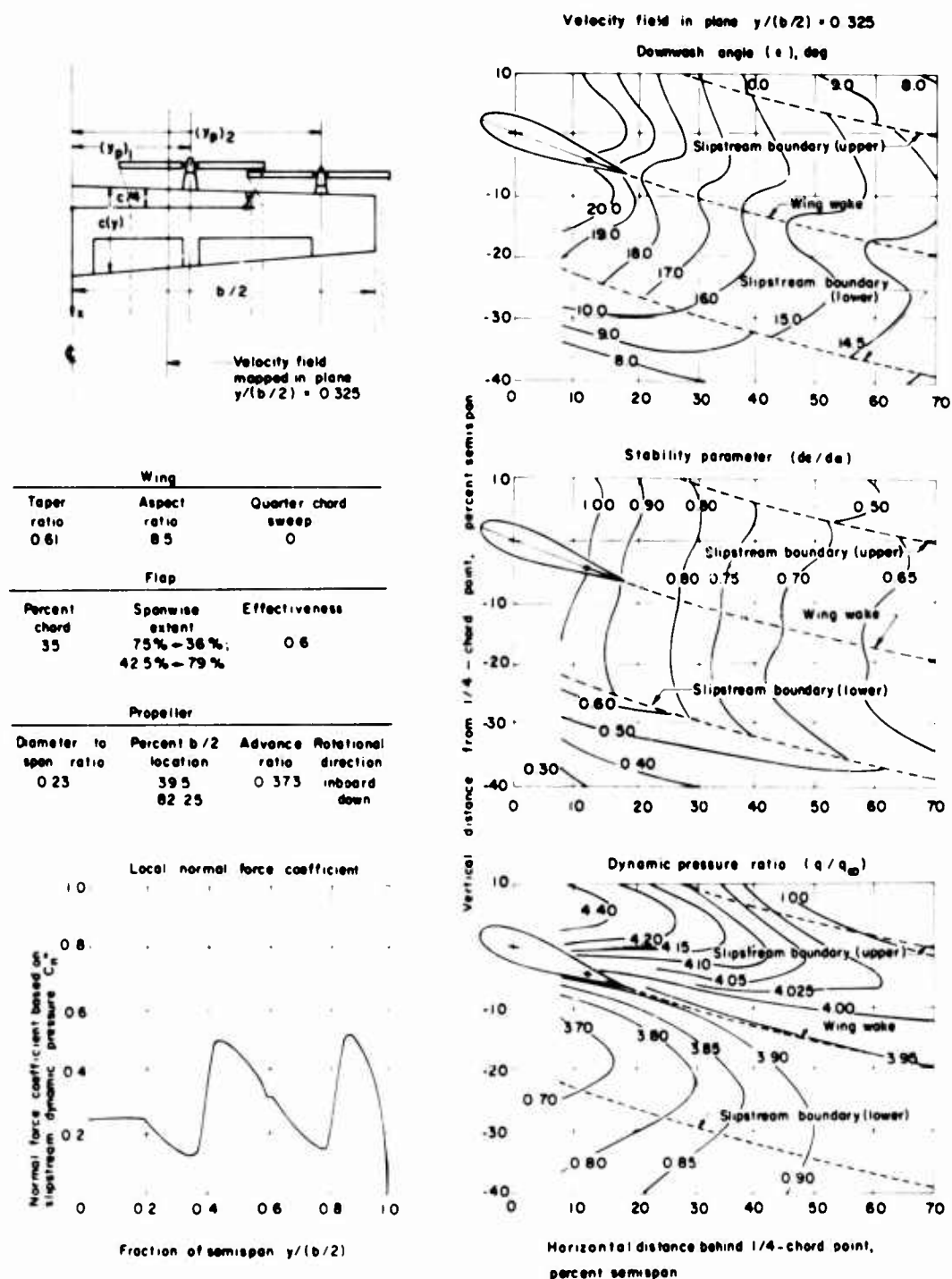


Figure 37. Four-Slipstream Configuration Design Charts:
 $T'_c = 0.75$, $\alpha = 20^\circ$, $\alpha_p = 20^\circ$, $\delta_f = 0^\circ$, $J = 0.37$.

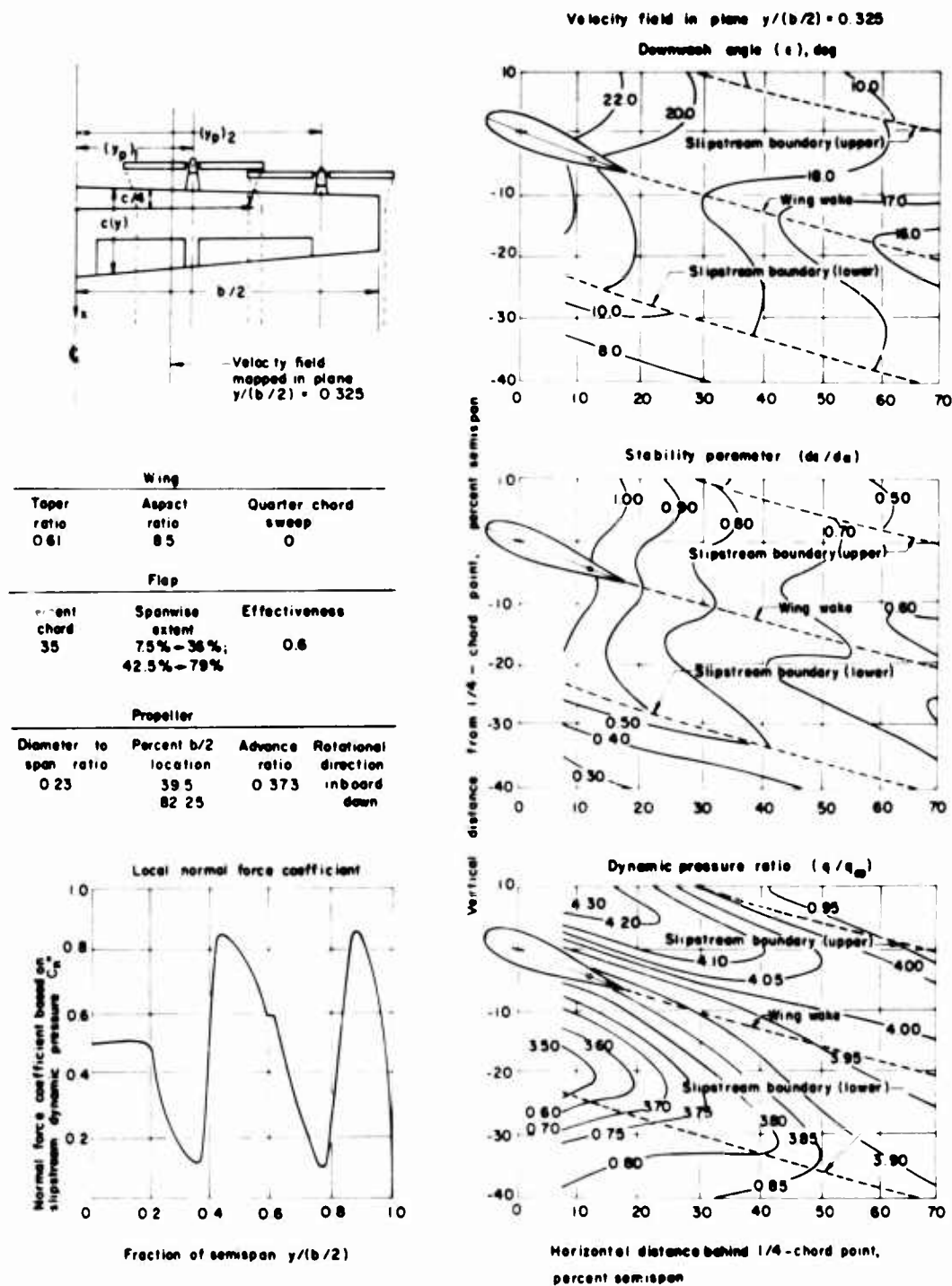


Figure 38. Four-Slipstream Configuration Design Charts:
 $T_c'' = 0.75$, $\alpha = 20^\circ$, $\alpha_p = 30^\circ$, $\delta_f = 0^\circ$, $J = 0.37$.

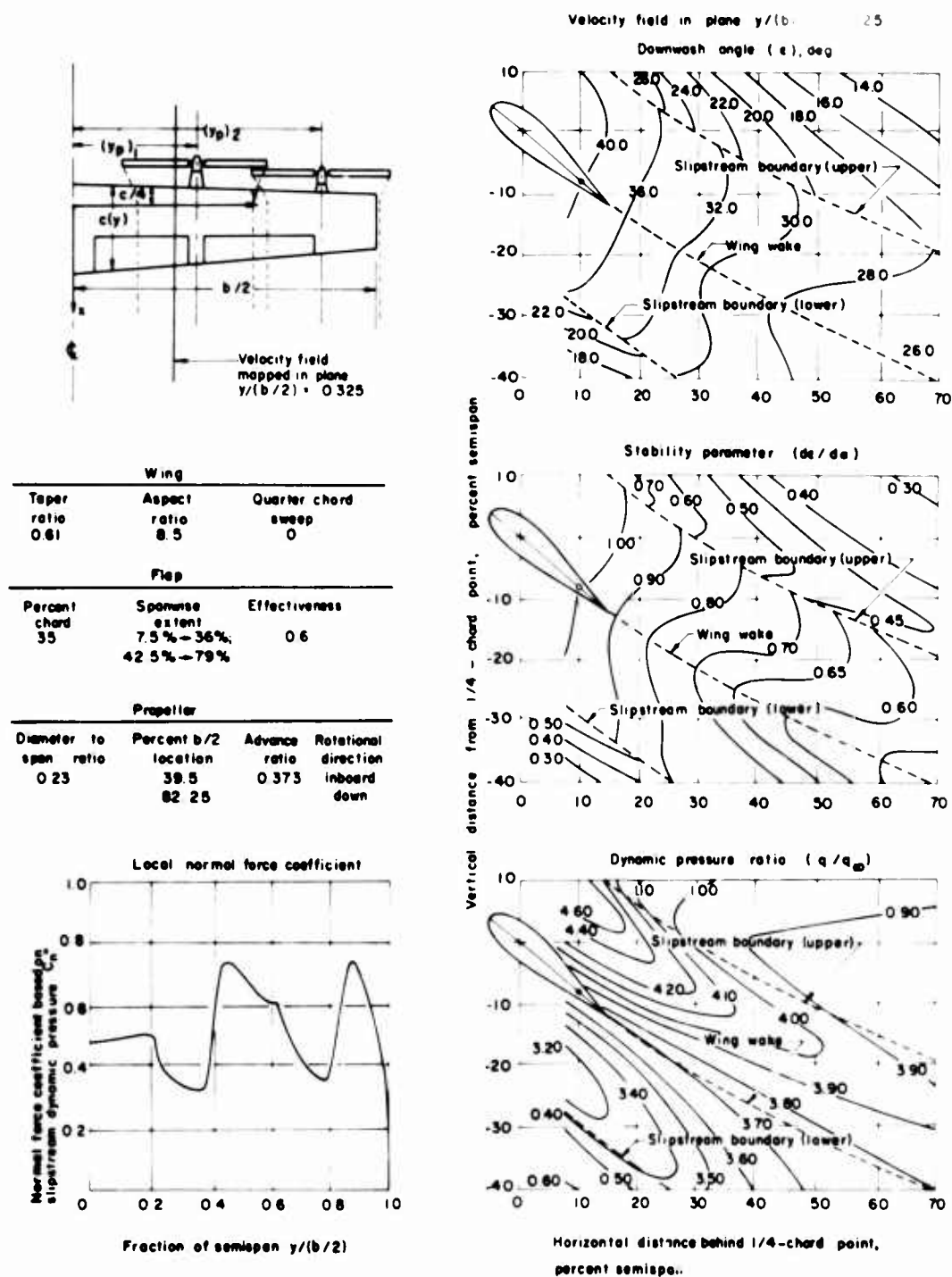


Figure 39. Four-Slipstream Configuration Design Charts:
 $T'_c = 0.75$, $\alpha = 40^\circ$, $\alpha_p = 40^\circ$, $\delta_f = 0^\circ$, $J = 0.37$.

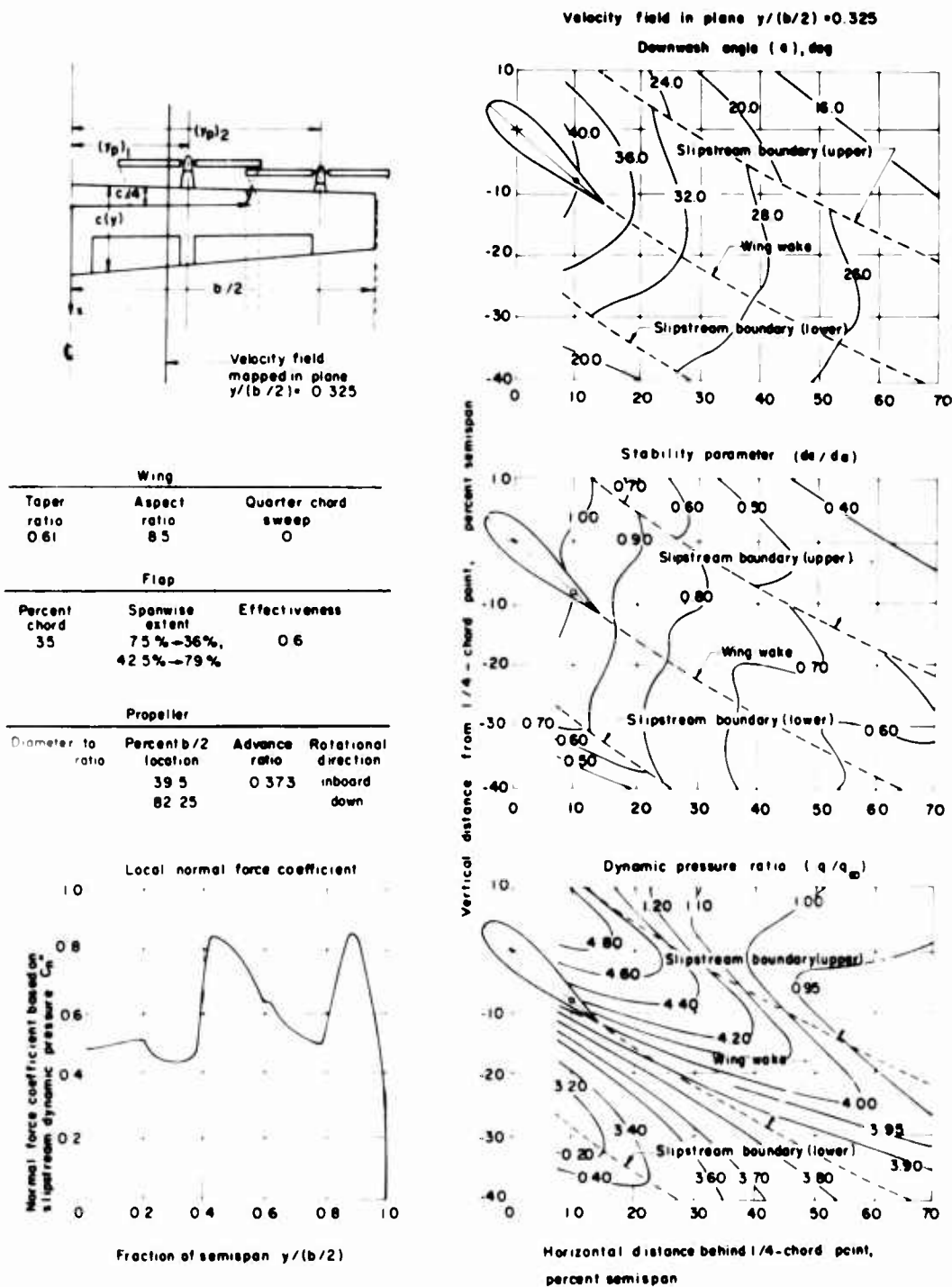


Figure 40. Four-Slipstream Configuration Design Charts:
 $T_c'' = 0.75$, $\alpha = 40^\circ$, $\alpha_p = 30^\circ$, $\delta_f = 0^\circ$, $J = 0.37$.

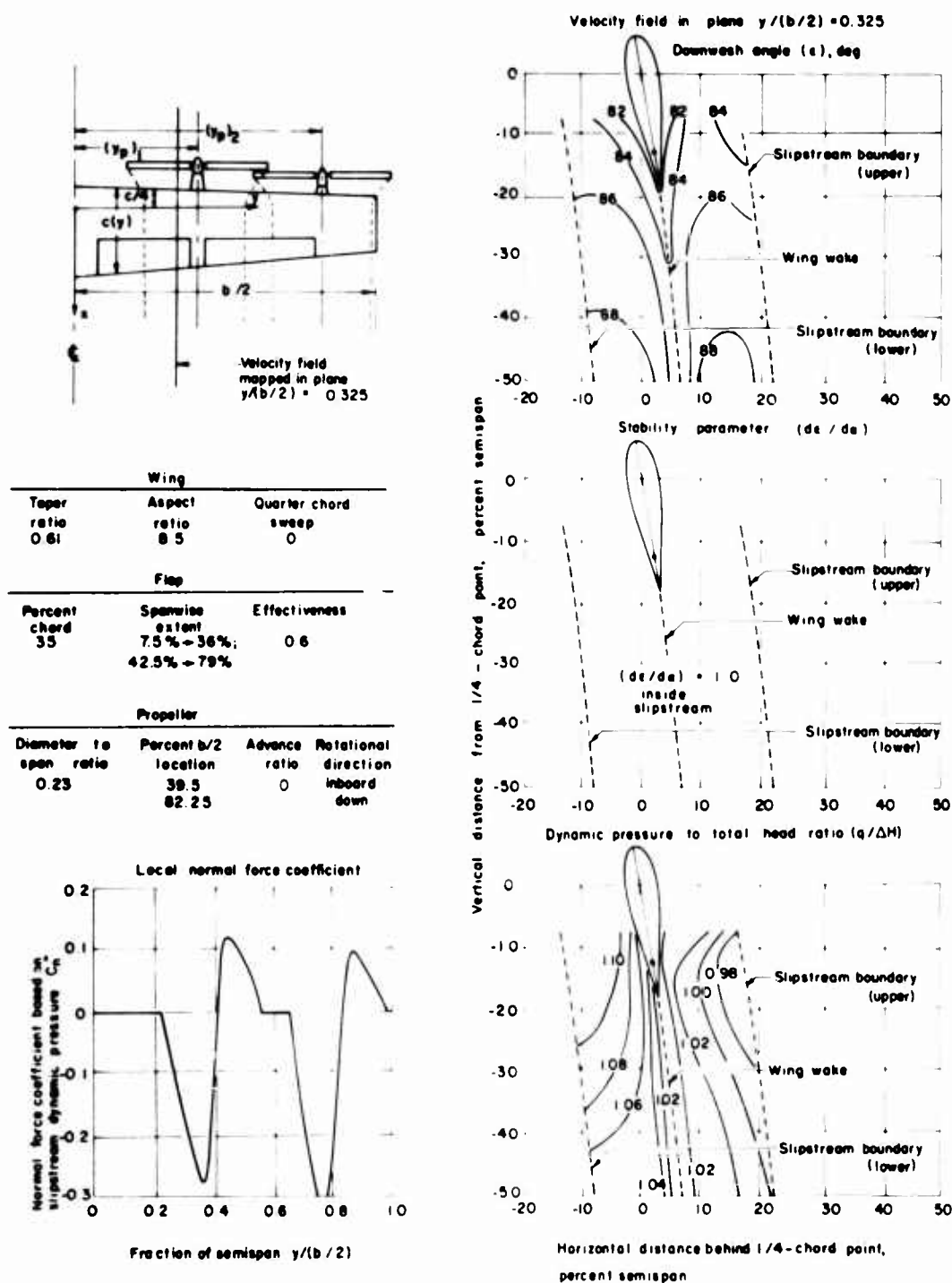


Figure 41. Four-Slipstream Configuration Design Charts:
 $T'_c = 1.0$, $\alpha = 80^\circ$, $\alpha_p = 90^\circ$, $\delta_f = 0^\circ$, $J = 0$.

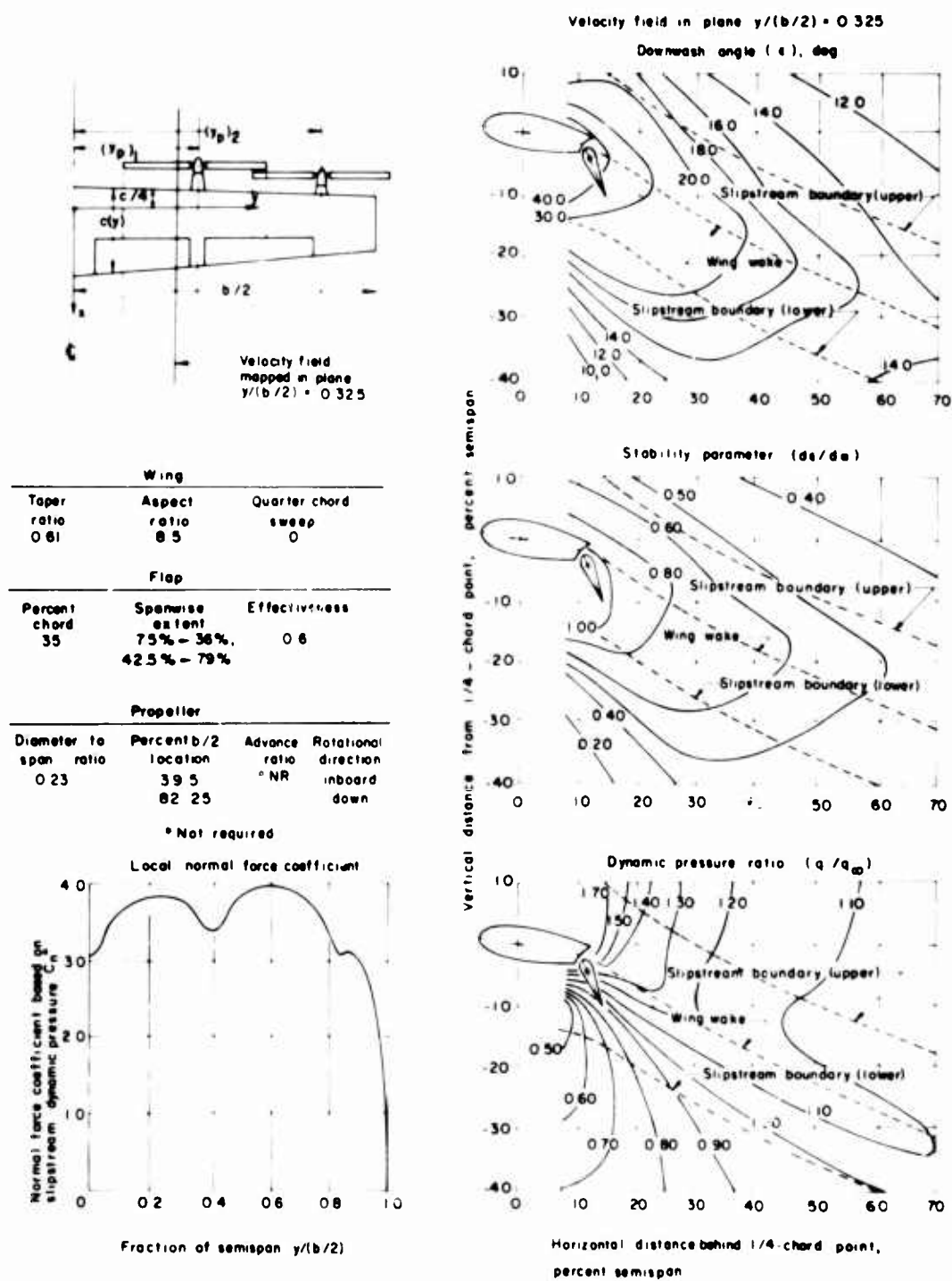


Figure 42. Four-Slipstream Configuration Design Charts:
 $T'_c = 0$, $\alpha = 10^\circ$, $\delta_f = 55^\circ$.

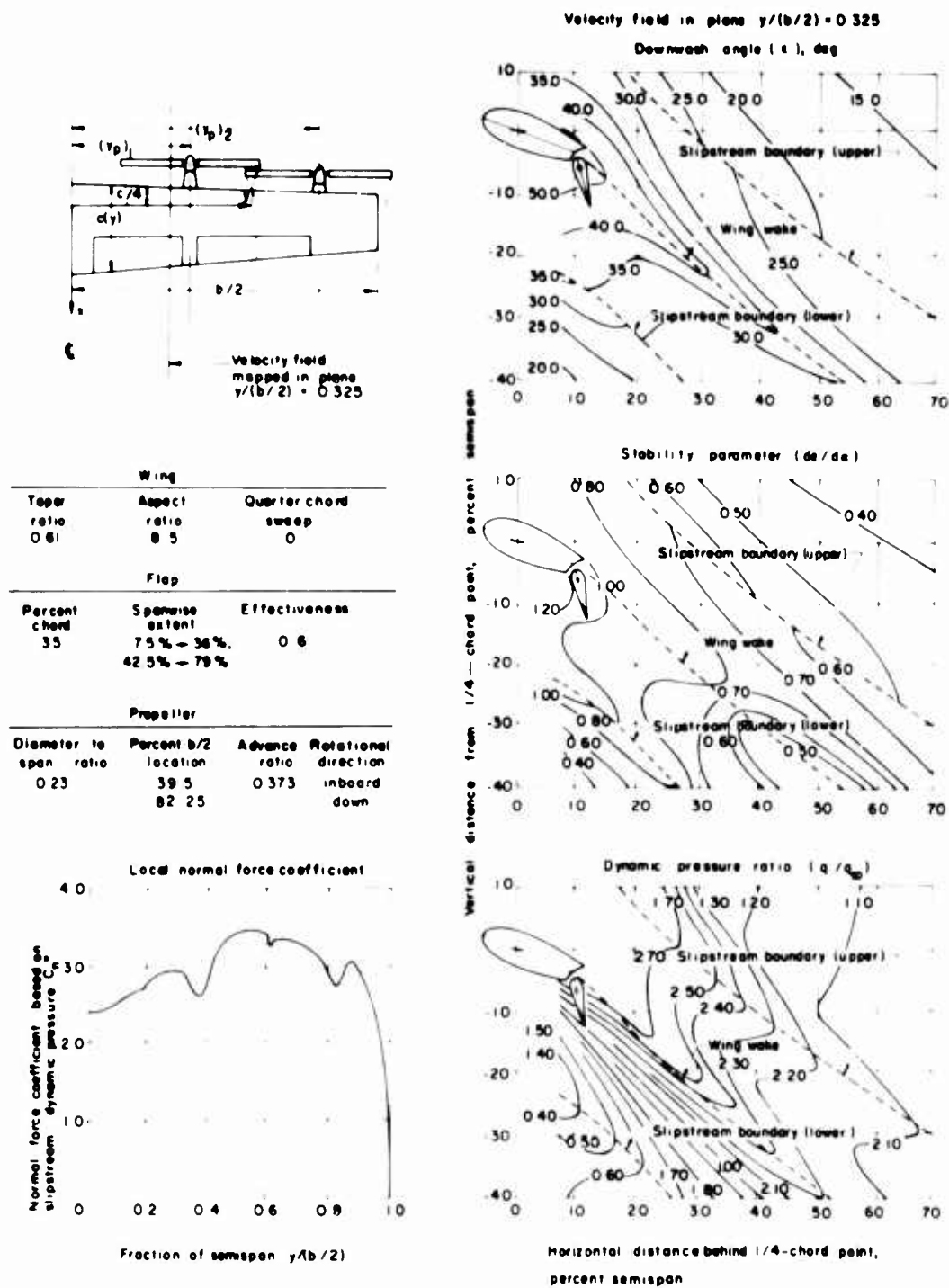


Figure 43. Four-Slipstream Configuration Design Charts:
 $T_c'' = 0.5$, $\alpha = 20^\circ$, $\alpha_p = 20^\circ$, $\delta_f = 55^\circ$, $J = 0.37$.

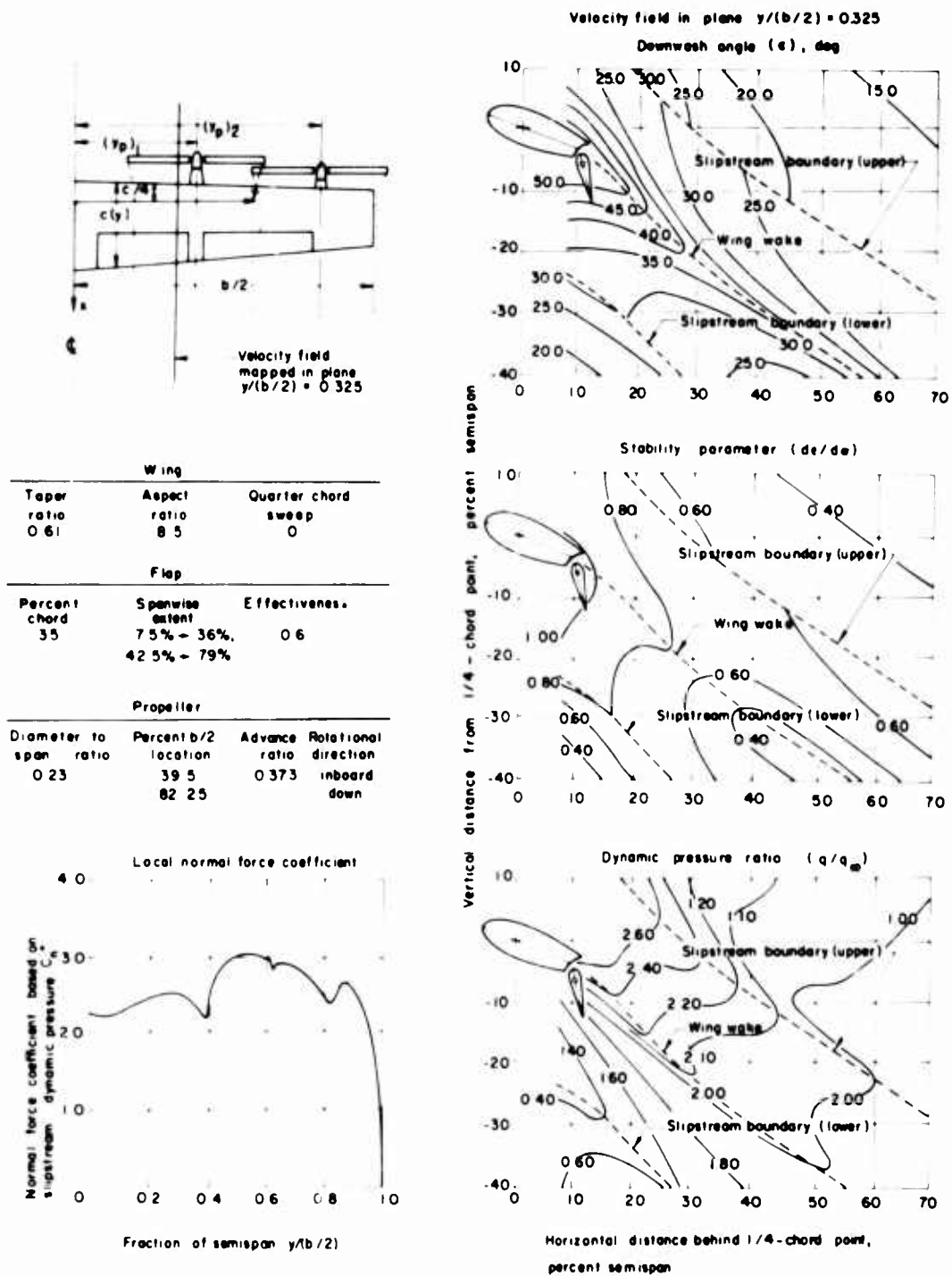


Figure 44. Four-Slipstream Configuration Design Charts:
 $T_c'' = 0.5$, $\alpha = 20^\circ$, $\alpha_p = 30^\circ$, $\delta_f = 55^\circ$, $J = 0.37$.

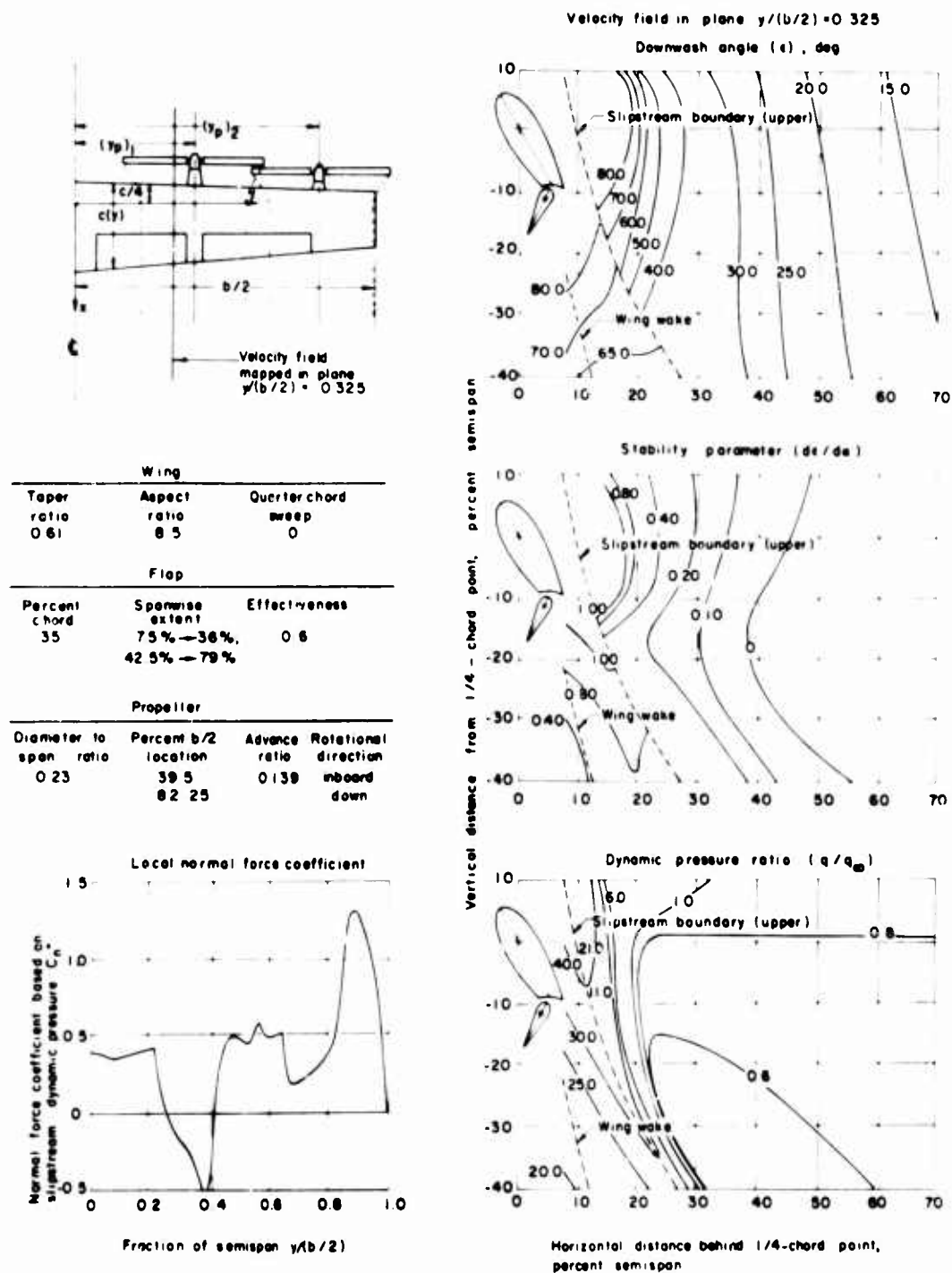


Figure 45. Four-Slipstream Configuration Design Charts:
 $T_c'' = 0.95$, $\alpha = 60^\circ$, $\alpha_p = 60^\circ$, $\delta_f = 55^\circ$, $J = 0.14$.

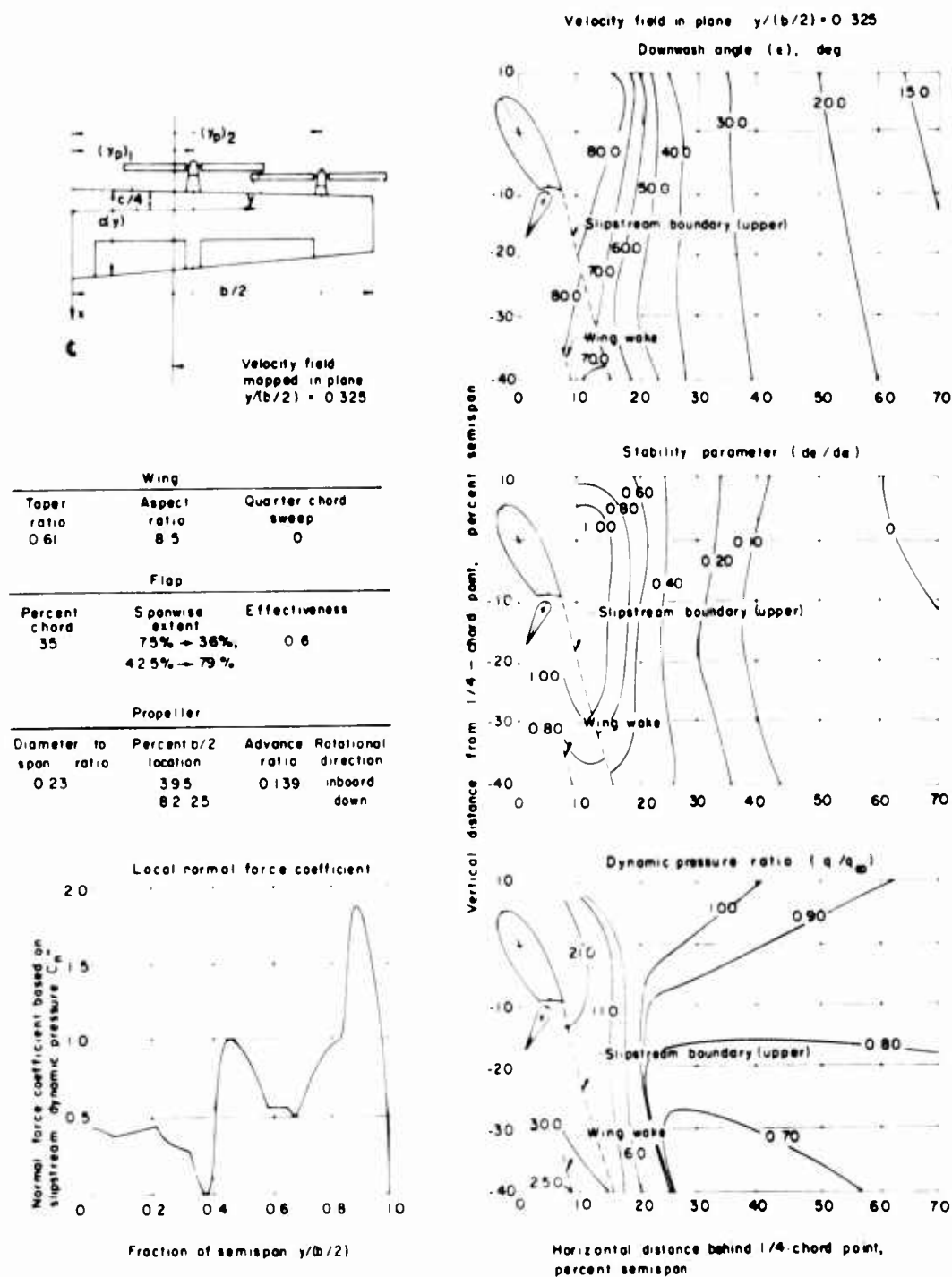


Figure 46. Four-Slipstream Configuration Design Charts:
 $T'_c = 0.95$, $\alpha = 60^\circ$, $\alpha_p = 50^\circ$, $\delta_f = 55^\circ$, $J = 0.14$.

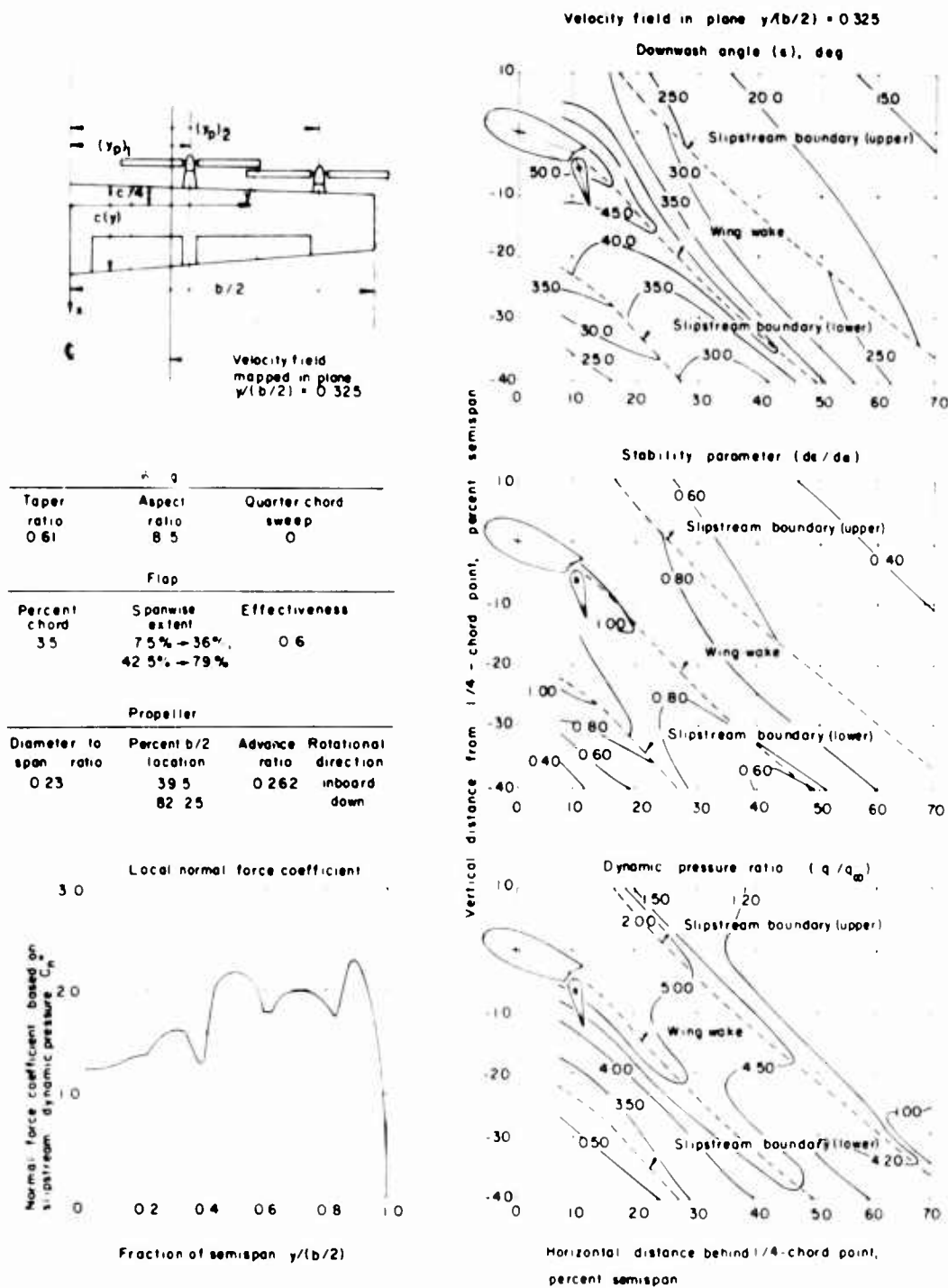


Figure 47. Four-Slipstream Configuration Design Charts:
 $T_c'' = 0.75$, $\alpha = 20^\circ$, $\alpha_p = 20^\circ$, $\delta_f = 55^\circ$, $J = 0.26$.

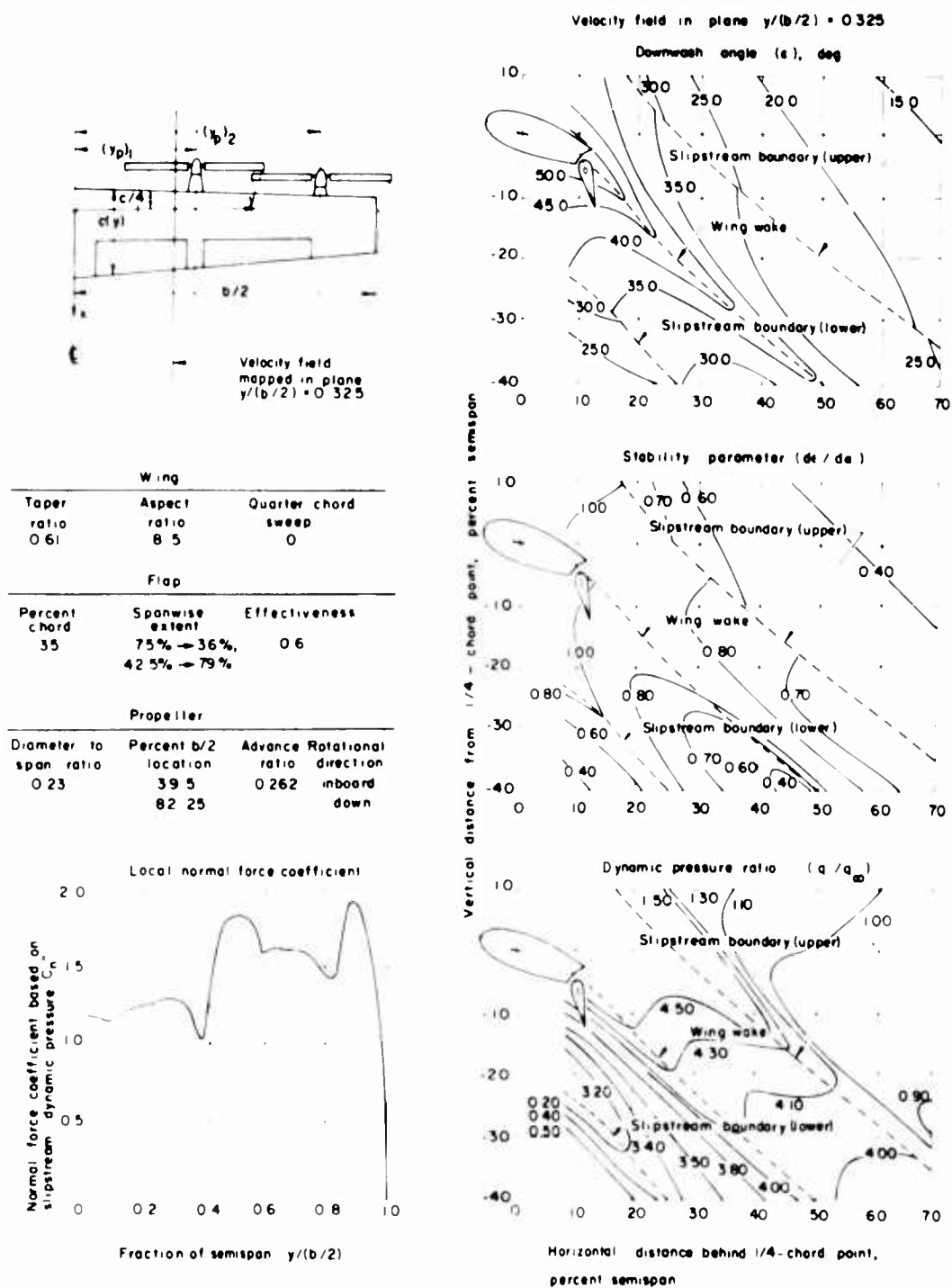


Figure 48. Four-Slipstream Configuration Design Charts:
 $T_c'' = 0.75$, $\alpha = 20^\circ$, $\alpha_p = 30^\circ$, $\delta_f = 55^\circ$, $J = 0.26$.

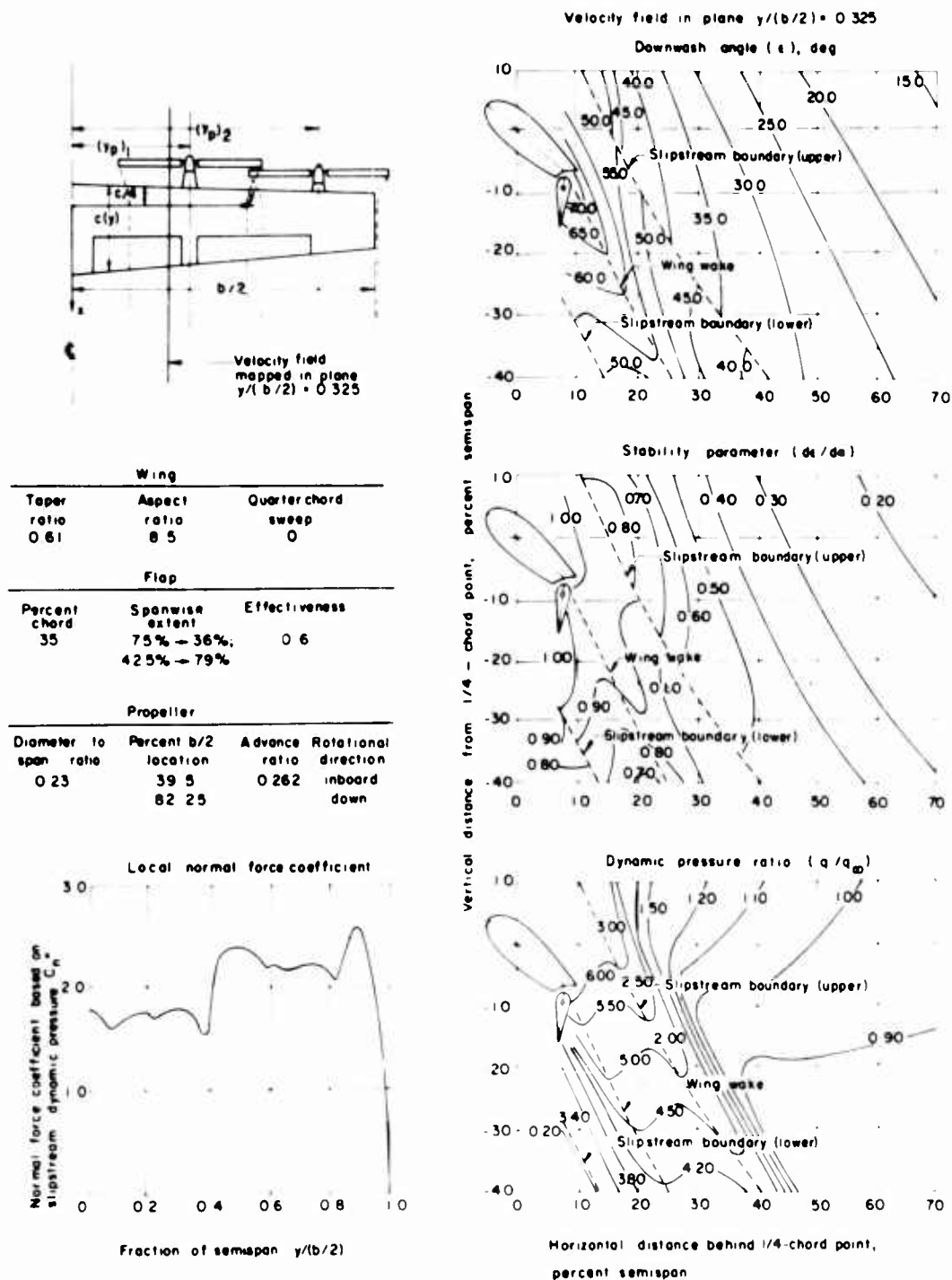


Figure 49. Four-Slipstream Configuration Design Charts:
 $T_c'' = 0.75$, $\alpha = 40^\circ$, $\alpha_p = 40^\circ$, $\delta_f = 55^\circ$, $J = 0.26$.

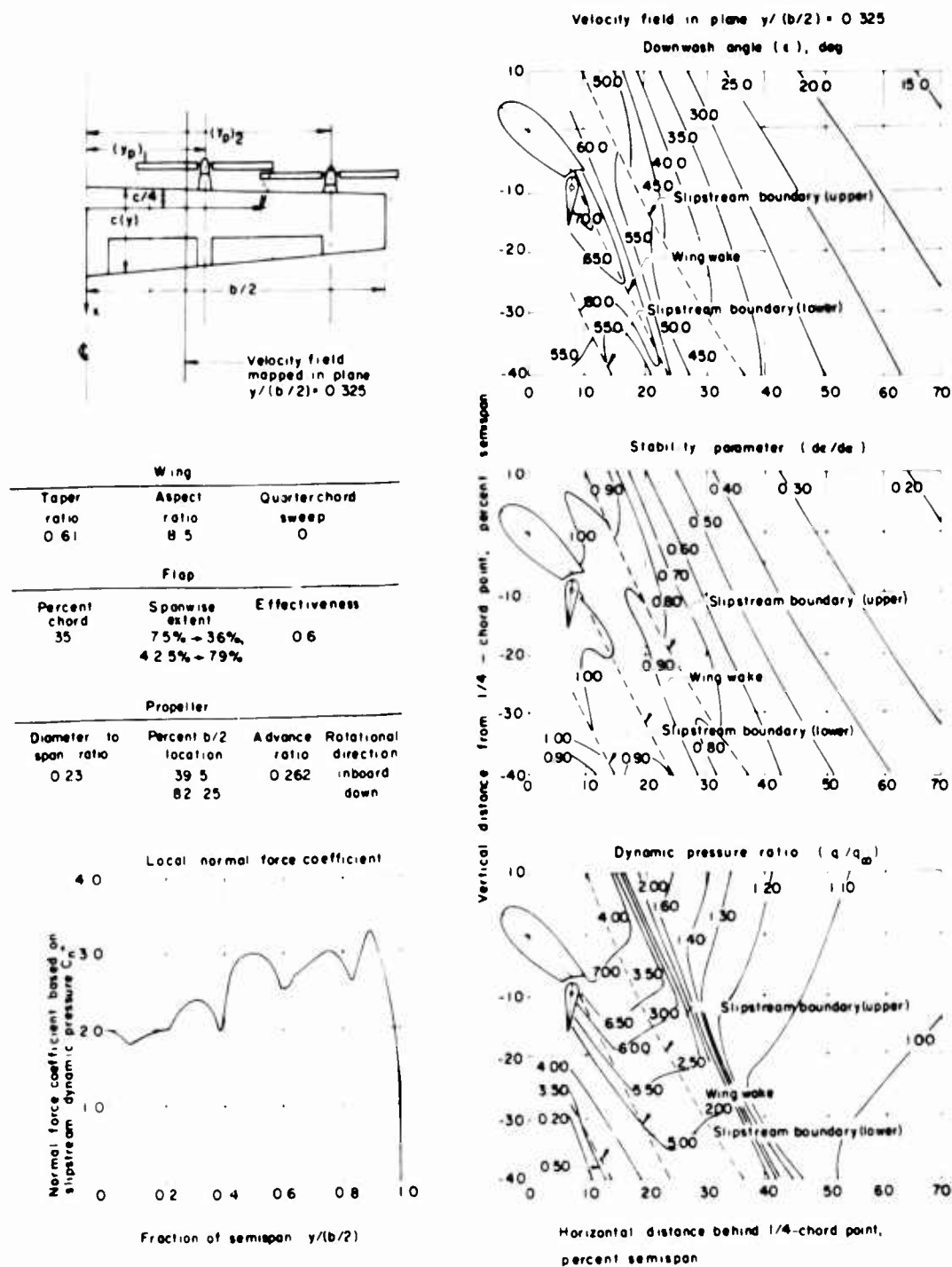


Figure 50. Four-Slipstream Configuration Design Charts:
 $T_c'' = 0.75$, $\alpha = 40^\circ$, $\alpha_p = 30^\circ$, $\delta_f = 55^\circ$, $J = 0.26$.

REFERENCES

1. Koning, C.: "Influence of the Propeller on Other Parts of the Aircraft Structure," Aerodynamic Theory, Vol. IV, Division M, edited by W. F. Durand, Dover Publications, New York, New York, 1935, pp. 361-431.
2. Glauert, H.: "The Lift and Drag of a Wing Spanning a Free Jet," British ARC R and M 1603, 1934.
3. Franke, A., and Weinig, F.: "The Effect of the Slipstream on an Airplane Wing," NACA TM 920, 1939.
4. Stüper, J.: "The Effect of Propeller Slipstream on Wing and Tail," NACA TM 874, 1938.
5. Graham, E. W., Lagerstrom, P. A., Licher, R. M., and Beane, B. J.: "A Preliminary Theoretical Investigation of the Effects of Propeller Slipstream on Wing Lift," Douglas Aircraft Co. Report SM-14991, 1953.
6. Ribner, H. S.: "Theory of Wings in Slipstream," University of Toronto, Institute of Aerophysics, Report No. 60, 1959.
7. Ellis, N. D.: "A Computer Study of a Wing in a Slipstream," University of Toronto, Institute for Aerospace Studies, Technical Note No. 101, 1967.
8. Ribner, H. S., and Ellis, N. D.: "Theory and Computer Study of a Wing in a Slipstream," American Institute of Aeronautics and Astronautics Paper No. 66-466, 1966.
9. Brenckmann, M.: "Experimental Investigation of the Aerodynamics of a Wing in a Slipstream," Journal of Aeronautical Sciences, Vol. 25, No. 5, May 1958, pp. 324-328.
10. Kuhn, R. E., and Draper, J. W.: "Investigation of the Aerodynamic Characteristics of a Model Wing-Propeller Combination and of the Wing and Propeller Separately at Angles of Attack up to 90° ," NACA TR 1263, 1956.
11. Simmons, L. F. G., and Ower, E.: "Investigation of Downwash in the Slipstream," British ARC R and M 882, 1923.
12. Lamb, H.: Hydrodynamics, Cambridge University Press, 1932.

13. Hall, M. G.: "The Structure of Concentrated Vortex Cores," Progress in Aeronautical Sciences, Vol. 7, edited by D. Kuchemann, Pergamon Press, London, 1966.
14. George, M., and Kisielowski, E.: "Investigation of Propeller Slipstream Effects on Wing Performance," USAAVLABS Technical Report 67-67, 1967.
15. Gray, W. L., and Schenk, K. M.: "A Method for Calculating the Subsonic Steady-State Loading on an Airplane with a Wing of Arbitrary Planform and Stiffness," NACA TN 3030, 1953.
16. Abbott, I. A., and von Doenhoff, A. E.: Theory of Wing Sections, Dover Publications, New York, New York, 1959.
17. Glauert, H.: The Elements of Aerofoil and Airscrew Theory, Cambridge University Press, 1947, pp. 157-160.
18. Goodson, K. W.: "Longitudinal Aerodynamic Characteristics of a Flapped Tilt-Wing Four-Propeller V/STOL Transport Model," NASA TN D-3217, 1966.
19. Helmbold, H. B.: "Limitations of Circulation Lift," *Journal of the Aero. Sciences*, Vol. 24, No. 3, pp. 237-238, March 1957.
20. Heyson, H. H., and Katzoff, S.: "Induced Velocities Near a Lifting Rotor with Nonuniform Disk Loading," NASA TR 1319, 1957.
21. Silverstein, A., and Katzoff, S.: "Design Charts for Predicting Downwash Angles and Wake Characteristics Behind Plain and Flapped Wings," NACA TR 648, 1938.
22. Grobner, W., and Hofreiter, N.: Integral Tafel, Zweiter Teil, Bestimmte Integrale, Springer-Verlag, Vienna, Austria, 1961.

APPENDIX I

EVALUATION OF INTEGRALS ARISING IN INCLINED ACTUATOR DISC THEORY

From Eq. (24) we have defined

$$I_o = \frac{1}{\pi R^2} \int_{S_{2o}} (\partial \bar{\varphi}_o / \partial z) dy dz$$

Integrating first with respect to z , and recognizing that $\lim_{z \rightarrow \pm\infty} \bar{\varphi}_o = 0$, we obtain

$$I_o = - \frac{4}{\pi R^2} \int_0^R \bar{\varphi}_o(z_u) dy$$

where z_u is the value of z along the upper boundary of the slipstream. Making use of Eq. (18) with $y^2 + z^2 = R^2$, we obtain

$$I_o = \frac{1-\mu}{\pi \mu^{1/2}} \int_0^1 \left\{ \ln \left[\frac{1-az}{1+az} \right] \right\} (1-z^2)^{-1/2} z dz$$

where $a = 2\mu^{1/2}/(1+\mu)$. The integration may be evaluated (e.g., p. 86, No. 22a of reference 22), and we obtain

$$I_o = -(1-\mu)$$

Similarly, the integral I_s as defined in Eq. (24) may be written

$$\begin{aligned} I_s &= \frac{1}{\pi R^2} \int_{S_{2s}} (\partial \bar{\varphi}_s / \partial z) dy dz = \frac{4}{\pi R^2} \int_0^R \bar{\varphi}_s(z_u) dy \\ &= - \frac{4}{\pi R^2} \int_0^R \bar{\varphi}_o(z_u) dy \\ &= I_o \end{aligned}$$

where we recall $\partial \varphi_s / \partial z = (\mu/w_\infty) (\partial \varphi_s / \partial z) - (1 - \mu)$, and we have made use of Eq. (17) evaluated on the boundary.

The expression for G_o may be defined as

$$G_o = \frac{1}{\pi R^2} \iint_{S_{2o}} (\nabla \bar{\varphi}_o)^2 r dr d\theta$$

The gradient term may be evaluated from Eq. (18). However, it is more convenient to evaluate $\nabla \bar{\varphi}_o^2$ directly from the complex potential F_o .

Thus, in polar coordinates we obtain

$$\begin{aligned} \nabla \bar{\varphi}_o^2 &= (dF_o/dZ) (dF_o^*/dZ^*)/w_\infty^2 \\ &= \frac{(1-\mu)^2}{r^4 + R^2 \mu^2 + 2r^2 R^2 \mu \cos 2\theta} \end{aligned}$$

Substituting into the expression for G_o , we obtain

$$G_o = \frac{(1-\mu)^2}{\pi} \int_1^\infty r dr \int_0^{2\pi} \frac{d\theta}{r^4 + \mu^2 + 2r^2 \mu \cos 2\theta}$$

The integral with respect to θ is $2\pi/(r^4 - \mu^2)$ (reference 22). Thus, G_o becomes

$$G_o = 2(1-\mu)^2 \int_1^\infty \frac{r dr}{r^4 - \mu^2} = \frac{(1-\mu)^2}{2\mu} \ln \frac{1+\mu}{1-\mu}$$

Evaluation of G_s may be accomplished in a similar fashion through use of the complex potential for F_s [Equation (15)] and through use of the definitions for $\partial \bar{\varphi}_s / \partial z$ and $\partial \bar{\varphi}_s / \partial y$. This gives

$$G_s = G_o$$

APPENDIX II

SLIPSTREAM SWIRL VELOCITY

An idealized vortex model of the propeller slipstream (e.g., reference 3) is that of a bound vortex of constant strength Γ rotating with the blade. The vortex is shed from the blade tip and moves rearward, because of the action of the free stream and because of self-induction effects, and forms a spiral-like trailing vortex system. A semi-infinite vortex of equal strength and lying along the slipstream axis must be inserted into the model to provide continuity with the bound vortex. The axial vortex induces swirl velocities inside the slipstream. The trailing vortices may be shown to have no effect on swirl inside the slipstream, but shield the axial vortex outside the slipstream, thereby reducing the resultant swirl velocities to zero as discussed in reference 3.

Far enough behind the propeller, the trailing vortex spiral may be assumed infinite in extent. The axial velocity increment induced inside the tube [see also Eq. (3)] is then

$$u_s - u_o = \gamma = 2N\Gamma / (u_o + u_s)$$

where the vortex strength per unit length γ is obtained by dividing Γ by the number of spiral loops per unit length. Here N is the number of blade revolutions per unit time and $(u_o + u_s)/2$ is the average axial velocity of the trailing spiral. Since $\Delta H/\rho = (1/2)(u_s^2 - u_o^2)$, we obtain

$$\Gamma = J V_\infty R_p \Delta H / q_\infty \quad (57)$$

where J is the advance ratio.

Due to the axial vortex, the inviscid swirl velocity v_θ will be taken as

$$v_\theta / V_\infty = (\Gamma / 2\pi r V_\infty) = (J / 2\pi) (R_p / r) (\Delta H / q_\infty)$$

which is the first factor in Eq. (34). The second factor accounts for viscous core effects (reference 12), and gives a zero swirl velocity at the center.

APPENDIX III

FORTRAN COMPUTER PROGRAM

GENERAL DESCRIPTION

An extensive, fairly general FORTRAN computer program has been developed to implement the methods and calculations presented in the body of this report. While written for and run only on the CDC 3600 computer (32K core), adaptation to IBM series 7040 and 7090 machines has been anticipated and should require no extensive modifications outside of plotting. (Plotting could not easily be transformed.)

The general organization of the program is as follows: the controlling program calls the input section which reads and stores data specifying the problem until a control word is read that directs a specific operation. Control then reverts to the driving program which supervises the desired calculation. Most numerical results are output as they are derived; however, with the plotting option active, certain results are retained for further processing. If the plotting option is on, it directs the smoothing, contouring, and plotting of these retained data. The main program then interrogates the input routine which reads and stores new data (if any) until another control word is encountered. This processing continues until a control word directs the program to stop.

The program has been written to handle any wing-centered configuration of one, two, or four propellers, provided there is no overlap of the fully contracted slipstreams, and provided the span loading is symmetrical about the airplane centerline. The two- and four-propeller cases allow for slipstream rotation as in Eq. (34). The wing has of necessity a straight quarter-chord line. However, the chord length, twist, flap-deflection angle, flap-effectiveness, ideal angle of attack, etc., may vary in an arbitrary manner along the span. These spanwise variables are input in a flexible tabular form (to be described in detail), and linear interpolation is used throughout. The plotting option, mentioned earlier, can be used to graphically produce wing loading curves and contour plots of constant downwash angle, constant dynamic pressure, and constant derivative of downwash angle with respect to angle of attack. Considerable hand smoothing of the contour plots is usually required, especially near slipstream and wake boundaries.

To complete the description of the program, the input format and options will be detailed. A sample run with the printed input and output has been included.

INPUT DESCRIPTION

Input to the digital computer program is read first as an alpha-numeric

card and checked for specific control words in columns 1 through 8. If there is a data control word indicating the presence of a data list, the card is re-read using the format-free NAMELIST feature of FORTRAN IV version 13. (For details on the many forms data values can take, the user is referred to the IBM FORTRAN IV Reference Manual.) If the card has a control word directing a specific operation, the appropriate action is taken. If there is no dollar sign in column 2, the card image (columns 3-80) is taken as 78 characters of BCD title information to serve as a heading for all output until another title is encountered.

The program is organized so that only data which differ from case to case have to be given. Certain default values are provided in case no values are given explicitly. For example, if no wing twist is specified, it will be taken as zero degrees. The default values for the various parameters are given in the table of recognized symbols, normal equivalents, and meanings (Tables I - III).

The problem of input can be broken into three parts:

1. Specification of the wing lifting surface and propeller configuration
2. Specification of the remaining quantities (environment, angle schedule, and numerical control)
3. Direction of the program to do one of several operations

These will be covered in the following sections.

SPECIFICATION OF THE AIRCRAFT CONFIGURATION

The aircraft is treated as a wing with a straight quarter-chord line and with one, two, or four propellers whose fully contracted slipstreams are centered on the $c/4$ line. Input to specify this lifting surface is under control of a data control word $\wedge \$WING \wedge \wedge$ (\wedge means a blank character).

The span of the wing (B), as an example, could be given as

$\wedge \$WING \wedge \wedge B=100 \END

In addition to the span (B), certain spanwise functions are used to describe the wing geometrically and aerodynamically. The chord (CHORD), the twist (TWIST), etc., are all considered functions of y (since the root chord of the wing is in the xz plane, and the wing extends in the $+y$ and $-y$ directions). The spanwise functions are stored in tabular form, and linear interpolation is used in extracting the variation from these tables. Different sets and numbers of y (Y) values may be associated with different tables. A single entry in a table gives a constant value over the whole span. The maximum number of entries in any one table is 40, and as mentioned earlier, no entry will result in a default value in some cases (see Table I). It is seen that the input form is arranged to conform to the usual "section" description of a wing, but this is not required.

The values of y need not be specified with each table, as they are carried along until replaced. Consequently, the entry of y values must precede the first multiple entry spanwise tabular function. The y values given on a $\wedge\$WING\wedge\wedge$ control card apply to the following $\wedge\$WING\wedge\wedge$ data cards until a new set of Y 's is read. As a simple example, a wing with a 60-foot span, a 5° linear washout, a 10-foot root chord, an 8-foot tip chord, and a constant ideal angle of attack of 6.67° could be specified as follows:

1. $\wedge\$WING\wedge\wedge$ B=60, ANGIDL(1)=6.67 \$END
2. $\wedge\$WING\wedge\wedge$ Y(1)=0, 30, TWIST(1)=0, -5 \$END
3. $\wedge\$WING\wedge\wedge$ CHORD(1)=10, 8 \$END

Several points are illustrated here. All numbers and symbols in the data list must be separated by either "=" or "," and all cards are terminated by \$END (the IBM FORTRAN IV manual describes the use of NAMELIST in detail). No y values need precede the spanwise functions with only a single entry but must be given before the double entry into the TWIST table. A table may be continued on more than one card (columns 2-80) until a \$END is read. Since the y value table is destroyed during calculation of a case, a y table must be given before wing data for any case changing these values (TWIST, CHORD, etc.). It is seen that specification of wings with flaps, taper, etc., is relatively straightforward. The reader is referred to Table I for a complete list of wing description options.

SPECIFICATION OF THE REMAINING PARAMETERS AND DATA

A schedule of α and β values must be furnished for most calculations. (The program uses $\beta = \alpha_p - \alpha$ to specify the propeller inclination.) This is accomplished using the $\wedge\$SCHED\wedge\wedge$ control card. The method is to give the starting value, the final value, and the step size of the angle in degrees. For example, the data to schedule α from -5° to $+10^\circ$ in steps of 5° and β from -10° to $+10^\circ$ in steps of 2° would read:

$\wedge\$SCHED\wedge\wedge$ AZ=-5, AMAX=10, DA=5, BZ=-10, BMAX=10, DB=2 \$END

The symbols recognized following a $\wedge\$SCHED\wedge\wedge$ control card are listed in Table III.

All remaining data are input under the direction of the $\wedge\$DATA\wedge\wedge$ control word, or the $\wedge\$PLOT\wedge\wedge$ word used to control the plotted output options. All the symbols recognized following a $\wedge\$DATA\wedge\wedge$ word are listed in Table II, and all those recognized following a $\wedge\$PLOT\wedge\wedge$ control word are listed in Table III.

PROGRAM CONTROL CARDS

There are several control cards that instruct the program to perform certain operations. For example, $\Delta\$STOP\Delta\Delta$ will terminate the program. The input section of the program reads and stores data until a control card is encountered directing some operation or calculation. When that action has been taken, control reverts to the input routine which continues reading cards until another direction is indicated.

The $\Delta\$RESET\Delta$ command clears all of the data from the storage areas. It is useful when different aircraft are to be processed in the same run. (The results of $\Delta\$RESET\Delta$ are the same as initial startup of the program with exception of titles and case number.)

$\Delta\$LOAD\Delta\Delta$ instructs the program to calculate the wing loadings only for the current α and β schedule. Loadings may be plotted if the MPLOT flag is on.

$\Delta\$WAKE\Delta\Delta$ instructs the program to calculate loadings and to calculate downwash fields and their derivatives at the points $[XMAP(i), ZMAP(i)]$ for each $YMAP(i)$. A whole set is calculated for each pair (α, β) in the current schedule. Plotting of the results occurs after each case if selected.

$\Delta\$STOP\Delta\Delta$ terminates the run.

SAMPLE COMPUTER INPUT AND OUTPUT

Input and output are shown on pages 94-96 for the four-slipstream configuration with flaps plotted in Figure 43.

TABLE I. RECOGNIZED SYMBOLS FOLLOWING A ^\$WING^^ CONTROL WORD			
Program Symbol	Normal Designation	Default Value	Meaning
<u>Single value symbols</u>			
B	b	**	wing span in feet
<u>Independent variable for spanwise tabular functions</u>			
*Y(1)	y	b/4	the current values of y will be linked to any table read in
<u>Spanwise tabular functions</u>			
*CMZERO(1)	C_{m_0}	0.0	wing zero-lift moment co- efficient
*CHORD(1)	c	**	chord length in feet
*TWIST(1)	α_t	0.0	twist angle in degrees
*CLIDL(1)	C_{l_a}	0.0	ideal lift coefficient
*FLPEFF(1)	$\partial \alpha / \partial \delta_f$	1.0	slope of the curve of sec- tion angle of attack versus flap-deflection angle for zero lift (flap effective- ness)
*FLPDEF(1)	δ_f	0.0	flap-deflection angle in degrees
*ANGIDL(1)	α_a	0.0	ideal angle of attack
<u>Station interface specifications</u>			
*STATNS(1)	y/(b/2)	0, .05, .1, ... 1.0	ratio of how far out to place horseshoe interfaces relative to half span
* These variables must be a consecutive list of from 1 to 40 values. ** Must be given.			

TABLE I - Continued			
Program Symbol	Normal Designation	Default Value	Meaning
*ARCS(1)	θ_i	0, 30... 180 0, 15... 90	2 ... props 1 prop angles in degrees at which to set up horseshoe inter- faces around slipstream

TABLE II. RECOGNIZED SYMBOLS FOLLOWING A
^\$DATA^^ CONTROL WORD

Program Symbol	Normal Designation	Default Value	Meaning
VV or VELCTY	V_{∞}	must be given free stream	velocity in feet per second
RHO	ρ	1.0	air density relative to a standard day
TCPP	T_c''	0.000001	thrust coefficient
RADIUS	R	**	radius of propeller in feet
PROP	y_p	0.0	spanwise propeller loca- tion in feet. [0.0 means one centrally mounted pro- peller, nonzero means at least two propellers]
PROP2	$(y_p)_2$	0.0	0.0 for 1- and 2-propeller cases, nonzero gives loca- tion of 3rd and 4th propel- lers
RPS	N	0.0	no. of revolutions per sec- ond of propeller for includ- ing rotation effects. (Posi- tive number means down- ward rotation inboard.)
EFFVIS	ν_t	0.1	effective viscosity (ft ² /sec)
DPROP	Ω	100.0	effective distance ahead of c/4 line in feet to locate propeller for purpose of slipstream rotation effects
STEP	-	b/10	step size to integrating trajectory wake
** Must be given.			

TABLE II - Continued			
Program Symbol	Normal Designation	Default Value	Meaning
*XMAP(1)	x'		downwash fields are calculated at each lattice point given by these coordinates. Only as many as are given will be calculated.
*YMAP(1)	y'		
*ZMAP(1)	z'		
PRINT	-	0	<p>a packed integer whose various digits control certain options as follows:</p> <p>unit digits: 0, 1 track mapping y stations only</p> <p>2 track all wing and ring stations</p> <p>3 track all wing, but no ring stations</p> <p>1-3 print wake profile</p> <p>tens digit: print W Y D(W Y)</p> <p>hundreds digit: value of MPLOT kept here internally</p>
* These variables may be given in a list of up to 10 variables.			

TABLE III. RECOGNIZED SYMBOLS FOLLOWING ^\$SCHEDA
AND ^\$PLOT^^ CONTROL WORDS

Program Symbol	Normal Designation	Meaning
<u>^\$SCHEDA recognized symbols:</u>		
AZ	α_{\min}	{ control scheduling of α (wing angle of attack) from α_{\min} to α_{\max} in steps of $d\alpha$ (degrees)
AMAX	α_{\max}	
DA	$d\alpha$	
BZ	β_{\min}	{ control scheduling of propeller angle with respect to wing from β_{\min} to β_{\max} in steps of $d\beta$ (degrees)
BMAX	β_{\max}	
DB	$d\beta$	
<u>DEFAULT</u>		
SIZE	must be given for plotting	total height of contour plot
*WZC(1)	no downwash plot	list of downwash angles to contour
*DWZC(1)	no $d\epsilon/d\alpha$ plot	list of downwash derivative levels to contour
*PC(1)	no pressure plot	list of pressure levels to contour
MPLOT	no plot	mode of plotting 0 no plotting 1-4 contours, no cross plots 5-8 both contours and cross plots 9 cross plots only in ranges 1-4 and 5-8 there is 1-4 point interpolation used in producing contours
* These variables may be given in a list of up to 20 variables.		

```

XC-142A PRODUCTION RUNS -- GENERAL DATA
$DATA PROP=13.4, PROP2=27.8, RADIUS=7.75, VV=113, RPS=20, FFFVIS=.1 $END
$WING R=67.5, Y=0.33.75, CHORD=9.85,5.96 $END
$DATA YMAP=10.969 $END
$DATA XMAP=2.5,5.0,7.5,10.0,12.5,15.0,17.5,20.0,22.5,25.0 $END
$DATA ZMAP=5.0, 2.5, 0, -2.5, -5.0, -7.5, -10.0, -12.5, -15.0 $END
$SCHED AMAX=-100, BMAX=-100 $END
$DATA DPPROP=400 $END

PLOT STANDARDS
$PLOT MPLOT=8 $END
$PLOT SIZE=4.73 $END
$PLOT DWZC=2.0,1.8,1.6,1.4,1.2,1.0,.8,.6,.4,.2,0,-.2,-.4,-.6,
      -.8,-1.0,-1.2 $END
$PLOT PC=.4,.5,.6,.7,.8,.9,1.0,1.1,1.2,1.3,1.4,1.5,1.6,1.7 $END
XC-142A FLAP DATA
$WING Y=0, FLDPDEF=55 $END
$WING Y=0,2.5,2.5,3,12.15,12.16,14.34,14.35,26.65,26.66,28.64
      ,28.65,23.75 $END
$WING FLDPDEF=0,0,.6,.6,0,0,.6,.6,0,0,.6,.6 $END
XC-142A FIG 43 TCPD=.5 (FLAPS)
$DATA TCPD=.5 $END
$PLOT WZC=5.10,15.20,25.30,35.40,45.50,55 $END
$SCHED AZ=20, RZ=0 $END
$WAKE $END
$STOP

```

25 CARDS

*** WING IN A SLIPSTREAM STUDY *** 5/ 9/68 CASE 1 PAGE 2
 XC-142A FIG 43 ICPP=5.5 (FLAPS)

***** ANGLES - ALPHA= 20.00, BETA= 0 ***** PRODUCING DELTA= 13.49, R(CONT) 7.04, MU= .697

COEFFICIENTS IN REMOTE FREE STREAM COORDINATES

WING LIFT = 1.8709 WING DRAG = 2.0152 WING MOMENT = 0

PROP LIFT = .1710 PROP DRAG = .4698

HORZ FORCE = 2.3475 VERT FORCE = 1.9919

POWER/POWER-HOVER = 2.3044 LIFTABLE WEIGHT = 32273 LBS

WING LOADINGS

Y	LOAD	Y	LOAD	Y	LOAD	Y	LOAD
344	2.3792	2.531	2.4441	4.219	2.5687	5.709	2.6582
7.594	2.8429	9.281	2.9127	10.969	2.8857	12.656	2.6034
16.031	3.3415	17.719	3.4297	19.406	3.4121	20.347	3.3926
21.347	3.3259	22.781	3.3070	24.469	3.2417	26.156	3.0829
29.531	3.0410	31.219	2.7633	32.906	2.0375		

WING GAMMAS

2493.5024	2709.4356	2789.5191	2834.8381	1424.7857
1439.6278	1439.5674	1388.0711	1211.1536	1366.7637
1510.1224	1512.3477	1467.0177	1437.7442	2814.7306
1387.1301	1346.4077	1279.1501	1171.4979	996.3063
1106.4445	971.5335	691.4731		

WING GAMMAS

709.2808	660.1096	620.1681	587.7698	562.6309
545.0424	535.6808	535.8270	547.7704	575.3292
624.0162	698.8630	694.5444	613.5321	548.1316
492.1427	441.6355	394.6493	350.0945	306.8547
263.4198	217.1963	162.1786	75.7638	

FIELD MAP AT Y = 10.97 (WZ,ZATAN(VZ,VX),D(WZ),D(ALPHA),PRESSURE)												
Z / X =	2.50	5.00	7.50	10.00	12.50	15.00	17.50	20.00	22.50	25.00	27.50	30.00
RING LIP	5.888	4.265	1.731	-.686	-2.887	-4.809	-6.391	-8.145	-9.850	-11.507	-13.189	-14.943
Z(MAKE) =	-.910	-2.533	-5.067	-7.484	-9.446	-11.407	-13.189	-14.943	-16.649	-18.305	-19.987	-21.741
RING LIP	-7.708	-6.331	-11.665	-14.282	-16.244	-18.205	-19.987	-21.741	-23.447	-25.103	-26.759	-28.415
5.00 WZ =	-36.704	-27.612	-21.223	-18.411	-16.272	-14.807	-13.708	-12.687	-11.833	-11.078	-10.323	-9.568
D(WZ) =	-1.863	-1.690	-1.515	-1.445	-1.395	-1.362	-1.334	-1.312	-1.293	-1.276	-1.259	-1.242
PRES. =	1.534	2.409	1.468	1.323	1.228	1.166	1.124	1.093	1.070	1.053	1.036	1.019
2.50 WZ =	-29.992	-31.218	-26.357	-21.034	-18.811	-16.811	-15.313	-14.093	-13.072	-12.163	-11.254	-10.345
D(WZ) =	-.840	-.734	-.709	-.518	-.457	-.413	-.376	-.349	-.326	-.306	-.286	-.266
PRES. =	2.686	2.231	1.950	1.303	1.216	1.158	1.117	1.087	1.065	1.048	1.031	1.014
0 WZ =	-50.913	-37.571	-29.216	-25.298	-22.841	-18.782	-17.015	-15.595	-14.398	-13.349	-12.300	-11.251
D(WZ) =	-.952	-.823	-.709	-.693	-.920	-.474	-.427	-.393	-.365	-.340	-.315	-.290
PRES. =	3.709	2.083	1.770	1.617	1.193	1.143	1.106	1.078	1.058	1.042	1.026	1.010
-2.50 WZ =	-59.730	-49.579	-33.177	-26.908	-23.838	-20.120	-18.881	-17.182	-15.802	-14.822	-13.842	-12.862
D(WZ) =	-1.286	-.980	-.790	-.683	-.636	-.508	-.483	-.445	-.410	-.380	-.355	-.330
PRES. =	1.156	1.991	1.579	1.469	1.386	1.119	1.090	1.067	1.048	1.034	1.018	1.002
-5.00 WZ =	-42.216	-40.790	-43.786	-29.735	-25.389	-22.771	-19.364	-18.543	-17.241	-15.988	-14.735	-13.482
D(WZ) =	-1.145	-.992	-.908	-.741	-.665	-.621	-.428	-.486	-.460	-.427	-.397	-.367
PRES. =	.457	.992	1.621	1.350	1.282	1.240	1.067	1.053	1.038	1.026	1.010	0.994
-7.50 WZ =	-36.648	-35.711	-34.211	-40.321	-28.916	-24.273	-22.135	-21.804	-18.225	-17.298	-16.371	-15.444
D(WZ) =	-1.119	-.938	-.821	-.815	-.762	-.652	-.617	-.582	-.468	-.472	-.437	-.402
PRES. =	.239	.601	1.002	1.442	1.238	1.175	1.151	1.154	1.027	1.017	0.999	0.982
-10.00 WZ =	-27.030	-31.612	-30.583	-29.856	-35.461	-28.556	-23.644	-21.678	-20.441	-17.829	-16.802	-15.775
D(WZ) =	-.595	-.939	-.797	-.709	-.454	-.877	-.659	-.607	-.514	-.424	-.334	-.244
PRES. =	.526	.434	.732	.981	1.291	1.206	1.115	1.094	1.086	1.009	0.991	0.974
-12.50 WZ =	-20.386	-24.880	-28.060	-26.977	-26.964	-30.102	-31.492	-23.661	-21.379	-20.135	-18.891	-17.647
D(WZ) =	-2.76	-.562	-.847	-.701	-.625	-.333	-1.205	-.719	-.610	-.525	-.435	-.345
PRES. =	.541	.650	.607	.794	.947	1.16	1.240	1.092	1.060	1.050	0.971	0.954
-15.00 WZ =	-15.769	-20.740	-23.108	-25.987	-24.991	-28.299	-25.839	-34.478	-28.743	-21.423	-18.103	-14.783
D(WZ) =	-.120	-.365	-.539	-.747	-.627	-.577	-.392	-.603	-.922	-.649	-.376	-.103
PRES. =	.584	.648	.740	.720	.828	.933	1.052	1.232	1.107	1.044	0.981	0.918
BEGIN CONTOUR OF DOWNWASH ANGLE												
Y = 10.969												
BEGIN CONTOUR OF L(DOWNWASH)/D(ATTACK ANGLE)												
Y = 10.969												
BEGIN CONTOUR OF DYNAMIC PRESSURE												
Y = 10.969												

UNCLASSIFIED

Security Classification

DOCUMENT CONTROL DATA - R & D

(Security classification of title, body of abstract and indexing annotation must be entered when the overall report is classified)

1. ORIGINATING ACTIVITY (Corporate author) Air Vehicle Corporation San Diego, California		2a. REPORT SECURITY CLASSIFICATION Unclassified	
		2b. GROUP	
3. REPORT TITLE LIFTING SURFACE THEORY AND TAIL DOWNWASH CALCULATIONS FOR V/STOL AIRCRAFT IN TRANSITION AND CRUISE			
4. DESCRIPTIVE NOTES (Type of report and inclusive dates) Final Report			
5. AUTHOR(S) (First name, middle initial, last name) E. S. Levinsky, H. U. Thommen, P. M. Yager, and C. H. Holland			
6. REPORT DATE October 1968		7a. TOTAL NO OF PAGES 115	7b. NO OF REFS 22
8a. CONTRACT OR GRANT NO DAAJ02-67-C-0059		8b. ORIGINATOR'S REPORT NUMBER(S) USAAVLABS Report 68-67	
8c. PROJECT NO 1F125901A142		8d. OTHER REPORT NO(S) (Any other numbers that may be assigned this report) Report No. 356	
10. DISTRIBUTION STATEMENT This document has been approved for public release and sale; its distribution is unlimited.			
11. SUPPLEMENTARY NOTES		12. SPONSORING MILITARY ACTIVITY U. S. Army Aviation Materiel Laboratories Fort Eustis, Virginia	
13. ABSTRACT A large-tilt-angle lifting-surface theory is developed for tilt-wing and tilt-propeller/ rotor V/STOL aircraft. The method is based upon an inclined actuator disc analysis in which closed-form solutions are obtained for the velocity potential at large dis- tances behind the actuator surface. Both the normal velocity and the nonlinear pres- sure boundary conditions are satisfied exactly across the slipstream interface. The inclined actuator disc analysis is combined with a discrete-vortex Weissinger- type lifting surface theory. Wing-propeller combinations at arbitrary wing angle of attack, propeller tilt angle, and thrust coefficient are considered. Multiple slip- stream effects including slipstream rotation are introduced. Agreement between theory and experiment is shown to be satisfactory for small slip- stream inclination angles. However, at large angles the theory (with an undeformed, but displaced, slipstream and wake) predicts significantly lower downwash angle the tail region than shown by the test data, possibly due to slipstream deformation and wake roll-up. Use of only one-half the calculated wake displacement gave im- proved agreement at these conditions. However, insufficient data are available for making a general evaluation of the theory at large angles. Extensive digital computer results are given in chart form, showing span loading, downwash angle ϵ , stability parameter $d\epsilon/d\alpha$, and dynamic pressure at arbitrary points behind the wing for V/STOL configurations with two and four slipstreams.			

DD FORM 1473

REPLACES DD FORM 1473, 1 JAN 64, WHICH IS
OBSOLETE FOR ARMY USE.UNCLASSIFIED
Security Classification

UNCLASSIFIED
Security Classification

14	KEY WORDS		LINK A		LINK B		LINK C	
			ROLE	WT	ROLE	WT	ROLE	WT
	Propeller Slipstream-Wing Interaction Inclined Slipstream Analysis Span Load Distribution Inclined Actuator Disc Theory Wing Lifting Surface Theory Downwash Angle Longitudinal Stability Tail Effectiveness Tilt Wing Tilt Propeller/Rotor V/STOL							

UNCLASSIFIED
Security Classification

11045-008